Application de la chimiluminescence de flamme et du courant d'ionisation à la surveillance de l'état de combustion pour une chaudière à gaz domestique

Yi Ding

université PARIS-SACLAY

CentraleSupélec

NNT: 2018SACLC039

Use of flame chemiluminescence and ionization current for the combustion state monitoring of a domestic gas boiler

Thèse de doctorat de l'Université Paris-Saclay
préparée à CentraleSupélec

École doctorale n°579 : Sciences mécaniques et énergétiques, matériaux et géosciences (SMEMAG)
Spécialité de doctorat : Energétique

Thèse présentée et soutenue à Gif-sur-Yvette, le 19/06/2018, par

Yi DING

Composition du Jury :

Vincent Giovangigli Directeur de recherche au CNRS, CMAP, Ecole Polytechnique	Président, Examinateur
Fabien Halter Professeur, Université d'Orléans, ICARE/CNRS	Rapporteur
David Honoré Professeur, INSA de Rouen, CORIA/CNRS	Rapporteur
Alexandre Gay Ingénieur, Bosch Thermotechnologie	Invité
Thierry Schuller Professeur, Université Toulouse 3, IMFT/CNRS	Directeur de thèse
Nasser Darabiha Professeur, CentraleSupélec	Co-Directeur de thèse
Daniel Durox Ingénieur de recherche, CentraleSupélec	Co-Directeur de thèse

Thèse de doctorat

Remerciements

Je tiens tout d'abord à remercier les membres de jury, mes rapporteurs Fabien Halter et David Honoré, le président et examinateur Vincent Giovangigli, et mes encadrants chez Bosch et au laboratoire EM2C, pour le temps qu'ils ont consacré à la relecture de mon manuscrit et à l'évaluation de mon travail de 3 ans. Leurs remarques pertinentes et constructives ont permis d'améliorer le manuscrit.

Je tiens vivement à remercier mes encadrants de thèse, Daniel, Thierry, Nasser et Alexandre. J'ai pu connaître Daniel et avoir son aide même avant le début de la thèse. Son accompagnement pendant les 3 ans sur divers sujets a été indispensable à la réalisation de ce travail et son expertise a rendu mes expérience beaucoup plus fluides. Les suggestions de Thierry ont permis plusieurs fois de débloquer la recherche et j'apprécie aussi le soin qu'il a pris pour la correction de mes rédactions. Grâce à Nasser, j'ai pu compléter ma thèse avec une approche numérique qui s'avère très intéressante. J'ai aussi apprécié les échanges avec Alexandre tout au long de la thèse ainsi que la liberté qu'il m'a accordée. Le soutien de l'équipe de François Vuillaume de Bosch Thermotechnologie a également été important. J'apprécie surtout leur travail pour la construction de ce sujet de thèse et leur soutien malgré un premier refus de la part de l'ANRT.

Je souhaite également remercier l'ensemble des personnels administratifs, Nathalie, Noï, Brigitte, et des personnels techniques, Yannick, Jérôme et Dédit. Je suis impressionné par leur gentillesse, efficacité et fiabilité.

J'ai pu aussi bénéficier énormément des discussions avec les doctorants et permanents du laboratoire: Clément, David, Kévin, Erwan, Nicolas, $\cdots$. Aussi, l'ambiance amicale du laboratoire EM2C a fait de ce séjour la meilleure période depuis mon arrivée en France.

Abstract

Due to a more diverse set of supply sources and the integration of renewable resources as for examples biogas and hydrogen, the European natural gas network is expecting greater variations of gas composition in the future. These evolutions may lead to adverse impacts on the performances of combustion apparatus, including domestic gas boilers. The current control strategy of these boilers optimizes the heating efficiency and pollutant gas emissions assuming a fixed composition of the natural gas. A new control system capable of monitoring and regulating the flame state in real time is necessary to maintain optimized performances despite gas composition variations.

The present thesis addresses the use of two potential low-cost techniques, *i.e.*, flame chemiluminescence and ionization current, for the monitoring of flame equivalence ratio, a key parameter for the optimization of boiler performances. Experiments are performed on three burner configurations, including a cylindrical multi-perforated burner used in real domestic gas boilers, a conical flame burner and a porous plug burner. In addition, numerical calculations are carried out based on direct flow simulations of 1-D premixed laminar flames with detailed chemistry mechanisms including the chemiluminescent species. These simulations are used as a support for the experimental findings.

The first part of this work focuses on the use of flame chemiluminescence to the equivalence ratio sensing. Experiments are first carried out to understand the effects of secondary natural gas components, including N_2, CO_2, H_2, C_2H_6 and C_3H_8, on the chemiluminescence intensities of CH^*, OH^* and CO_2^*. Equivalence ratio indicators are inferred from the chemiluminescence signal. The investigation proceeds by examining effects of the flame-burner heat exchange on the chemiluminescence signal, an important feature of the multi-perforated industrial burner with a large turn-down ratio. The evolution of chemiluminescence intensities with the inlet gas velocity and gas temperature is investigated. The interference of several disturbing factors for the chemiluminescence signal characterization is also analyzed.

The second part is dedicated to the analysis of the flame ionization current.

Its application to the flame state monitoring is already emerging in domestic gas boilers. Experiments are carried out on the conical flame burner to understand the evolution of the ionization current intensity with various parameters including the probe position, flame power, fuel composition and equivalence ratio. Changes in the ionization current are attributed to modifications of the distance between the flame base and the burner rim. A new equivalence ratio sensing strategy coupling both flame chemiluminescence and ionization current is proposed.

In the third part, a control loop is developed with LabVIEW to demonstrate the feasibility of equivalence ratio self-regulation by real time analysis of the flame chemiluminescence signal when the fuel gas composition is varied. The equivalence ratio indicators identified in the first part are tested in order to determine the best choice for industrial application. The demonstrative control system is tested by changing the equivalence ratio set value and gas composition in order to assess the robustness of the technique.

Résumé

Le réseau de distribution européen verra dans le futur des variations plus importantes de la composition du gaz naturel, à cause d'une diversification des sources d'approvisionnement mais aussi de l'intégration des gaz produits par les énergies renouvelables tels que le biogaz et l'hydrogène. Ces modifications de combustible auront un impact sur les performances des appareils de combustion, y compris les chaudières à gaz domestiques. La stratégie de contrôle actuelle de ces chaudières optimise le rendement et la réduction des émissions de polluants avec l'hypothèse d'une composition fixe du gaz injecté. Pour continuer à assurer des performances optimisées malgré des variations de composition, il est nécessaire de concevoir un nouveau système de contrôle, capable de surveiller et de réguler automatiquement en temps réel l'état de la combustion.

Dans le travail proposé, une stratégie est développée qui repose sur deux techniques à coût réduit exploitant la chimiluminescence de flamme et le courant d'ionisation pour surveiller et contrôler la richesse du mélange, un paramètre important pour l'optimisation des performances des chaudières. Les expériences sont effectuées sur trois configurations, un brûleur cylindrique multi-perforé utilisé dans les chaudières domestiques, un brûleur à flamme conique et un brûleur poreux. En parallèle, des simulations de ces écoulements ont été réalisées avec des modèles de flamme 1-D incluant une description détaillée de la cinétique des réactions dont celles de chimiluminescence. Ces simulations sont utilisées comme support aux découvertes expérimentales.

La première partie du travail est consacrée à l'analyse du signal de chimiluminescence pour mesurer la richesse de flamme. Des expériences sont effectuées pour examiner les effets de composants secondaires, tels que N_2, CO_2, H_2, C_2H_6 et C_3H_8, sur les intensités de chimiluminescence des radicaux CH^*, OH^* et CO_2^*. Ces expériences permettent d'identifier plusieurs indicateurs de la richesse. L'impact de l'échange de chaleur entre la flamme et le brûleur sur ces signaux est ensuite étudié. Cet échange de chaleur conditionne l'intensité de la chimiluminescence dans le cas du brûleur industriel multi-perforé. On s'intéresse surtout à l'évolution des intensités de chimiluminescence avec la vitesse et la température des gaz frais. Une analyse est également faite des

principaux facteurs pouvant perturber la caractérisation du signal de chimiluminescence.

Le courant d'ionisation de flamme est étudié dans la deuxième partie. Utiliser ce courant pour surveiller l'état de la combustion dans les chaudières domestiques est déjà envisagé par certains constructeurs. Des expériences ont été réalisées pour comprendre l'évolution de l'intensité du courant d'ionisation avec des paramètres tels que la position de la sonde, la puissance de la flamme, la composition des gaz et la richesse du mélange combustible injecté. On montre que ces évolutions sont corrélées avec le changement de la distance entre le pied de flamme et le brûleur.

Dans la troisième partie, une boucle de contrôle est développée avec le logiciel LabVIEW pour démontrer la faisabilité du réglage automatique de la richesse à l'aide du signal de chimiluminescence lorsque la composition du mélange combustible varie. Les indicateurs de richesse proposés dans la première partie sont testés pour identifier le meilleur candidat pour une application industrielle. Cette démonstration de système de contrôle est validée en modifiant la consigne de richesse et la composition du gaz pour caractériser la robustesse de cette technique.

Contents

List of Tables

List of Figures

Nomenclature

Latin Characters :

A_{21}	rate of radiative decay
c	concentration
c_p	specific heat capacity
c_ν	Speed of light
E	electrical field strength
e	elementary charge
f_0	mass burning flux
I	chemiluminescence emission intensity
I_s	specific chemiluminescence emission intensity
j	current density
$\mathcal{K}$	reaction rate constant
k_B	Boltzmann constant
n	number concentration
m	mass
$\dot{m}$	mass flow rate
$\dot{V}$	volumetric flow rate
p	pressure
P	power
Q_{21}	global rate of quenching
R	ohmic resistance
S_L	laminar flame velocity under adiabatic conditions
T_b	burnt gas temperature
U	voltage
u_0	mean bulk velocity of reactant stream at burner outlet
V	diffusion velocity
W	species molar mass
X	volumetric fraction
X^{fuel}	volumetric fraction in the fuel blend
Y	mass fraction
y	fluorescence yield of excited species

Greek Characters :

δ	distance between conical flame base and burner rim	μ	mobility of charged particle
ϵ	permittivity	ρ	density
κ	stretch rate	ϕ	fuel-air equivalence ratio
λ	heat conductivity	ξ_{loss}	heat loss fraction
λ_ν	wavelength		

Abbreviations :

CF	Conversion Factor of gas flow meter
FWHM	Full Width Half Maximum
ERI	Equivalence Ratio Indicator
HHV	High Heating Value
LHV	Low Heating Value
PM	Photomultiplier tube
SD	Standard Deviation
WI	Wobbe Index

Introduction

Evolutions of European natural gas network

Household gas boilers for heating and hot water generation are generally fueled by natural gas, composed primarily of methane but the specific composition may vary. The European natural gas supply relies on a few major sources originating from Russia, the North Sea, the Netherlands and North Africa through pipelines and from other regions from the world through LNG* (Adelt et al. 2010). The gas composition varies according to the supply sources. As an example, a summary of the compositions in Germany from several sources is taken from Adelt et al. (2010) in Tab. 0.1.

In Europe, a more diverse set of supply sources is expected in the future. The decreasing indigenous natural gas supply is part of the reason. The Groningen field in the Netherlands, the largest in Europe, has been planned to stop the gas production by 2030 due to the danger of an earthquake. It is also driven by the geopolitical reason to enhance the security of gas supply. The diversification of supply sources may then lead to larger variations of the gas composition (Williams et al. 2012).

The gas composition may also be modified by the injection of gases obtained from renewable resources. One example is the biomethane produced by the anaerobic digestion process from organic wastes. The raw biogas is mainly composed of methane and CO_2. After a series of purification processes, removing especially the undesirable components of CO_2 and H_2S, the gas can be injected into the gas network†. It has also been proposed to use the so-called raw biogas, with no more than the basic purification procedures removing H_2S, to feed domestic gas boilers and meet local heating demands.

*Liquefied Natural Gas

†ADEME, Enea Consulting, APESA. 2017. Suivi technique, économique et environnemental d'installations de production et d'injection de biométhane dans les réseaux de gaz naturel - Rapport de synthèse des suivis. 91 pages.

Table 0.1: *Natural gas composition in Germany originating from Russia (RU), Norway (NO), Denmark (DK), Netherlands (NL) and Germany (DE), expressed in vol. %. H and L in parentheses stand for gases of high and low calorific value (Adelt et al. 2010).*

	RU (H)	NO (H)	DK (H)	NL (L)	DE (L)
CH_4	97.64%	87.81%	87.76%	83.18%	87.14%
C_2H_6	0.99%	7.63%	6.64%	4.05%	0.73%
C_3H_8	0.32%	1.32%	2.92%	0.71%	0.06%
C_4H_{10}	0.10%	0.24%	0.96%	0.23%	0.03%
C_5H_{12}	0.01%	0.02%	0.16%	0.05%	-
Higher HC	0.01%	0.02%	0.03%	0.05%	-
N_2	0.84%	0.96%	0.33%	9.94%	9.76%
CO_2	0.09%	2.00%	1.20%	1.79%	2.28%

Another example is the injection of hydrogen, which is not a natural component of natural gas. The idea is to convert surplus electricity produced by renewable sources into hydrogen through electrolysis process. In this way the natural gas network is used at the same time as a means of energy transport and storage. In France, the demonstrative project of GRHYD* in Dunkerque is initiated by ENGIE to evaluate its technical feasibility, with up to 20% vol. hydrogen injected into the natural gas. A more audacious example is the H21 project in Leeds†, in which a switch to 100% hydrogen is envisaged. These evolutions of natural gas network result in more intense variations of gas compositions encountered by end users.

The Wobbe index (WI) is a commonly used parameter to judge the interchangeability of fuel gases. It is defined as the ratio of the high heating value (HHV) and the square root of the relative gas density with respect to the air density:

$$\mathrm{WI} = \frac{\mathrm{HHV}}{\sqrt{\rho_{gaz}/\rho_{air}}} \tag{0.1}$$

When the gas injection obeys the Bernoulli equation, the volumetric flow rate is proportional to $\rho_{\mathrm{gaz}}^{-1/2}$. Therefore Wobbe index actually indicates the power output with a fixed valve opening. For fuels with the same Wobbe index and with the same pressure in the feeding line, the power released remains constant. The EN437 standard defines an authorized Wobbe index range of 45 to 54 $\mathrm{MJ/m^3}$. Up to now, the Wobbe index variations in the network are much

*GRHYD: Gestion des Réseaux par l'injection d'Hydrogène pour Décarboner les énergies (refer to https://www.engie.com/innovation-transition-energetique/pilotage-digital-efficacite-energetique/power-to-gas/projet-demonstration-grhyd/)

†https://www.northerngasnetworks.co.uk/wp-content/uploads/2017/04/H21-Report-Interactive-PDF-July-2016.compressed.pdf

smaller than the authorized range and are generally geographical, *i.e.*, variations over time within a given geographical zone are limited. This situation is however expected to change in the future.

Current boiler control strategy

Domestic gas boilers are usually equipped with premixed burners with a large turn-down ratio. The air flow rate is regulated by the fan speed. A pneumatic control method is often adopted to ensure a correct fuel/air ratio at different loads. In Fig. 0.1, the pressure before and after the injector are respectively $p^{\mathrm{u}}_{\mathrm{air}}$, $p^{\mathrm{d}}_{\mathrm{air}}$ for air and $p^{\mathrm{u}}_{\mathrm{fuel}}$, $p^{\mathrm{d}}_{\mathrm{fuel}}$ for natural gas. Calculations of the gas flow rate through an orifice can be found in Jones (1989). A simplified analysis with Bernoulli's equation assuming zero loss at the orifice shows that the volumetric flow rate is proportional to the square root of the pressure drop divided by the gas density:

$$\dot{V}_{\mathrm{air}} = K_{\mathrm{air}} \sqrt{\frac{p^{\mathrm{u}}_{\mathrm{air}} - p^{\mathrm{d}}_{\mathrm{air}}}{\rho_{\mathrm{air}}}} \tag{0.2}$$

$$\dot{V}_{\mathrm{fuel}} = K_{\mathrm{fuel}} \sqrt{\frac{p^{\mathrm{u}}_{\mathrm{fuel}} - p^{\mathrm{d}}_{\mathrm{fuel}}}{\rho_{\mathrm{fuel}}}} \tag{0.3}$$

A special valve automatically adjusts the gas pressure $p^{\mathrm{u}}_{\mathrm{fuel}}$ to be equal to that of the air $p^{\mathrm{u}}_{\mathrm{air}}$. Also, $p^{\mathrm{d}}_{\mathrm{air}}$ equals $p^{\mathrm{d}}_{\mathrm{fuel}}$, which corresponds to the pressure of fuel/air mixture. In this case, the ratio of fuel and air flow rate only depends on the coefficients K_{air} and K_{fuel}, when the density variations can be neglected:

$$\frac{\dot{V}_{\mathrm{air}}}{\dot{V}_{\mathrm{fuel}}} = \frac{K_{\mathrm{air}}}{K_{\mathrm{fuel}}} \sqrt{\frac{\rho_{\mathrm{fuel}}}{\rho_{\mathrm{air}}}} = cst. \tag{0.4}$$

This ratio can be changed by adjusting the valve opening and this operation is done in factory or during the installation according to the local conditions.

Combustion control system

Variations of the gas composition set a challenge for domestic gas boiler manufacturers to maintain optimized performances of the product. Condensing boilers now are equipped with full premixed burners and work with a certain amount of excess air to ensure a complete combustion. The fuel-air equivalence

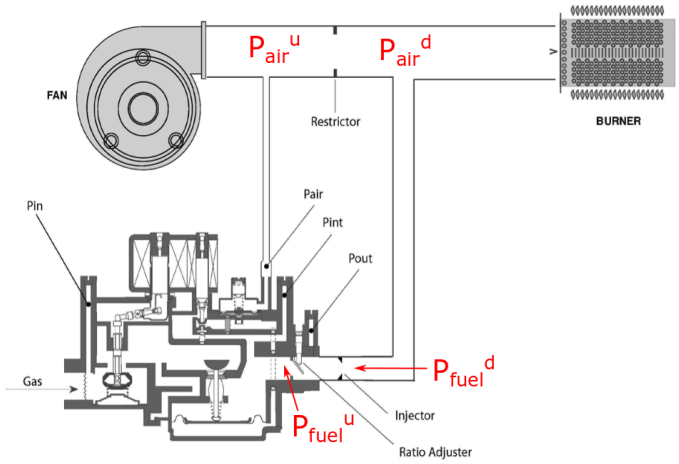

Figure 0.1: *Pneumatic control of fuel and air flow rate (SIT Group document).*

ratio is often used to characterize the operation point of premixed burners:

$$\phi = \frac{(\dot{m}_{\text{fuel}}/\dot{m}_{\text{air}})}{(\dot{m}_{\text{fuel}}/\dot{m}_{\text{air}})_s} \tag{0.5}$$

where $\dot{m}$ stands for the mass flow rate and the index s corresponds to stoichiometric combustion conditions. For gaseous fuels, under the ideal gas assumption, $\dot{m}$ can be replaced by the volumetric flow rate $\dot{V}$ in Eq. (0.5). Alternatively, the air excess factor $\lambda = 1/\phi$ is also often used in the industry to characterize the combustion state.

Insufficient excess air may result in dangerous carbon monoxide emissions due to incomplete combustion. Also, a higher flame temperature promotes the production of nitrogen oxides. On the other hand, too much excess air would compromise the efficiency of the device, and also cause flame detachment, prone to carbon monoxide production as well (Jones 1989). A compromise is therefore necessary and the equivalence ratio, or air excess factor, should be maintained within an optimized range (Lee et al. 2011b).

The current control strategy makes the boiler to work at preset equivalence ratios chosen to obtain optimized performances. In view of the future gas composition variations, this strategy may no longer be sufficient. Instead, a control loop is necessary, which monitors in real time the flame state and accordingly regulates the fuel/air ratio (Fig. 0.2).

The first step for the development of a combustion control loop is to gain reliable information about the gas conditions or the combustion state. A brief description of the available sensor technologies and potential equivalence ratio monitoring methods are given in the following sections.

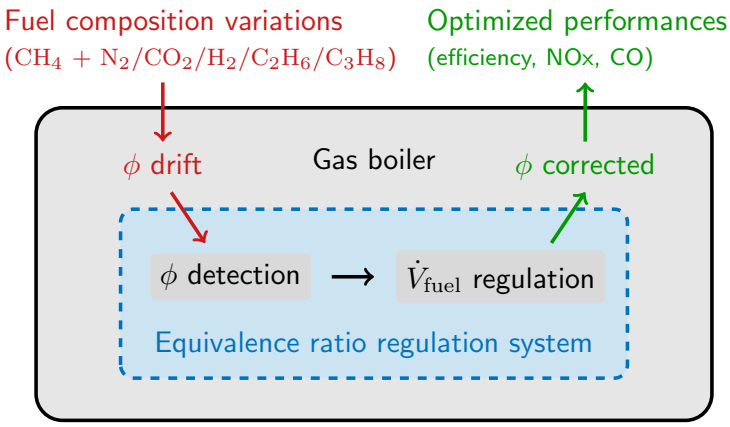

Figure 0.2: *Combustion control system.*

Sensors for combustion monitoring

The technical solutions are often classified in three categories depending where the diagnostic is made:

- Upstream the combustion: *Analysis of the supplied gas composition*
- Inside the combustion chamber: *Monitoring of combustion state*
- Downstream the combustion : *Analysis of flue gases*

Both the upstream analysis of natural gas and the downstream analysis of flue gases require gas sensors indicating the gas composition. Reviews on the available sensor technologies have been done for example by Docquier and Candel (2002) and by Tschulena and Lahrmann (2006). Table 0.2 is taken from Tschulena and Lahrmann (2006) showing some relatively low cost sensor technologies possibly applicable to combustion monitoring in household boilers. However, all the cited sensor technologies do not necessarily fulfill the requirements for flame monitoring purpose, due to cost, endurance, and cross-sensitivity, *i.e.*, sensors reacting to substances other than the targeted gas component. Some sensors are based on the measurement of physical properties of gas mixtures, such as the dielectric constant, speed of sound or heat conductivity. They may not be sufficient for the analysis of the fuel blend or flue gas compositions as they are generally not enough selective. The so-called pellistors may give useful information on the concentration of flammable gases through catalytic conversion. However, they are so far only designed to serve as guarding sensors in rooms with a risk of flammable gas leaking. Analyzers based on light absorption are able to give more reliable and precise information on a variety of gas components, but their complexity makes them difficult to be integrated

Table 0.2: *Gas sensor principles (Tschulena and Lahrmann 2006).*

Functional principle	Detectable gases
Dielectric constant	CO_2, H_2O
Speed of sound	Binary gaseous mixtures
Optical principles	CO_2, CO, CH_4, NO, NO_2, SO_2
Heat conduction	H_2, CH_4
Heat of reaction	combustible gases
Electrochemical cells with liquid electrolyte	O_2, CO, NO, NO_2, SO_2, H_2
Electrochemical cells with solid electrolyte	O_2, H_2, CO
Semiconductors	O_2, H_2, CO, CH_4, NO_2, Cl_2

in domestic gas boilers. Certain technologies, like electrochemical cells with a liquid electrolyte, do not have a sufficient life span for a permanent monitoring over a period of 10 years.

A complete analysis of all the natural gas components is generally difficult. Instead, it is possible to statistically relate some physical properties of gases, *e.g.* its density, viscosity, thermal conductivity, speed of sound, refractive index, etc., with some useful information for the operation point regulation, *e.g.* its heating value, Wobbe index or methane number*. Usually the number of physical parameters needed to monitor is less than the number of gas components. Rahmouni et al. (2003) have classified the natural gas components into three groups: methane, heavier alcanes (C_2H_6, C_3H_8, C_4H_{10}) and inert components (N_2, CO_2). The low heating value and methane number of the natural gas can for example be deduced from a measurement of the thermal conductivity at 30 and 80 °C. Other examples with approaches based on statistical correlations are summarized in Schley et al. (2003). A particularly interesting example is that the Wobbe index of natural gas can be directly related to the dynamic viscosity of the combustible mixture (Pickenäcker et al. 2000) and more details on this technique are given in the following section.

Potential methods for equivalence ratio monitoring

Wobbe index monitoring

The Wobbe index is a useful parameter for the equivalence ratio regulation. As explained above, this index is a measure of the thermal power for a fixed valve opening. In addition, the heat of combustion is approximately proportional to the oxygen required for a stoichiometric combustion. This correlation is valid

*Measure of resistance of fuel gases to engine knock

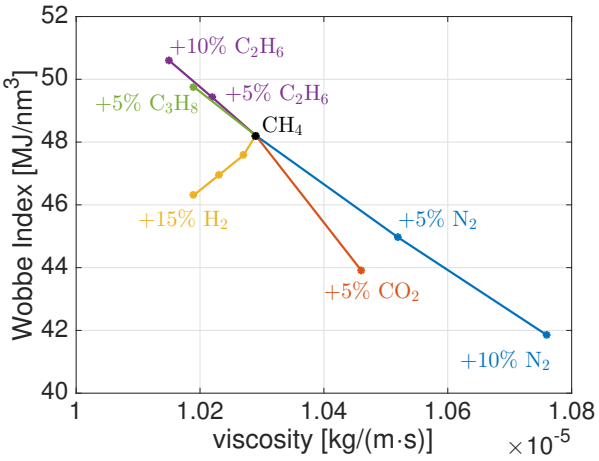

Figure 0.3: *Correlation between the Wobbe index and gas dynamic viscosity (calculation based on Le Corre and Loubar (2010)).*

for all major components of natural gas (light alcanes, inert gases like N_2 and CO_2) and to a lesser extent for H_2 as well. As a result, the knowledge of the Wobbe index alone is sufficient to determine the necessary air flow rate.

The Wobbe index can be obtained by measuring respectively the heating value and density of the natural gas. Miniaturized sensors using this method have been developed (Lötters et al. 2013). Alternatively, as mentioned above, the Wobbe index can also be deduced from a measurement of the dynamic viscosity (Pickenäcker et al. 2000). With the Matlab code provided by Le Corre and Loubar (2010), the dynamic viscosity is calculated for binary gas mixtures consisting of methane and one of the following components: ethane, propane, hydrogen, nitrogen or carbon dioxide. The Wobbe index of the gas blends are drawn as a function of the resulting viscosity values in Fig. 0.3, which helps to understand the correlation between these two parameters and reveals its limit of applicability. The data for light alcanes (methane, ethane, propane) and nitrogen, which are the major components of natural gas, form a straight line in this figure. Mixtures with CO_2 slightly deviate from this line, while the injection of H_2 does not conform to this correlation at all. However, in natural gases, the CO_2 content is generally low while H_2 is not an intrinsic component. This correlation is therefore valid for natural gases with a high precision in the absence of CO_2 and H_2.

This correlation has promoted the development of Wobbe index sensors based on the measurement of the gas mixture dynamic viscosity. A miniaturized solution has been proposed at EPFL (Slater et al. 2010). However, despite these innovations, these sensors are still too complex and expensive to be used in household gas boilers.

Flue gas analysis

The fuel/air equivalence ratio can be related with the volumetric fraction of certain components in the dried flue gases.

The first example is the residual oxygen content. The relationship between the equivalence ratio and the volumetric fraction of residual oxygen in the dried flue gases $X_{O_2}^{\text{dried}}$ depends on the natural gas composition. However, considering that the change of mole numbers before and after combustion can be neglected, the relationship can be simplified as:

$$\phi \sim 1 - \frac{X_{O_2}^{\text{dried}}}{0.21} \tag{0.6}$$

A low-cost solution for oxygen content analysis is the lambda probe, developed first by Robert Bosch GmbH in the 1970s and widely used in automobiles, industrial burners and biomass boilers. Nevertheless, it is questionable whether its measurement precision is sufficient for equivalence ratio analyses in gas boilers.

Another potential indicator for the equivalence ratio is the content of CO_2 in the flue gases. For methane combustion the relationship can be written as:

$$\phi = \frac{9.52}{1 + 1/X_{CO_2}^{\text{dried}}} \tag{0.7}$$

This expression is only valid at lean and stoichiometric conditions and also depends on the natural gas composition. Yet as long as the fraction of other components are small in the natural gas, $X_{CO_2}^{\text{dried}}$ remains an acceptable and convenient indicator of equivalence ratio. It is commonly used during factory tests or boiler maintenance. However, for a real time monitoring, no appropriate CO_2 sensors are available (see Tab. 0.2). The existing sensors are either too complex and expensive (optical analyzers) or too fragile (electrochemical cells) for permanent measurements.

The content of carbon monoxide is also exploited in the combustion monitoring and low cost miniaturized CO sensors have also been developed (*e.g.* CarboSen, Lamtec GmbH). It is a straightforward indicator for the quality of combustion and also an important parameter to monitor for security reasons. However, it does not yield the equivalence ratio with precision. Indeed, a well designed burner produces very low CO levels over a large range of equivalence ratios, and the curve of CO molar fraction X_{CO} vs. equivalence ratio ϕ features a U shape with a wide and flat bottom.

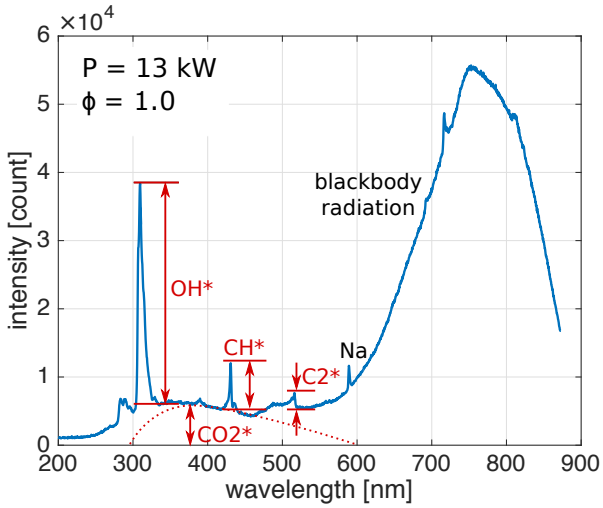

Figure 0.4: *Typical spectrum of methane-air flame stabilized on a cylindrical multi-perforated burner.*

Flame chemiluminescence

Flame chemiluminescence refers to the spontaneous light emission from flames. It is the result of the transition of excited radicals created during the combustion process to their ground states. The radicals at excited states are denoted by the superscript $*$. Figure 0.4 shows a typical spectrum taken from a cylindrical multi-perforated burner used in domestic gas boilers. It contains light emissions from different origins. The remarkable continuous emission above 500 nm is attributed to the blackbody thermal radiation from the hot burner surface. The drop of the signal observed for the wavelengths above 750 nm is unphysical and is due to the apparatus, which was not calibrated for these measurements (Section 2.3.2). Due to salt deposition on the burner surface, a narrow peak emission due to sodium is visible at 589 nm, especially when the burner is operating at high temperature. The flame chemiluminescence concerns the emissions of OH^* at 309 nm, CH^* at 431 nm, C_2^* at 516 nm, and CO_2^* from 300 to 600 nm. The emission peaks are not monochromatic due to different vibrational and rotational energy levels. The fine structures are however invisible in Fig. 0.4 with the resolution of the spectrometer used.

These emission intensities are related to the equivalence ratio of the combustible mixture. This can be understood thanks to the schematic of methane-air reactions proposed by Najm et al. (1998) as shown in Fig. 0.5. Indeed the flame equivalence ratio changes the preferred path of the combustion process, thus modifying the chemiluminescence intensities. Its potential application to flame equivalence ratio monitoring has been extensively discussed in the scientific literature. However, studies focusing on its industrial application in domestic gas

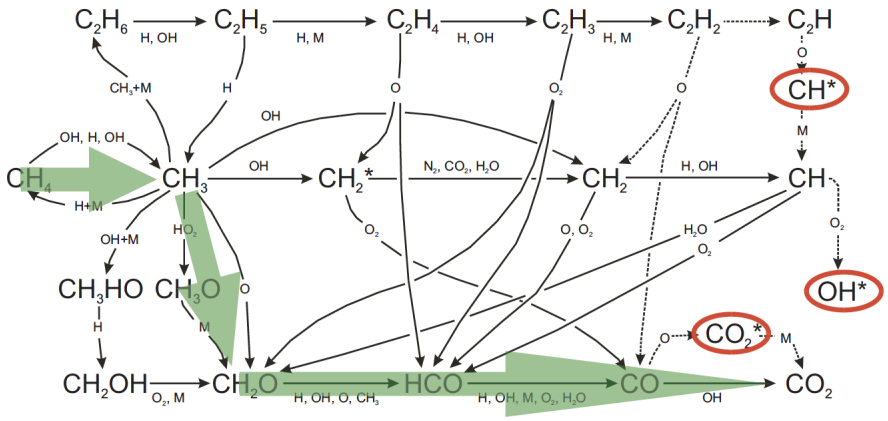

Figure 0.5: *Simplified schematic of methane combustion reactions. The bold arrows indicate the major reaction path followed by the carbon (Najm et al. 1998; Lauer 2011).*

boilers are still lacking. Detailed experimental and numerical investigations of this signal are presented in the present thesis.

Flame ionization current

The flame can be considered as a weakly charged plasma and has a certain level of electrical conductivity due to the ions and electrons created during the reactions. The ions are mainly formed by two mechanisms: thermal ionization and chemi-ionization. In the case of a laminar flame under atmospheric pressure, the chemi-ionization is dominant. For lean methane-air flames, the major reactions contributing to the formation of ions include (Franke 2002):

$CH + O \rightarrow CHO^+ + e^-$	initialization
$CHO^+ + H_2O \rightarrow CO + H_3O^+$	proton exchange
$H_3O^+ + e^- \rightarrow H_2O + H$	recombination
$e^- + O_2 \rightarrow O_2^-$	electron attachment

The CHO^+ radical is first created by the collision of CH and O. It is then immediately transformed into H_3O^+. The electron formed in the initialization reaction can either be recombined with H_3O^+ or captured by O_2, especially at low temperature and with high oxygen concentrations. In a fuel rich flame ($\phi > 1$) $C_3H_3^+$ should also be taken into account (Franke 2002).

When a voltage is applied to the flame, an ionization current can be measured. In a gas boiler, the voltage is applied between an ionization probe exposed to the flame and the metallic burner surface, used as the second electrode. According

to previous studies (Franke 2002; Rodrigues 2005), the drop of electric potential takes place almost entirely around the cathode. In order to get a strong current, a big cathode surface area is necessary, while the surface area of the anode is not as important.

The ionization current technique is widely used in domestic gas boilers, but initially only as a flame detector. More recently, applications to equivalence ratio monitoring are emerging (Näslund 2014), and exploiting the ionization current receives interests from many gas boiler manufacturers, thanks to the low cost, simplicity and relatively high maturity of this technology. This technique is investigated in the second part of the manuscript.

Thesis objective and content

The present thesis is part of the ZEM-R project initiated by Bosch Thermotechnologie and supported by FUI (Fonds Unique Interministériel), with the aim of developing a combustion control system for domestic gas boilers. The targeted boilers operate with premixed flames under atmospheric pressure and the heating power varies between 3 and 30 kW. The combustion control system is expected to regulate in real time automatically the burner operation point (power and equivalence ratio) according to the natural gas supply conditions. The objective of the thesis is to find out a control law for the monitoring of combustion state, and more specifically, the flame equivalence ratio. The work carried out examines two potential techniques of the flame chemiluminescence emission and the ionization current.

The manuscript is divided into three parts.

Part I focuses on the possibility of exploiting the flame chemiluminescence signal for the equivalence ratio monitoring. Effects of several disturbing factors are also investigated:

- Chapter 1 makes a literature review on the current knowledge on these problems. The molecular spectrum theory and the chemical reactions associated with the production of chemiluminescent species are first briefly introduced. A synthesis on the impact of various flame parameters on the chemiluminescence signal is then made. Finally, previous studies relying on the chemiluminescence to monitor the flame state are presented.

- Chapter 2 introduces the experimental facilities and the diagnostics which are used in this work. The three burner configurations and various measurement devices are presented. A detailed discussion is given on the calibration and limitation of the spectrometer used in this study to col-

lect and analyze the light signal. The possibility of using CCD sensors as a low cost alternative is briefly discussed with preliminary experiments. The methods used to measure the chemiluminescence intensity as well as the temperatures of the solid burner components and within the gaseous flow are also described in this chapter.

- Chapter 3 describes the numerical work carried out with the flow solver that is used to support the experimental studies. The governing equations and the boundary conditions of the different 1-D flame models that have been investigated, as well as the chemical kinetics adopted, are first described. The method used to determine the chemiluminescence intensity from these simulations is then explained.

- Chapter 4 makes a synthesis of the experimental data gathered for the chemiluminescence intensities with the different fuel blends investigated. Experiments are reported to understand the effects of secondary natural gas components on the chemiluminescence emission intensities of OH^*, CH^* and CO_2^*. Numerical results are then analyzed to support the experimental results. The correlation between the chemiluminescence intensity and flame temperature is briefly discussed. Finally, different equivalence ratio indicators are suggested, which serve as input data for the combustion control system in Chapter 9.

- Chapter 5 investigates the impact of the flame-burner heat exchange on the flame chemiluminescence signal. Experiments are carried out to show the evolution of the chemiluminescence intensity with the inlet gas flow rate and gas temperature, for both freely-propagating and burner-stabilized flames. The results are then completed by numerical simulations. These simulations suggest that the effects of flame-burner heat exchange on the chemiluminescence signal are mainly related to changes of the burnt gas temperature.

- Chapter 6 deals with the impact of several disturbing factors on the flame chemiluminescence. These effects need to be taken into consideration for the design of the flame monitoring system for the final application in a domestic gas boiler.

The technique of flame ionization current is studied in Part II:

- Chapter 7 briefly introduces several background notions on the flame ionization current, including the formation of charged species in hydrocarbon-air flames and electrical properties of flames under a bias voltage. A literature review on its application to flame monitoring is also made.

- Chapter 8 presents the experiments carried out on a premixed conical

flame to understand the evolution of the ionization current with the probe position, gas velocity, fuel composition and equivalence ratio. A new equivalence ratio sensing strategy is proposed coupling both the signals from the flame chemiluminescence and ionization current. Finally, the changes of the ionization current intensity with various parameters are found to be related to the distance between flame base and burner rim.

Part III shows a demonstrative equivalence ratio sensing system controlled by an algorithm developed with LabVIEW based on the findings of Part I.

- Chapter 9 first makes a synthesis of the different equivalence ratio sensing strategies. The tests are made to determine the best choice when the fuel blend composition varies. The impact of the burner temperature is explored. A control strategy is then developed and tested for different natural gas compositions.

Part I

Flame chemiluminescence

Chapter 1

Literature review on flame chemiluminescence

This chapter explains the mechanism of chemiluminescence emission from hydrocarbon flames, including the molecular spectrum theory and the chemical reactions responsible for the formation and destruction of excited species. A literature review is given for the impact of flame parameters on the chemiluminescence intensity and its potential application to flame state monitoring.

1.1 Molecular spectrum

The spontaneous light emission of a flame, denoted flame chemiluminescence, is generated when radicals at excited states created during the combustion process drop to the ground states. Unlike atomic spectra which feature monochromatic emission peaks, the peaks of molecular spectra generally have a certain width especially when observed with low-resolution devices. The energy states of molecules contain the contributions of electronic, vibrational and rotational energies. According to the Born-Oppenheimer approximation, the three components have distinct order of magnitude:

$$E_{\text{electronic}} \gg E_{\text{vibrational}} \gg E_{\text{rotational}} \tag{1.1}$$

The three types of motion can therefore be treated separately. It is known that each electronic state is split into several vibrational states, while each vibrational state is split into several rotational states. For example, the radiative

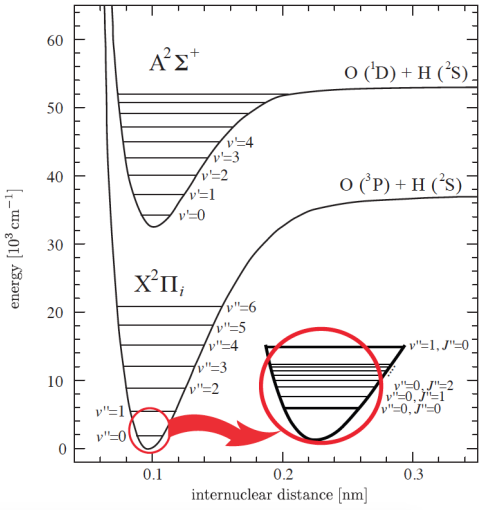

Figure 1.1: *Energy levels of OH radical (Luque and Crosley 1998; Lauer 2011).*

decay of OH* concerns the electronic state transition of $A^2\Sigma^+ \rightarrow X^2\Pi$*. Figure 1.1 shows a sketch of the energy level of the OH radical drawn by Luque and Crosley (1998) and further annotated by Lauer (2011). In Fig. 0.4, the most intense OH* emission between 300 and 320 nm results from the transitions with $\Delta v = 0$ (including $1-1$ and $0-0$). Also, a much weaker branch of $\Delta v = 1$ at 283 nm is discernible, yet the $\Delta v = -1$ branch at 346 nm is hardly visible. In the case of CH*, the stronger peak at 431 nm is attributed to $A^2\Delta - X^2\Pi(0-0)$, while two weaker peaks are discernible, *i.e.* the peak at 435 nm attributed to $B^2\Sigma^- - X^2\Pi(0-1)$ and at 389 nm attributed to $B^2\Sigma^- - X^2\Pi(0-0)$ (Luque and Crosley 1996a; Luque and Crosley 1996b). In the present study, however, only the most intense peak of each radical is retained to conduct the analysis.

*The electronic state of a molecule is denoted as $^{2S+1}\Lambda_\Omega$, where $2S+1$ is the multiplicity and Ω designates the quantum number of total angular momentum. The quantum number of the molecule's orbital momentum $\Lambda = 0, 1, 2, 3$ is denoted by the capital Greek letters Σ, Π, Δ, Φ. The letters X, A, B, C added before the annotation represent the ground state, the first, second and third excited states. The numbers in the parenthesis $(v' - v'')$ denote the quantum number of the initial and final vibrational state

1.2 Reaction kinetics

1.2.1 Chemical excitation and decay

A detailed explanation of the chemiluminescence related reactions is given by Kathrotia (2011). The process can be summarized by three types of reactions:

$$A + B \rightarrow C + X^* \qquad \text{formation} \tag{1.2}$$

$$X^* \rightarrow X + h\nu \qquad \text{radiative decay} \tag{1.3}$$

$$X^* + M \rightarrow X + M \qquad \text{collision} \tag{1.4}$$

The major formation reactions for OH^*, CH^* and C_2^* are listed below:

$$OH^*: \quad CH + O_2 \rightarrow CO + OH^* \tag{1.5}$$

$$H + O + M \rightarrow M + OH^* \tag{1.6}$$

$$CH^*: \quad C_2H + O_2 \rightarrow CO_2 + CH^* \tag{1.7}$$

$$C_2H + O \rightarrow CO + CH^* \tag{1.8}$$

$$C_2^*: \quad CH_2 + C \rightarrow H_2 + C_2^* \tag{1.9}$$

$$C_3 + O \rightarrow CO + C_2^* \tag{1.10}$$

The reactions contributing to the formation of CO_2^* are not well understood, but are often written as:

$$CO + O \rightarrow CO_2^* \tag{1.11}$$

The excited radicals X^* drops to the ground state via two channels: either by emitting a photon through reaction 1.3, or by colliding with another particle M through Eq. 1.4 and only the first channel gives rise to chemiluminescence emission. The radiative decay is therefore in competition with the collisional quenching (Geddis 2009).

With OH^* as an example, by assuming the radical radius $r \sim 10^{-10}\,\mathrm{m}$, the radical mass $m \sim 3 \times 10^{-28}\,\mathrm{kg}$, the scattering cross-section $\sigma = 4\pi r^2$, the average molecular equilibrium speed $\bar{v} = \sqrt{\dfrac{3k_BT}{m}}$, the temperature $T \sim 2 \times 10^3\,\mathrm{K}$, the molecule number density $n = \dfrac{p_{atm}}{k_BT}$, the average collision frequency can then be estimated as $\bar{Z} = \sqrt{2}n\sigma\bar{v} \sim 10^9\,\mathrm{s}^{-1}$. The reaction rate of the radiative decay can be obtained from the chemical kinetics shown for example in Tab. 3.1 and for OH^* the reaction rate constant (or Einstein coefficient) is $A = 1.45 \times 10^6\,\mathrm{s}^{-1}$. It is seen that the fraction of radiative decay is very low and of the order of 10^{-3}. More precise calculations have been carried out with 1-D flame numerical simulations, with the method explained in Section 3.3 taken from Kojima et al. (2005) and the order of magnitude is coherent with the rough estimation made here.

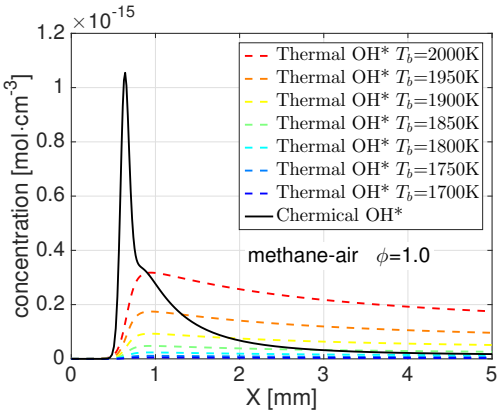

Figure 1.2: *Profiles of chemical and thermal OH* concentrations for different burnt gas temperatures.*

1.2.2 Thermal excitation

Although excited radicals are mostly created by chemical reactions during the combustion, the thermal excitation of ground state radicals constitutes another source of excited radicals. This contribution to the chemiluminescence signal is however considered to be weak below 2000 K (Nori 2008). A simple estimate is done according to the Boltzmann distribution, with the help of concentration profiles given by the 1-D flame solver described in Chapter 3:

$$c(\mathrm{OH}^*_{\mathrm{thermal}}) = c(\mathrm{OH}) \cdot \exp\left(-\frac{hc_\nu}{\lambda_\nu k_B T_b}\right) \tag{1.12}$$

where T_b is the burnt gas temperature, h and k_B the Planck and Boltzmann constants, c_ν the speed of light and $\lambda_\nu = 309\,\mathrm{nm}$ the wavelength of OH* emission. The burnt gases in the experiments are subjected to the cooling from the surrounding environment and the temperature distribution cannot be easily determined. Figure 1.2 compares the chemical OH* with the thermal OH* for different hypotheses of burnt gas temperatures T_b. It is found that when the burnt gas temperature remains high over a certain distance downstream the flame front, the thermal OH* may constitute a considerable contribution to the light emission. Regarding CH*, the contribution of thermal excitation is considered negligible since the ground state CH radicals are scarce.

1.2.3 OH self-absorption

As OH radicals are relatively abundant in the burnt gases (molar fraction $X \sim 10^{-3}$), the photons emitted by the radiative decay of OH* can be absorbed

again to form OH^*:

$$h\nu_{\sim 309\,\mathrm{nm}} + \mathrm{OH} \rightarrow \mathrm{OH}^* \tag{1.13}$$

It is recalled that the probability of the created OH^* emitting again a photon is only of the order of 10^{-3}, hence Eq. 1.13 causes a net attenuation of OH^* emission signal. The absorption intensity can be estimated with the Beer-Lambert law:

$$\frac{I_{\mathrm{residual}}}{I_0} = \exp\left(-\int_0^l k_\nu p X_{\mathrm{OH}} dl\right) \tag{1.14}$$

where k_ν is the attenuation coefficient, p the pressure, X_{OH} the OH molar fraction, l the distance from the source of light emission.

For a rough estimation, the value of $k_\nu = 20\,\mathrm{atm}^{-1}\mathrm{cm}^{-1}$ for the head of R-branch of OH $A^2\Sigma^+ \rightarrow X^2\Pi(0-0)$ band at 1735 K is taken from Davidson et al. (1996). Numerical 1-D flame simulations (described in Chapter 3) give an OH molar fraction of $X_{\mathrm{OH}} \sim 3 \times 10^{-3}$ in the burnt gases. Equation 1.14 then yields an absorption fraction of about $\sim 5\%$ at $l = 1\,\mathrm{cm}$, $\sim 25\%$ at $l = 5\,\mathrm{cm}$ and $\sim 45\%$ at $l = 10\,\mathrm{cm}$. It is reminded that other branches of OH^* emission have lower attenuation coefficients and the gas temperature also varies in the burnt gases region, therefore these calculations only give an order of magnitude. However, it is seen that the ground state OH absorption can be significant when the photon has to travel a long distance in the burnt gases before reaching the optical detector. This phenomenon has been observed in real combustion systems in the work of Guethe et al. (2012), when the flame is observed from downstream through the hot zone of burnt gases. It is also observed in the present thesis in Section 6.3.

1.3 Influence of flame parameters on the chemiluminescence

The flame chemiluminescence intensity is known to be influenced by a series of flame parameters, *e.g.* the fuel-air equivalence ratio, fuel flow rate (power), pressure, temperature, turbulence, aerodynamic stretch, etc.

The dependence of the flame chemiluminescence intensity on the equivalence ratio has been demonstrated in many studies conducted over a variety of burner configurations, such as conical flames (Nori and Seitzman 2007), swirl stabilized flames (Zimmer et al. 2003; Ballester et al. 2005) and counter-flow flames (Hardalupas et al. 2004).

For methane-air flames, the three commonly observed emissions of OH^*, CH^* and CO_2^* are generally found to increase monotonically with the equivalence

ratio within the range $0.6 < \phi < 1.0$. The modeling results of Nori and Seitzman (2007) show in addition that CO_2^* and OH^* reach their maximum value around $\phi = 0.95$ while CH^* continues to increase in the fuel rich regime at least till $\phi = 1.3$. It should be noticed that the changes of flame temperature with the varying equivalence ratio are at least partly responsible for the changes of the chemiluminescence intensity. Lee and Santavicca (2003) suggest that it is the flame temperature rather than the equivalence ratio by itself that changes the chemiluminescence intensity. This claim is supported by the numerical results from Samaniego et al. (1995) showing that for different equivalence ratios and N_2 dilutions, the CO_2^* emission intensity per unit flame surface area is correlated to the burnt gas temperature. This suggests that the equivalence ratio and dilution have the same effects on the CO_2^* emission and are both controlled by the burnt gas temperature. These numerical results are however not extended to OH^* and CH^* emissions.

At a fixed equivalence ratio, the chemiluminescence intensity is found to increase linearly with the fuel flow rate for laminar conical flames (Higgins et al. 2001) and turbulent flames up to a Reynolds number of 10,000 (Hurle et al. 1968). The linear law is however violated at highly turbulent conditions. Hurle et al. (1968) observed that CH^* and C_2^* emissions of an ethylene-air flame are lower than the linear extrapolations for Reynolds numbers above 13,000 and decrease with the fuel flow rate for Reynolds numbers above 17,000.

Chemiluminescence emissions are also observed to decrease under high pressure (Higgins et al. 2001; Higgins et al. 2001). However, a numerical approach to account for the pressure effects is difficult to carry out due to a lack of validated kinetic data at elevated pressures for the formation and quenching of OH^*, CH^* or their precursors and quenchers (Lauer 2011).

The change of relative intensity of different emission peaks from the same radical species is less investigated. This problem has been studied by Brown et al. (2008). It is suggested that the integrated intensity ratio between OH^* emission from $310-340\,nm$ and $305-310\,nm$ is well correlated to the flame temperature. It seems that these two OH^* emission bands can be roughly attributed respectively to the $A^2\Sigma^+ \rightarrow X^2\Pi$ (0-0) and $A^2\Sigma^+ \rightarrow X^2\Pi$ (1-1) transitions. This observation is also seemingly supported by the theoretical analysis of Crosley and Smith (1980).

1.4 Flame monitoring with chemiluminescence

As the flame chemiluminescence signal is sensitive to various flame parameters, it is often used to monitor the combustion state. The monitoring techniques

are generally based on empirical correlations. On the other hand, cautions are necessary to properly evaluate and exclude all interferences of irrelevant factors.

1.4.1 Heat release rate

The knowledge of the heat release rate distribution is important for the understanding and prediction of unstable combustion states (Lauer and Sattelmayer 2010). It is suggested that the chemiluminescence emissions of CH^*, OH^* and CO_2^* can be used as heat release rate markers (Clark 1958; Samaniego et al. 1995). However, Najm et al. (1998) suggest that the CO_2^* may have a complicated dependence on curvature and flow history and the chemical pathways creating OH^* and CH^* are not representative of the major pathway of carbon atoms in a methane-air flame. These authors are therefore skeptical about the correlation between the chemiluminescence emissions of these species and the heat release rate.

In the work of Lauer and Sattelmayer (2010) conducted on a swirl stabilized burner, the OH^* and CH^* emission patterns are compared with spatially resolved heat release rate distributions, which is determined with a reference technique according to the first law of thermodynamics, using data for the flow velocity deduced from particle image velocimetry (PIV), combustion progress variable from OH-PLIF, and equivalence ratio from CH^*/OH^* chemiluminescence emission ratio. It is found that the location of maximum chemiluminescence does not correspond to that of the maximum heat release rate, due to the strong flame aerodynamic stretch at the burner exit. Nevertheless, in a later study Lauer et al. (2011) found a good agreement between the OH^* emission and heat release rate when the results are corrected for the effects of the strain rate.

1.4.2 Equivalence ratio

Monitoring the combustible mixture equivalence ratio by recording the flame chemiluminescence signal is another important application and is also the major purpose of the present work. This technique applied to industrial combustion systems has recently been reviewed by Ballester and García-Armingol (2010). In practice, it is important to remove the impact of factors other than the equivalence ratio.

For this purpose, a relevant technique is to use the ratio of two chemiluminescence emissions as the equivalence ratio indicator. A common choice is the CH^*/OH^* ratio (Kojima et al. 2000). In this way, the impact of disturbing factors can be removed as long as they have similar effects on both emissions. For

example, as chemiluminescence emissions are proportional to the fuel mass flow rate (Higgins et al. 2001; Higgins et al. 2001), the CH^*/OH^* ratio is supposed to be independent of the latter. Also, the experimental work of Hardalupas and Orain (2004) with a counterflow burner revealed that the CH^*/OH^* ratio is barely modified by the strain rate. This conclusion was later verified in the numerical investigation from Panoutsos et al. (2009). They showed that even though the strain rate modifies both OH^* and CH^* emissions, the ratio of the two intensities remains unaltered by the strain rate. They however found that the C_2^*/CH^* ratio is modified by strain rate for rich flames.

A laboratory demonstrative equivalence ratio controller for a conical methane-air flame has been developed by Docquier et al. (2002), based on a lookup table consisting of two ratios OH^*/CH^* and CO_2^*/CH^*. The broadband CO_2^* emissions is represented in this study by the value recorded at 450 nm. The system was tested with success to adjust the equivalence ratio to the set value and also when the fuel is diluted with N_2. Application of this technique to industrial combustion systems has also been reported for example by Arias et al. (2008).

Nevertheless, several limitations of this technique have also been highlighted. García-Armingol et al. (2014) studied the time and space resolved OH^*/CH^* signal of swirl-stabilized turbulent flames, to evaluate its applicability to local equivalence ratio variation and thermo-acoustic instability monitoring. They found that, although the empirical correlation between OH^*/CH^* signal and equivalence ratio remains valid on the global scale, it may not be used to predict local equivalence ratio variations, as the local flame temperature and burnt gas recirculation are shown to change the value of OH^*/CH^* ratio. In addition, the chemiluminescence signal depends also on the fuel type and the effects have been addressed by several studies. Orain and Hardalupas (2010) studied the chemiluminescence of different fuels and found that the equivalence ratio calibration curve (OH^*/CH^* vs. equivalence ratio) depends on the fuel nature. García-Armingol and Ballester (2014a), García-Armingol and Ballester (2014b) studied emissions of premixed flames fueled by CH_4-CO_2-H_2-CO blends. They suggest that the OH^*/CH^* ratio should be applicable to fuels diluted with different levels of CO_2. When H_2 is added to methane, the OH^*/CH^* shows a non-monotonic behavior for an equivalence ratio $\phi > 0.75$ and in this case the OH^*/CO_2^* ratio is a better alternative. Guiberti et al. (2015) studied the effect of N_2 and CO_2 dilution on the chemiluminescence and found that they both reduce the chemiluminescence intensity of CH^*, OH^* and CO_2^* per unit flame surface area, and CO_2 dilution yields a larger drop than N_2 dilution for the same molar concentration.

This literature review indicates that the chemiluminescence signal depends on the fuel composition. In order to monitor the fuel blend equivalence ratio

with varying natural gas composition, it is important to understand the effects of secondary natural gas components on the flame chemiluminescence signal. A more comprehensive investigation is performed in Chapter 4 for laminar premixed flames.

Chapter 2

Experimental setup and methodology

This chapter describes the burners and various metrological devices used throughout the thesis. Their function principle, calibration and measurement uncertainties are discussed. The method used to determine the intensity of the different chemiluminescent species is detailed as well. Finally, an explanation is given for the determination of the temperature of the burner solid components and of the gas flow.

2.1 Burners

The aim of the thesis is to monitor the flame state on a cylindrical multi-perforated burner used in domestic gas boilers, operating with laminar premixed flames. Experiments are therefore first carried out on this commercial burner. However, it not necessarily a good model sufficiently simple for parametric analyses. Two canonical burner configurations are therefore also employed. They allow mimicking the different flame states observed on the industrial burner operating at different regimes. A conical flame burner is used as a reference for adiabatic operation of the industrial burner which prevails at high power. This burner is used to investigate the flame chemiluminescence in part I and facilitates investigation of the flame ionization current in Part II. In addition, a porous plug burner helps to understand the behavior of the flame chemiluminescence signal under non-adiabatic conditions, and ease comparisons with simulation results of 1-D flame models. Non-adiabatic conditions prevail in the radiative mode of the industrial burner at low powers. A brief description of these three burners are given in this section.

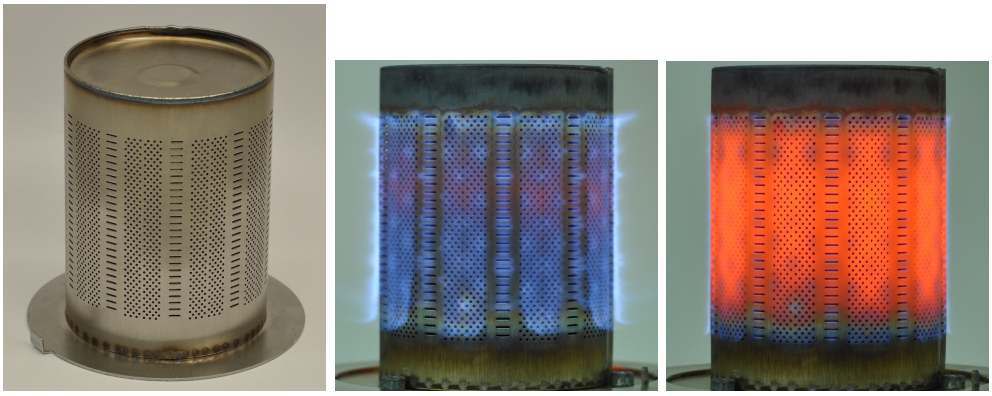

(a) Photo (b) P=9 kW $\phi = 0.83$ (c) P=3 kW $\phi = 0.83$

Figure 2.1: *Cylindrical multi-perforated burner (a), working under regular mode (b), and radiation mode (c).*

2.1.1 Cylindrical multi-perforated burner

The cylindrical multi-perforated burner shown in Fig. 2.1.a is a commercialized burner widely used in domestic gas boilers, with a diameter of 70 mm. It is made of stainless steel designed to resist high flame temperatures. The surface of the burner consists of hundreds of tiny circular holes ($\varnothing$ =0.8 mm) and rectangular slits (4 mm $\times$ 0.5 mm). Right below the surface, a set of metallic elements, including another stainless steel perforated sheet (not visible in Fig. 2.1), helps to improve the homogeneity of the gas stream distribution over the whole injection surface. The operational power covers a range of $3 - 14$ kW or $3 - 30$ kW with a slightly different internal flow guiding structure. The large power modulation range allows to meet the needs of varying heating power demand without frequent ON/OFF cycles which compromise the global energy efficiency. At high power, small blue flames are stabilized above the burner surface and the operational mode is designated as "regular" as illustrated in Fig. 2.1.b. At low power, the flames are stabilized close to burner surface with significant heat transfer to the metallic pieces. In this case, the heat is transferred to a heat exchanger through thermal radiation of the hot burner components, which works then under the so-called "radiation mode". In Fig. 2.1.c it is seen that the burner turns red due to thermal radiation of the metal at high temperature. This operation mode allows to reduce the flame temperature and mitigate NOx emissions (de Goey et al. 2011).

This commercial burner is designed according to the requirements for operation in real domestic gas boilers. It is however more difficult to handle for parametric studies aiming at a fundamental understanding of the main physical factors governing its behavior. The main issues raised by this burner are listed here:

- It is difficult to achieve an ideally uniform distribution of the gas velocity over the burner surface, despite the special internal structure of the burner injection system that was optimized to homogenize the flow. Local flame detachment may also occur especially at higher burner load.

- The flow of burnt gases is subject to natural convection and this causes a nonuniform distribution of burnt gases along the burner surface.

- A strong thermal radiation spectrum is emitted from the burner metallic surface when it is operated in the radiative mode. The characterization of the flame chemiluminesce signal can be largely perturbed by the overwhelming blackbody radiation.

- The cylindrical shape of the burner causes difficulties when studying the spatial distribution of the light emissions through image analysis. An Abel transformation would reduce effects of light integration in the line of sight, but the flame distribution over the surface is not ideally axisymmetrical and this would cause more difficulties in interpreting the results.

Therefore, apart from the cylindrical multi-perforated burner, the experiments are also carried out on two canonical burners *i.e.* a porous plug burner and a conical flame burner. The relatively simple flow pattern of these two burners allows to separately investigate the effects of the main physical parameters altering the chemiluminescence signal. The description of the two burners is given below.

2.1.2 Conical flame burner

This burner in Fig. 2.2 anchoring a conical premixed flame serves as a reference for various experiments in the present thesis. The fuel-air mixture entering the plenum passes first through a perforated plate to homogenize the flow, then through a honeycomb structure helping to laminarize it and finally through a mesh-wire grid to prevent flashback and break the residual turbulent vortices. A converging nozzle, with a contraction ratio of 8.7, guides the flow so that the gas mixture leaves the burner with a quasi-uniform top hat velocity profile (Durox et al. 1997). The nozzle outlet features a diameter of 22 mm. A ring stabilizer can be added at the top of the nozzle to improve flame stabilization and ease measurements over a large range of powers and equivalence ratios. The ring stabilizer features three slits on the top (Johnson et al. 1998). A tiny annular flame is formed above the slits helping to sustain the central conical flame. The internal diameter of the ring is 20 mm.

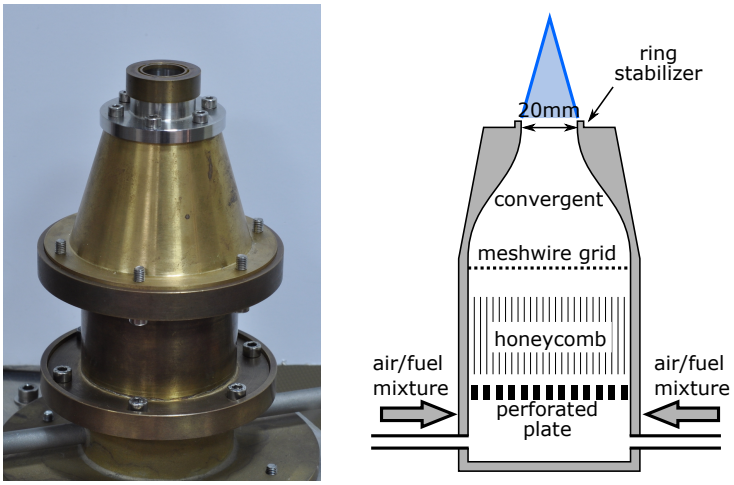

(a) Photo (b) Schematic

Figure 2.2: *Conical flame burner.*

2.1.3 Porous plug burner

The porous plug burner is a round porous plate of 35 mm diameter and 3 mm thickness, composed of packed bronze grains of 0.2−0.3 mm diameter (Fig. 2.3.c). It is supported by a stainless steel plate and fed by the fuel-air mixture with a straight duct below. An external heater can be installed upstream of the burner to investigate effects of gas preheating. An integrated thermocouple measures the gas bulk temperature leaving the heating tube. Two tiny metallic fixing lugs are installed to prevent the porous plug from being blown out by the incoming flow. The supporting plate is painted in black to minimize light reflection and avoid interferences with optical measurement devices.

For high gas injection velocities, tiny conical flames are formed above the porous plate as shown in Fig. 2.4.a. When the gas velocity drops below the laminar burning velocity S_L, the small size of the pores between the grains (of the order of 0.1 mm) eliminates the possibility of flashback. It makes the burner different from those superadiabatic burners described for example by Barra and Ellzey (2004), in which the combustion can take place inside the porous structure. With the present burner, the flame is stabilized above the porous plate with a strong heat transfer to the porous element, resulting in a (non-adiabatic) flame speed lower than the adiabatic laminar burning velocity S_L and a new equilibrium is achieved with the gas flow velocity u_0. A 1-D planar flame is then observed as in Fig. 2.4.b. In practice, the transition between conical and planar flames is progressive and the two types of flame structures can be simultaneously observed over a certain range of flow rates. This is due to the

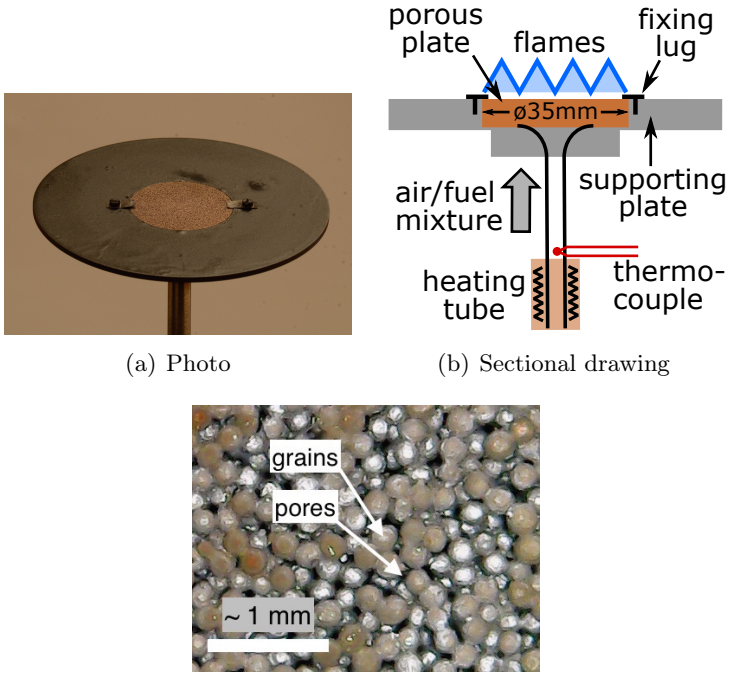

(a) Photo

(b) Sectional drawing

(c) Porous material

Figure 2.3: *Porous plug burner.*

complex porous structure of the sintered bronze, leading to a nonuniform gas velocity distribution at the porous plate outlet.

The porous plug burner is used to investigate the effects of the flame-burner heat exchange on the flame chemiluminescence signal. In addition, the simplicity of the flame geometry allows for a comparison with the numerical flow simulations with 1-D flame models.

2.2 Mass flow meter

Gas flow rates are monitored and controlled by a series of Bronkhorst EL-FLOW mass flow meters with different scales. The device is based on a heat transfer principle by measuring the temperature difference up and downstream of a heated capillary tube exposed to a by-pass gas flow. The temperature difference is related to the amount of heat absorbed by the gas flow. A signal proportional to the mass flow rate is generated:

$$\text{signal} \propto c_p \dot{m} = c_p \rho \dot{V} \tag{2.1}$$

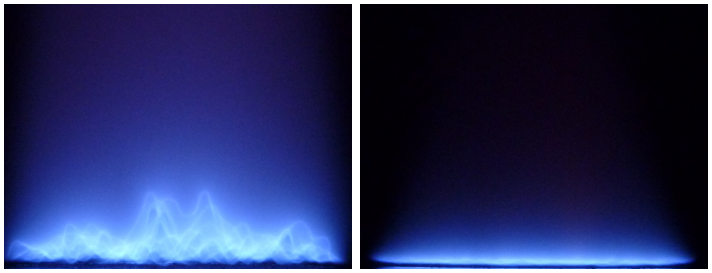

(a) $u_0/S_L = 1.41$ (b) $u_0/S_L = 0.30$

Figure 2.4: *Flames stabilized on the porous plug burner.*

Table 2.1: *Conversion factor for gas flow rate with flow meters calibrated with air (Bronkhorst product manual)*

Gas	CH_4	N_2	CO_2	H_2	C_2H_6	C_3H_8
Conversion factor	0.76	1.00	0.74	1.01	0.49	0.34

where c_p is the specific heat capacity at constant pressure, ρ the gas density, $\dot{m}$ the mass flow rate and $\dot{V}$ the volumetric flow rate. The flow rate readout is therefore only valid for the gas with which the device is calibrated. The flow meters used in the present work are generally calibrated with air. When a different gas is measured, the readout should be multiplied by a conversion factor:

$$\mathrm{CF} = \frac{\rho' c_p'}{\rho c_p} \tag{2.2}$$

where the prime stands for the calibration gas. The conversion factors taken from the product manual for the gases used in the present work are listed in Tab. 2.1. When gas mixtures (*e.g.* certification gases G25, G21, G222) are considered, the conversion factor is calculated by:

$$\frac{1}{\mathrm{CF}} = \sum_i \frac{X_i}{\mathrm{CF}_i} \tag{2.3}$$

where X_i denotes the volumetric fraction of the gas component i.

The values of mass flow rate are given with a precision of 0.1% of the flow meter capacity, which is sufficient as long as the scale is correctly chosen. The major source of error is however introduced by the conversion factor to account for the nature of gas flowing through the device. It is known with a precision of 2 decimals, leading generally to an uncertainty of about 1% abs. of the conversion factor.

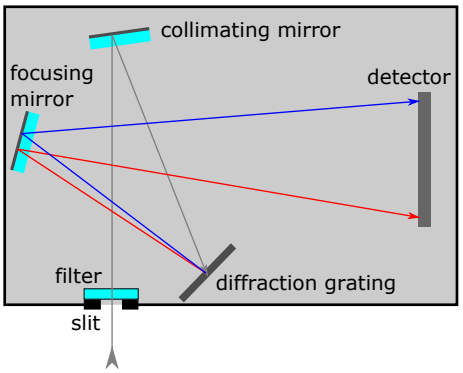

Figure 2.5: *Spectrometer configuration.*

2.3 Spectrometer

2.3.1 Principle

Figure 2.5 shows a simplified schematic of an OceanOptics USB2000+ spectrometer. Light enters the device through a slit and is collimated by a mirror. It is then diverted by a diffraction grating in different directions according to the wavelength λ_ν of the incident light:

$$a(\sin i_1 + \sin i_{2k}) = k\lambda_\nu \tag{2.4}$$

where i_1 is the angle of the incident light, i_{2k} is the diffraction angle of k^{th} order, k the order of interference and a the grating constant. After the grating, light is directed to a CCD sensor. Each pixel records the intensity of the light originating from a different direction and thus corresponding to a different wavelength.

The spectrometer uses the first order diffraction maximum ($k = 1$) to determine the spectral distribution of the incoming light. When the range of wavelengths covers more than one octave, *i.e.*, when the ratio of the maximum and minimum wavelength is greater than 2, overlapping of different orders may occur. In Eq. 2.4, the n^{th} diffraction mode order of a light source at wavelength λ_ν has the same diffraction angle as the 1^{st} diffraction mode order of a light source at the wavelength $n\lambda_\nu$. For the USB2000+ spectrometer, this problem is avoided by a high order filter.

2.3.2 Calibration

Device function

The resolution of a spectrometer is limited by its device function $A(\lambda_\nu - \lambda_{\nu 0})$, which is the response of a spectrometer to a perfectly monochromatic signal $\delta(\lambda_\nu - \lambda_{\nu 0})$, where δ is the Dirac distribution. The observed spectrum is actually a convolution of the real spectrum from the incident light $I_i(\lambda_\nu)$ by the device function:

$$I(\lambda_\nu) = \int_{-\infty}^{\infty} I_i(\lambda_\nu) A(\lambda_\nu - \lambda'_\nu) d\lambda'_\nu \tag{2.5}$$

The resolution of the spectrometer is characterized by the FWHM (full width half maximum) of the device function. For the current system it is estimated to be 2 nm, based on the measurement of a monochromatic laser at 654.4 nm.

Noise

The noise refers to random fluctuations observed over short integration times of the light source. The problem can be solved simply by averaging several measurement cycles. The total record time corresponds to the integration time for one acquisition times the number of cycles over which this measurement is repeated. Usually a total record time of several seconds is enough to suppress the random noise.

Dark background

A background signal can also be observed even without optical input. This contribution is superposed to the observed spectrum during measurements. This background signal increases with the integration time and becomes significant above 1 second. It is generally constant over time, and this property is used to make a correction. A background signal is recorded in the dark and this signal is subtracted from the measured flame spectrum. Figure 2.6 shows that this simple operation greatly reduces the interference of the dark background and improves the quality of the measured spectrum.

Stray light

Another disturbing factor is the stray light. Indeed, light entering the spectrometer does not entirely follows the desired path presented in Fig. 2.5. Light scattering on various components of the device (grating, mirrors, etc.) causes an aberrant light which shines the CCD sensor, generating a signal spreading over the whole range of wavelengths. This phenomenon can be highlighted with the spectra measured from an incandescence lamp (Planck's radiation).

Figure 2.7.a shows a series of spectra with different integration times from 20 to 320 ms. The intensity is drawn in logarithmic scale to highlight the relatively weak stray light signal. The spectra obtained for 80, 160 and 320 ms record times are partly saturated. On the ultraviolet side of the spectrum, there should

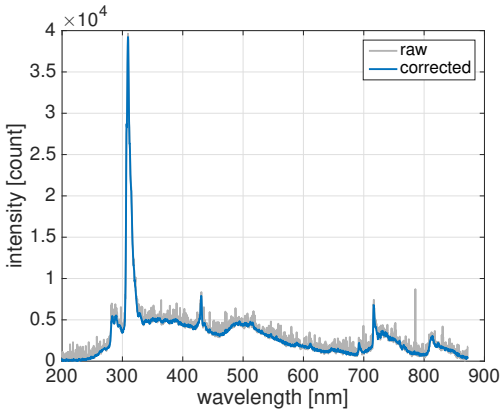

Figure 2.6: *Correction for dark noise.*

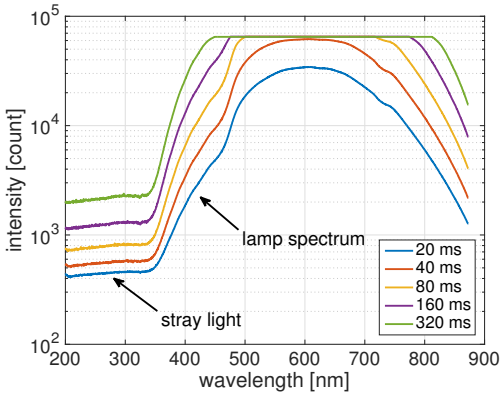

Figure 2.7: *Demonstration of stray light with an incandescence lamp.*

not be any light detection below 350 nm according to Planck's law. However, it is noticed that a signal still persists and increases with the record time, even when the sensor is not saturated. The residual signal is attributed to the stray light.

Although relatively weak compared to the overall light signal, the stray light can still result in considerable errors for flame spectrum measurements especially in the case of the cylindrical multi-perforated burner when it operates under the radiation mode. The light originating from thermal radiation can be two orders of magnitude stronger than the chemiluminescence signal, and leaves a stray light signal of similar intensity as the latter one.

When the emission intensity is studied with respect to the baseline, the stray light does not cause problems as it is corrected together with other background emissions (*e.g.* CO_2^*). However, when absolute intensities are needed, the stray light may disturb the measurements. Several methods can be proposed

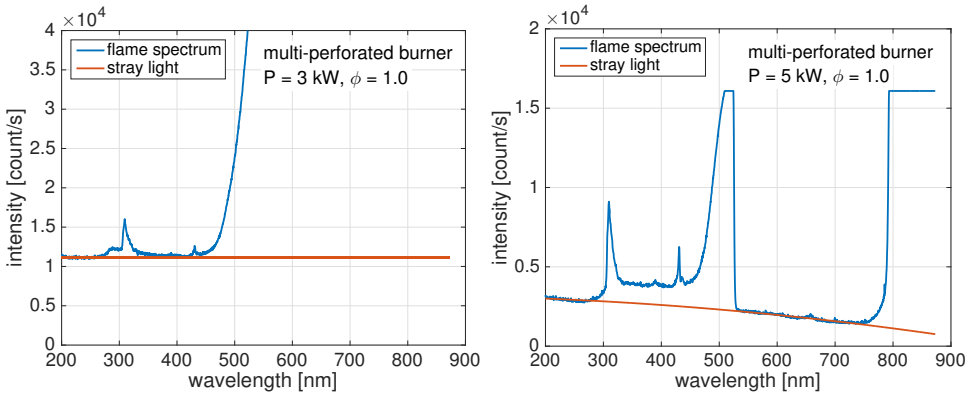

(a) Without filter (b) With filter

Figure 2.8: *Correction for stray light signal.*

to correct the stray light signal. The main idea is to find out a wavelength bandwidth where the optical signal is supposed to be zero, and the residual signal can then safely be attributed to stray light.

When studying the light emission from hydrocarbon flames, the range below 250 nm is a good candidate. By assuming a homogeneous stray light signal over the whole range of wavelengths, its contribution can be determined as shown in Fig. 2.8.a. Alternatively, when a bandpass optical filter is used, the part blocked by the filter can also be used to characterize the stray light contribution, as shown in Fig. 2.8.b, with a filter blocking the wavelengths comprised between 525 and 800 nm. It is noticed however that the stray light is not really homogeneous.

However, it remains to be verified whether these correction procedures are sufficient to eliminate the error introduced by the stray light signal. Therefore for measurements of absolute intensities (*e.g.* CO_2^*), it is advisable to use other sensors such as photomultiplier tube, when the stray light is considered to be significant.

Response as a function of wavelength

The sensitivity of a spectrometer is not constant over the whole range of wavelengths. The observed spectrum is filtered by the device response function: $I(\lambda_\nu) = I_i R(\lambda_\nu)$. The response function $R(\lambda_\nu)$ can be characterized with a standard light source whose spectrum is known. This calibration is not performed in the present work, because absolute intensity values are not needed for the present study. Instead, what is of interest is the evolutions of certain peak emissions at fixed wavelengths. Similar claims are made for example by Sandrowitz et al. (1998).

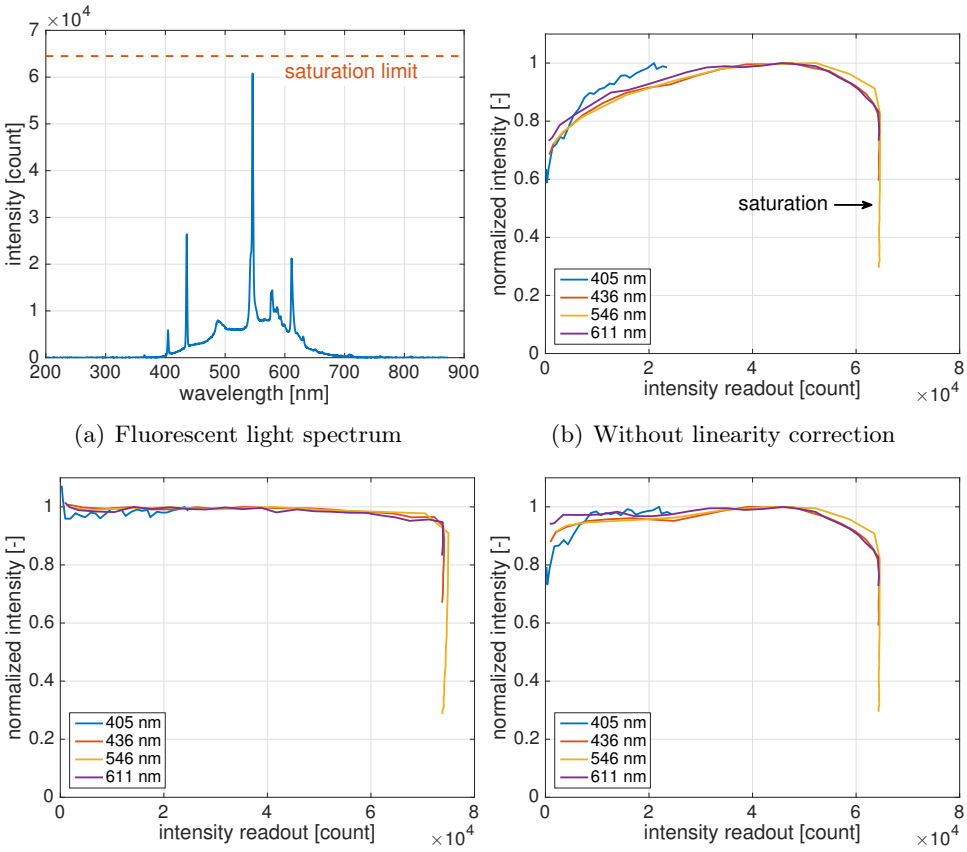

(a) Fluorescent light spectrum

(b) Without linearity correction

(c) With OceanView correction

(d) With polynomial correction

Figure 2.9: *Spectrometer response as a function of intensity readout.*

Response as a function of intensity readout

The intensity readout of a given pixel is assumed to be linear to the input light intensity, or, for a constant light source, to the integration time. To verify the linearity of the device, the fluorescent light from a neon in the room is used as the constant light source. Its spectrum (see Fig. 2.9.a), features a couple of discrete peaks superposed to a continuum, and offers a convenient solution for the calibration.

A series of spectra are recorded with increasing integration times from 50 to 5000 ms. The readout for peaks at 405, 436, 546 and 611 nm are divided by the integration time to obtain the peak intensity, which is then normalized by their maximum value. The normalized intensity (or response factor) is drawn as a function of the original intensity readout in Fig. 2.9.b. It is noticed that the linearity is valid only over a limited range of intensities between 3×10^4 and 5×10^4 counts.

The OceanView program used to record the light spectra offers an option for the non-linearity correction. this correction is based on a seventh degree polynomial stored in the device. When this correction is applied, the linearity is largely improved. As shown in Fig. 2.9.c, the response factor is constant over almost the whole intensity range before saturation, with an error lower than 3%.

The linearity correction option is however not provided in the LabVIEW module used to control the spectrometer. In this case, a manual correction is performed with a third order polynomial, based on the data in Fig. 2.9.c. As shown in Fig. 2.9.d, the operation gives a satisfactory linearity (generally below 5%) up to an intensity readout of 5×10^4 counts.

2.3.3 Spectrum correction procedure

The systematic procedure described below is followed for all the spectrum measurements shown in this work:

- A minimum acquisition time of 1 second is imposed for all the spectra recorded to limit the random noise. When the integration time is short, an averaging procedure over several cycles is adopted.

- When the integration time is above 1 second, the dark background begins to be significant. In this case, the background spectrum is recorded in the dark with the same integration time, and subtracted from the measured spectrum.

- The stray light has considerable impacts on the absolute intensity measurements (*e.g.* CO_2^* emission intensity) for the operating conditions with a strong thermal radiation component of the burners. The validity of the proposed method to suppress the stray light contribution remains to be verified. Therefore, when absolute intensities are studied, the measurements are done with a photomultiplier tube equipped with a bandpass optical filter instead.

- The device function limits the wavelength resolution to about 2 nm. No finer structure below this limit can be observed.

- The response function of the device as a function of wavelength is not calibrated. The relative intensities of two emission peaks are then changed by an unknown constant, and cannot be compared with the measurements from other devices.

- When measurements are performed with the OceanView program, the response as a function of intensity readout is corrected by the embed-

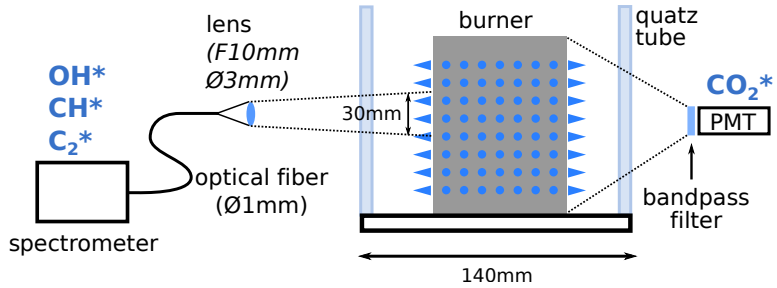

Figure 2.10: *Experimental setup for chemiluminescence intensity measurement with the cylindrical multi-perforated burner.*

ded function, which ensures a linearity over almost the whole range before saturation, with a relative error below 3%. For the LabVIEW program in Section III, the correction is done manually with a third order polynomial, which ensures a linearity for the range between 1×10^4 and 5×10^4 counts, with a relative error below 5%.

2.4 Chemiluminescence intensity measurement

The experimental setup for the measurement of the flame and burner light emissions is displayed in Fig. 2.10, with the cylindrical multi-perforated burner as an example. The corresponding optical path for the spectrometer is shown in Fig. 2.11. Light emitted by the flame is collected by a lens (F=10 mm, ⌀=3mm) and guided by an optical fiber to the spectrometer. The size of the spectrometer field of view depends on the distance between the lens and the burner and is given by $d_{\text{scope}} = (x/f)d_{\text{fiber}}$ considering $x \gg f$. The distance between the optical center of the lens and the end of the optical fiber $x' + f'$ is adjusted so that the burner leaves a net image on the fiber. In this case x' respects the Gaussian lens formula $xx' = ff'$. In practice the field of view is adjusted either to include the whole flame region or to collect the light originating from a representative region of the burner.

Figure 2.12 shows the different fields of view investigated for the three burners. The conical flame burner and the porous plug burner are observed with a view angle perpendicular to the flow direction to minimize reflection from the metallic components. The scope investigated in the case of the conical flame burner in Fig. 2.12.a is a disk of 100 mm diameter that was set to record the light from the longest flames investigated. For the porous plug burner in Fig. 2.12.b, the interrogation area has the same size (⌀ =100 mm). This field of view is bigger than the porous plate to collect all the chemiluminescence emission from the flames. In this case, the flames are stabilized at a very small distance above the

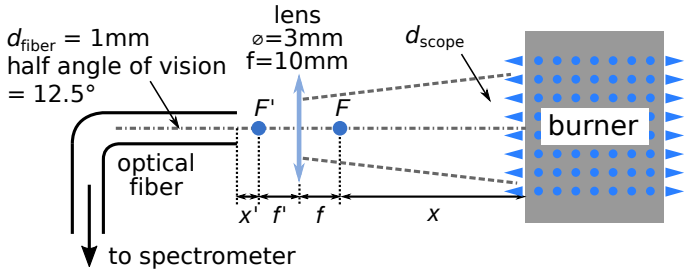

Figure 2.11: *Optical path.*

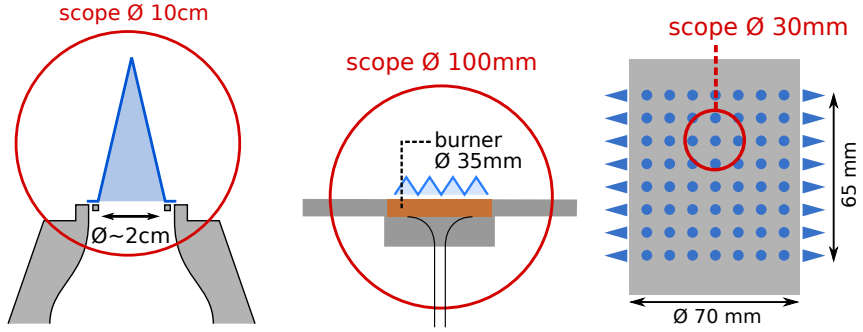

(a) Conical flame burner (b) Porous plug burner (c) Multi-perforated burner

Figure 2.12: *Spectrometer's field of view.*

burner surface and the porous plug burner is slightly inclined towards the spectrometer to ease light detection. For the cylindrical multi-perforated burner in Fig. 2.12.c, a representative circular interrogation area of ⌀ =30 mm is selected.

For the cylindrical multi-perforated burner, a quartz protection tube of 140 mm diameter and 200 mm length is set around, isolating the burner from the surrounding atmosphere (see Fig. 2.10). In addition, an optical filter blocking the light signal between 525 and 800 nm is added between the burner and the lens. It helps to attenuate the spectrum from the strong thermal radiation originating from the burner surface.

The emission intensities are determined from the recorded spectra as shown in Fig. 0.4. For narrow band emissions like OH^*, CH^* and C_2^*, the intensity can be interpreted either as the peak height or the whole peak area (García-Armingol et al. 2013). In these experiments, it is found that the shapes of the peaks are generally self-similar and the two methods yield the same results. The shapes of the OH^* and CH^* distributions for different operating conditions are presented in Appendix A to show their self-similarity. We have chosen to take the peak height. It is recalled that due to a resolution of 2 nm of the spectrometer, the

fine structures of the peaks are not visible. The baseline, consisting generally of the broadband CO_2^* emission, thermal radiation and stray light signal, needs to be removed. It is done by taking the mean value of the intensity values at the left and right limits of each peak.

The broadband emission of CO_2^* can be represented by its intensity at a certain wavelength free from other emission peaks, *e.g.* at 450 nm or 370 nm (Samaniego et al. 1995). The common choice is 450 nm. However, in the present thesis, for measurements on the multi-perforated burner, 450 nm lies close to the thermal radiation spectrum of the hot metallic pieces and its invasion at this wavelength is probable (Fig. 0.4). Therefore, it is preferred to infer this signal at the wavelength 370 nm. In addition, in order to avoid the interference of the stray light signal, all measurements of CO_2^* intensities on this burner are conducted with the photomultiplier tube mounted with a $370\,\text{nm} \pm 5\,\text{nm}$ bandpass filter.

One potential source of error with the optical setup shown in Fig. 2.11 is that the optical collection efficiency is not perfectly uniform over the interrogation area. It is found to drop slightly towards the border of the field of view. The problem mainly concerns the conical flame in Fig. 2.12.a especially when the tip of elongated flames is located in a zone with a lower collecting efficiency. Nevertheless, the flame tip constitutes a relatively small fraction of the reaction layer and the resulting relative error is estimated to be less than a few percent. Measurements on the porous plug burner and the cylindrical multi-perforated burner in Fig. 2.12.b and c are not impacted, as the flames are generally fixed in space within the field of view.

2.5 CCD image sensor

Images gathered with CCD sensors can be a very low-cost alternative solution for the chemiluminescence characterization. Although designed to record images, it can also be employed to measure simply the light emission intensity or even get information on the spectral content.

It has been proposed to use the blue and green channels from a CCD color camera to record the CH^* (431 nm) and C_2^* (516 nm) chemiluminescence emissions (Trindade et al. 2014). Nevertheless, this approximation seems too rough considering the complexity of the flame spectrum and it is preferable to couple the image sensor with a bandpass optical filter to limit the range of wavelengths recorded by the sensor.

Figure 2.13 shows a false color image of the cylindrical multi-perforated burner in operation ($P = 5\,\text{kW}$, $\phi = 1.0$) based on the blue channel signal of a webcam

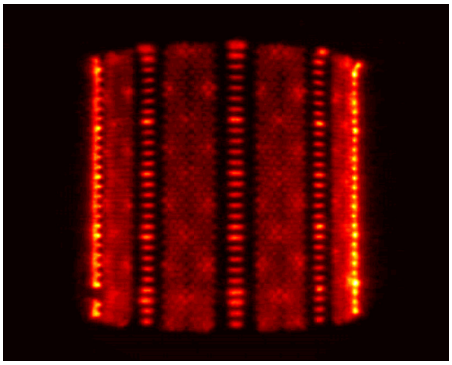

Figure 2.13: *Blue channel signal of a webcam mounted with a* $430\,\text{nm} \pm 5\,\text{nm}$ *bandpass filter presented in false color (cylindrical multi-perforated burner,* $P = 5\,\text{kW}$*,* $\phi = 1.0$*).*

mounted with a (430 ± 5) nm bandpass filter. The captured signal then includes CH^* and CO_2^* within the wavelength range. The global light intensity can be obtained by summing up the intensity values of each pixel:

$$< I^{\text{CCD}}_{(430 \pm 5)\,\text{nm}} >= \sum_{\text{all pixels}} I^{\text{CCD}} \tag{2.6}$$

where I^{CCD} is the blue channel value of the image in JPEG format. The same quantity can be obtained from the spectrometer by integrating the flame spectrum over the same range of wavelengths:

$$< I^{\text{spectro}}_{(430 \pm 5)\,\text{nm}} >= \int_{425\,\text{nm}}^{435\,\text{nm}} dI^{\text{spectro}}(\lambda_\nu) \tag{2.7}$$

The optical filter transmission is assumed to be constant for simplicity. To verify the reliability of the chemiluminescence characterization with a CCD image sensor, the intensity values obtained with the spectrometer $< I^{\text{spectro}}_{(430 \pm 5)\,\text{nm}} >$ and the webcam $< I^{\text{CCD}}_{(430 \pm 5)\,\text{nm}} >$ are drawn as a function of the equivalence ratio in Fig. 2.14 and power in Fig. 2.15. To ease the comparison, the intensity values are normalized by the intensity obtained for a flame at $\phi = 0.83$ in Fig. 2.14 and for a flame with a thermal power $P = 7\,\text{kW}$ in Fig. 2.15. It is noticed that the spectrometer curves are well reproduced by the CCD image sensor, especially when the light signal is strong, *i.e.*, at higher flame powers in Fig. 2.14 or close to the stoichiometry in Fig. 2.15.

This test with a low cost webcam demonstrates the possibility of flame chemiluminescence characterization with CCD image sensors. Nevertheless, CCD image sensors also suffer from several drawbacks. First, the OH^* emission in the UV range cannot be collected with common CCD image arrays and a special design, including the sensor and the optical system, needs to be conceived. In

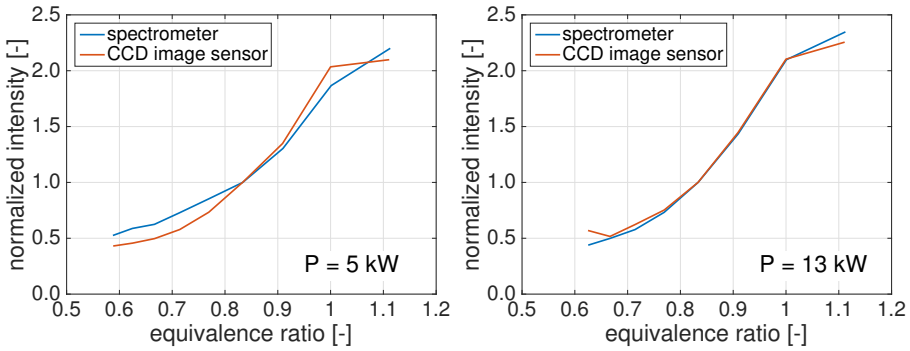

Figure 2.14: *Chemiluminescence characterization with a CCD image camera and a spectrometer: emission intensity (*$430\,\mathrm{nm} \pm 5\,\mathrm{nm}$*) vs. equivalence ratio.*

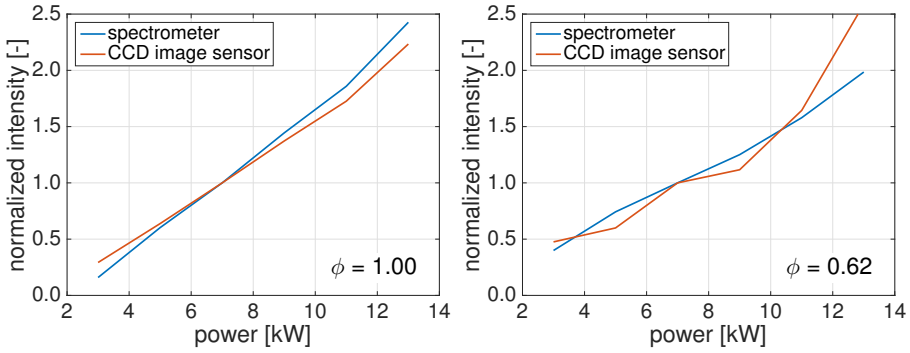

Figure 2.15: *Chemiluminescence characterization with a CCD image camera and a spectrometer: emission intensity (*$430\,\mathrm{nm} \pm 5\,\mathrm{nm}$*) vs. power.*

addition, although CCD array sensors are accessible at very low price, expensive bandpass optical filters may penalize to the total cost of the system.

The webcam is not used in the following experiments to characterize flame spectra. However, the preliminary results presented in Fig. 2.14 and Fig. 2.15 open the path to the development of new low cost sensors for flame chemiluminescence characterization.

2.6 Temperature measurement

2.6.1 Solid temperature measurement

The temperature of the solid components of the burners are monitored with a type K thermocouple. These measurements are limited to steady regimes or in regimes with small variations with time.

Alternatively, when the solid component is not accessible by the thermocouple, a Fluke 572 IR thermometer is used for a non-intrusive measurement of the solid surface temperature. This measurement is made based on Planck's thermal radiation law and a rough approximation for the surface emissivity. The sampled spot size varies with the sensor to the object distance and is indicated with two laser beams coming out of the device handle. The interrogation spot diameter reaches a minimum size of 19 mm at a distance of 1150 mm.

2.6.2 Gas temperature measurement

The temperature of the reactant stream T_0 at the burner outlet is an important parameter for the following study. When the burner is hot (especially for the multi-perforated burner and porous plug burner), preheating of the reactant stream by the burner makes the temperature T_0 much higher than the temperature T_u at which the gases are injected in the system (see Section 5.1).

A direct measurement of the temperature T_0 is difficult with the burner in operation. An alternative method is thus used to gain a rough yet reasonable estimation of the gas stream temperature at the injector outlet. The burner is first left working for several minutes until its surface temperature is stabilized. Then the fuel is turned off but the air continues to flow. A thin type R Pt/Rh thermocouple is immediately approached towards the burner surface at a distance of about 1 mm above the burner surface. The thermocouple features a bead diameter of about 100 μm and a wire diameter of about 50 μm (see Fig. 2.16.a). The response time is therefore estimated to be of the order of 30 ms (Guiberti 2015), which is sufficiently short. Nevertheless, setting the thermocouple in place takes about 1 second. The initial instant at which the flame is blown off is denoted as $t = 0$ and the temperature is then recorded over a period of 30 seconds. An exponential regression of the data and an extrapolation to $t = 0$ are used to infer the gas temperature at the burner outlet when the burner is in operation.

Figure 2.16.b is an example of the gas temperature evolution over 30 s at the porous plug burner outlet after the flame blow-off. The flow conditions for the burner in operation are $u_0/S_L = 0.29$, $\phi = 1.0$. The delay of the first point corresponds to the time necessary to set the thermocouple in place and is estimated to be (1.5 ± 0.5) s. A regression is then performed assuming an exponential drop according to Newton's cooling law :

$$T - T_e = A \exp(-Bt) \tag{2.8}$$

where T stands for the gas temperature, T_e the final temperature of the gas and t the time. The positive coefficients A and B as well as T_e are determined by a regression. It is worth noticing that T_e does not correspond to the room

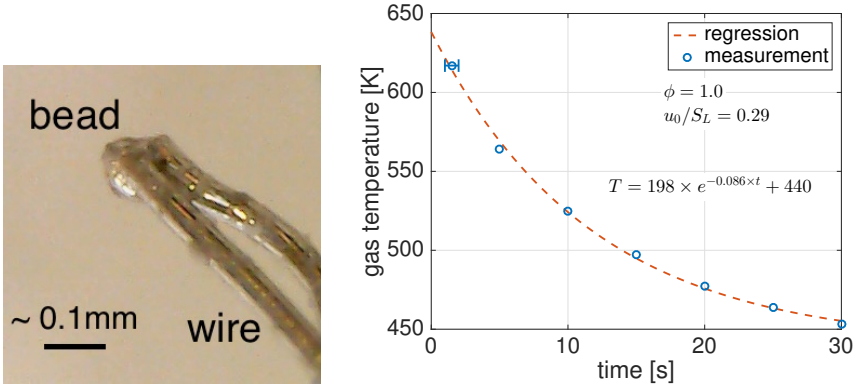

(a) Bead of the type R thermocouple

(b) Evolution of the air flow temperature after flame blow-off. $u_0/S_L = 0.29$, $\phi = 1.0$.

Figure 2.16: *Gas temperature measurement.*

temperature (*i.e.* $\sim 20\,°C$). Generally the value T_e given by the regression is slightly below the asymptotic temperature at $t = 30\,s$, which may correspond to the supporting plate temperature. An extrapolation to $t = 0\,s$ yields the gas temperature when the burner is in operation. The time uncertainty of the first point leads to an error of less than $\pm 10\,K$.

Tests were also made in which the first point of the temperature measurements was left out. It turned out that in most cases, the first measured temperature point that was left out dropped close to the regression curve calculated without considering this first measurement. These tests validate the reliability of the technique used to determine the temperature T_0 of the reactant stream at the burner outlet with the burner in operation. Repeatability tests have shown that for all cases explored T_0 could be determined in this way with an uncertainty of $\pm 40\,K$.

Chapter 3

1-D flame simulation

A numerical analysis is conducted to help interpreting the experimental observations made in the thesis. Simulations are carried out with a 1-D numerical laminar flow solver developed at EM2C laboratory including detailed chemistry and different models for flame stabilization. This code is designated in the following by REGATH. The mathematical methods for the the different flame models as well as the interpretation of the simulation results are described in this chapter.

3.1 Governing equations

The governing equations describing the 1-D multi-species reactive flow are deduced from the mass, species and energy balances at steady conditions:

$$\frac{d(\rho u)}{dx} = 0 \tag{3.1}$$

$$\rho u \frac{\partial Y_k}{\partial x} = \underbrace{-\frac{\partial(\rho Y_k V_k)}{\partial x}}_{\text{diffusion}} + \underbrace{W_k \dot{\omega}_k}_{\text{reaction}} \quad (k = 1, \cdots, N_{sp}) \tag{3.2}$$

$$\rho u c_p \frac{\partial T}{\partial x} = \underbrace{\frac{\partial}{\partial x}\left(\lambda \frac{\partial T}{\partial x}\right)}_{\text{conduction}} \underbrace{- \sum_{k=1}^{N_{sp}} \rho Y_k V_k c_{p_k} \frac{\partial T}{\partial x}}_{\text{species diffusion}} + \underbrace{\sum_{k=1}^{N_{sp}} W_k \dot{\omega}_k h_k}_{\text{reaction}} \tag{3.3}$$

where ρ is the density and u the velocity along the axial direction x. In the species balance (Eq. 3.2), Y_k is the k^{th} species mass fraction. The diffusion velocity V_k of this species is computed assuming complex transport phenomena (Giovangigli 1999). The quantities W_k and $\dot{\omega}_k$ denote respectively the molar mass and the volumetric production rate of the k^{th} species. The series of N_{sp}

conservation equations described by Eq. 3.2 has a rank of $(N_{sp}-1)$ due to the relations $\sum_{k=1}^{N_{sp}} Y_k = 1$, $\sum_{k=1}^{N_{sp}} Y_k V_k = 0$ and $\sum_{k=1}^{N_{sp}} W_k \omega_k = 0$.

In the energy balance (Eq. 3.3), T is the temperature, λ the mixture conductivity, $c_p = \sum Y_k c_{pk}$ the mixture specific heat capacity at constant pressure where c_{p_k} corresponds to the k^{th} species specific heat capacity, and h_k is the k^{th} species enthalpy. Dufour and Soret effects are neglected as well as heat transfer by radiation.

In the low Mach limit approximation the pressure is considered to be constant and the momentum conservation equation is not considered. The system of equations is completed with the state equation:

$$\rho = \frac{p_u W}{RT} \tag{3.4}$$

where W is the molar mass of the gas mixture and R the ideal gas constant. The pressure p_u is assigned to the value of atmospheric pressure p_{atm} throughout the present thesis.

It remains then to specify the production rates $\dot{\omega}_k$ appearing in Eqs. 3.2 and 3.3. Consider a reaction system with N_{sp} species χ_k $(k = 1, \cdots, N_{sp})$ and N_{rxn} reactions with the form

$$\sum_{k=1}^{N_{sp}} \nu'_{ki} \chi_k \leftrightarrow \sum_{k=1}^{N_{sp}} \nu''_{ki} \chi_k \quad (i = 1, \cdots, N_{rxn}) \tag{3.5}$$

where the integer numbers ν'_{ki} and ν''_{ki} are the stoichiometric coefficients for k^{th} species in i^{th} reaction. The production rate $\dot{\omega_k}$ of k^{th} species is given by:

$$\dot{\omega_k} = \sum_{i=i}^{N_{rxn}} (\nu''_{ki} - \nu'_{ki}) \left(\mathcal{K}_i^f \prod_{k=1}^{N_{sp}} c_k^{\nu'_{ki}} - \mathcal{K}_i^f \prod_{k=1}^{N_{sp}} c_k^{\nu''_{ki}} \right) \tag{3.6}$$

where c_k is the k^{th} species molar concentration, $\mathcal{K}_i^f$ and $\mathcal{K}_i^r$ the forward and backward reaction rate constants, related by the equilibrium constant $\mathcal{K}_i^e$:

$$\mathcal{K}_i^r = \mathcal{K}_i^f / \mathcal{K}_i^e \tag{3.7}$$

The forward reaction rate constant $\mathcal{K}_i^f$ is calculated with the Arrhenius law

$$\mathcal{K}_i^f = A_i T^{n_i} \exp\left(\frac{-E_i}{RT}\right) \tag{3.8}$$

The pre-exponential factor A_i, the exponent n_i and the activation energy E_i are taken from the detailed chemical kinetic GRI-Mech 3.0 mechanism (Smith et al.

Table 3.1: *Reactions for the formation and decay of OH* and CH* (Smith et al. 2002; Alviso et al. 2015). Reaction rate coefficient is calculated as* $\mathcal{K} = AT^n exp(-E/RT)$. *Units are mol cm cal s.*

Reaction	A	n	E
$C_2 + H_2 \leftrightarrow C_2H + H$	4.00×10^5	2.40	1000
$CH + CH \leftrightarrow C_2 + H_2$	5.00×10^{12}	0	0
$C + C + M \leftrightarrow C_2 + M$	3.00×10^{14}	0	-1000
$C + CH \leftrightarrow C_2 + H$	5.00×10^{13}	0	0
$O + C_2 \leftrightarrow C + CO$	5.00×10^{13}	0	0
$C_2 + O_2 \leftrightarrow CO + CO$	9.00×10^{12}	0	980
$CH + O_2 \leftrightarrow OH^* + CO$	6.00×10^{10}	0	0
$O + H + M \leftrightarrow OH^* + M$	3.63×10^{12}	0	0
$OH^* \rightarrow OH$	1.45×10^6	0	0
$OH^* + N_2 \leftrightarrow OH + N_2$	1.08×10^{11}	0.50	-1238
$OH^* + O_2 \leftrightarrow OH + O_2$	2.10×10^{12}	0.50	-482
$OH^* + H_2O \leftrightarrow OH + H_2O$	5.92×10^{12}	0.50	-861
$OH^* + H_2 \leftrightarrow OH + H_2$	2.95×10^{12}	0.50	-444
$OH^* + CO_2 \leftrightarrow OH + CO_2$	2.75×10^{12}	0.50	-968
$OH^* + CO \leftrightarrow OH + CO$	3.23×10^{12}	0.50	-787
$OH^* + CH_4 \leftrightarrow OH + CH_4$	3.36×10^{12}	0.50	-635
$C_2H + O \leftrightarrow CH^* + CO$	6.20×10^{12}	0	0
$CH^* \rightarrow CH$	1.86×10^6	0	0
$CH^* + N_2 \leftrightarrow CH + N_2$	3.03×10^2	3.40	-381
$CH^* + O_2 \leftrightarrow CH + O_2$	2.48×10^6	2.14	-1720
$CH^* + H_2O \leftrightarrow CH + H_2O$	5.30×10^{13}	0	0
$CH^* + H_2 \leftrightarrow CH + H_2$	1.47×10^{12}	0	1361
$CH^* + CO_2 \leftrightarrow CH + CO_2$	2.41×10^{-1}	4.30	-1694
$CH^* + CO \leftrightarrow CH + CO$	2.44×10^{12}	0.50	0
$CH^* + CH_4 \leftrightarrow CH + CH_4$	1.73×10^{13}	0	167
$C + H + M \leftrightarrow CH^* + M$	3.63×10^{13}	0	0

2000), which has been validated for methane/air combustion and methane/air fuel blends with many secondary components. Additional species and reactions (Qin et al. 2000) are included when C_2H_6 and C_3H_8 are added to the fuel mixture. Reactions for the formation and decay of the OH^* and CH^* radicals are integrated in the chemical scheme as well following Smith et al. (2002) and Alviso et al. (2015), as listed in Tab. 3.1.

3.2 1-D flame models

Two 1-D laminar premixed flame regimes are considered by imposing different boundary conditions to the previous governing equations. The first model corresponds to a freely-propagating flame and the second one considers a flame stabilized by heat losses to the burner.

3.2.1 Freely-propagating flame

In the freely-propagating regime, the reactant stream is injected at $x = -\infty$ with a temperature T^{fr} and mass fractions Y_k^{fr} for the k^{th} species, where the superscript "fr" stands for the fresh gases. At $x = +\infty$, a thermal equilibrium is achieved for the burnt gases and the temperature and mass fraction gradients tend to zero. The boundary conditions are therefore established as:

$$T|_{x=-\infty} = T^{fr} \tag{3.9}$$

$$Y_k|_{x=-\infty} = Y_k^{fr} \quad (k = 1, \cdots, N_{sp}) \tag{3.10}$$

$$\left.\frac{dT}{dx}\right|_{x=+\infty} = 0 \tag{3.11}$$

$$\left.\frac{dY_k}{dx}\right|_{x=+\infty} = 0 \quad (k = 1, \cdots, N_{sp}) \tag{3.12}$$

These boundary conditions allow to determine the solution to Eqs. 3.2 and 3.3. However, the boundary condition for Eq. 3.1 cannot be determined *a priori* because the laminar burning velocity S_L is unknown. One of the approaches adopted in the REGATH solver is to impose an arbitrary temperature value T_m at the position x_m in the middle of the temperature profile :

$$T(x_m) = T_m \tag{3.13}$$

Physically, this condition fixes the position of the flame front in the numerical domain. The additional condition Eq. 3.13 makes the mass burning flux $f = \rho u$ an eigenvalue of the system, which should be equal to $\rho_0 S_L$ to allow for a steady flame solution.

3.2.2 Burner-stabilized flame

In the burner-stabilized flame regime, one considers instead a semi-infinite region from $x = 0$ to $+\infty$. The presence of a burner is simulated by imposing the following boundary conditions at $x = 0$ for the k^{th} species mass fraction and

temperature (Smooke 1982):

$$Y_k\big|_{x=0} + \frac{\rho Y_k V_k}{f_0}\Big|_{x=0} = Y_k^0 \quad (k = 1, \cdots, N_{sp}) \tag{3.14}$$

$$(\rho u)\big|_{x=0} = f_0 \tag{3.15}$$

$$T\big|_{x=0} = T_0 \tag{3.16}$$

where $f = \rho u$ is the mass burning flux and the super or subscript 0 in the right hand sides of Eqs. 3.14-3.16 stands for the injection conditions of the reactant stream at $x = 0$. The first order boundary conditions of the temperature T and mass fraction Y_k, necessary for solving the equation system Eqs. 3.1 to 3.3, are given at $x = +\infty$ and are the same as the freely-propagating flame model, *i.e.* Eqs. 3.11 and 3.12.

In this model, it is assumed that the heat exchange between the gaseous mixture within the burner and the metallic components of the burner is fast enough for the gaseous stream to reach the chemical and thermal equilibrium at the burner outlet. It is reminded that the burner outlet corresponds to the numerical domain inlet at $x = 0$.

The mass burning flux f_0 is assigned to different values to account for different gas flow rates in the experiments. The results can be classified into three categories with respect to the laminar burning velocity S_L calculated in the freely-propagating regime:

- For $f_0 > \rho_0 S_L$ (or $u_0 > S_L$), there is no solution to this 1-D model. In practice, it means that the gas velocity u_0 exceeds the laminar burning velocity and the flame is blown away.
- For $f_0 = \rho_0 S_L$ (or $u_0 = S_L$), the model yields a solution identical to the freely-propagating flame model (see Fig. 3.1 top).
- For $f_0 < \rho_0 S_L$ (or $u_0 < S_L$), the solution corresponds to a flame attached to the burner stabilized by conductive heat loss (see Fig. 3.1 bottom).

As an illustration of the two types of solution in the burner-stabilized flame regime with $f_0 \leq \rho_0 S_L$ (or $u_0 \leq S_L$), Fig. 3.2 shows the temperature profiles over $x = 0 - 0.8\,\text{mm}$ for a stoichiometric mixture injected at $T_0 = 298\,\text{K}$ for two different mass burning fluxes $f_0 = 4.36 \times 10^{-2}$ and $4.00 \times 10^{-2}\,\text{g cm}^{-2}\,\text{s}^{-1}$. The corresponding configurations are drawn in Fig. 3.1. The mass flux $f_0 = 4.36 \times 10^{-2}\,\text{g cm}^{-2}\,\text{s}^{-1}$, corresponding to an inlet velocity $u_0 = 38.7\,\text{cm/s}$, is the maximum value yielding a solution to the problem, and corresponds therefore to an adiabatic freely-propagating flame. In this case, the temperature and all species gradient vanish at $x = 0$ (see Fig. 3.2). The other solution obtained with a lower mass burning flux $f_0 = 4.00 \times 10^{-2}\,\text{g cm}^{-2}\,\text{s}^{-1}$ features a positive

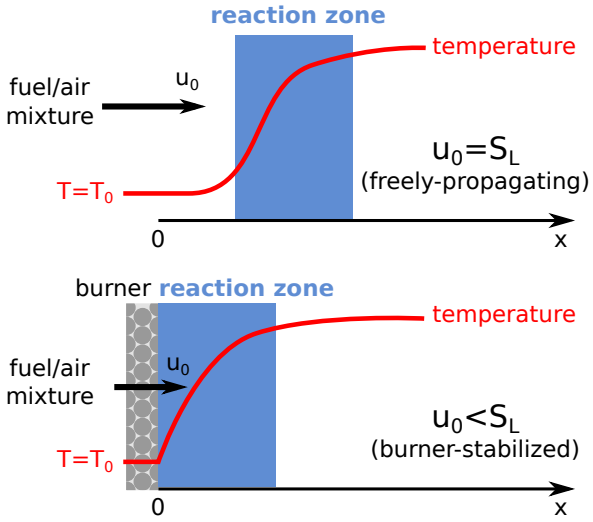

Figure 3.1: *Example of 1-D numerical freely-propagating flame (top) and burner-stabilized flame (bottom) calculated with REGATH. u_0: bulk injection velocity, S_L laminar burning velocity of an adiabatic freely-propagating flame. T_0: gas temperature at burner outlet.*

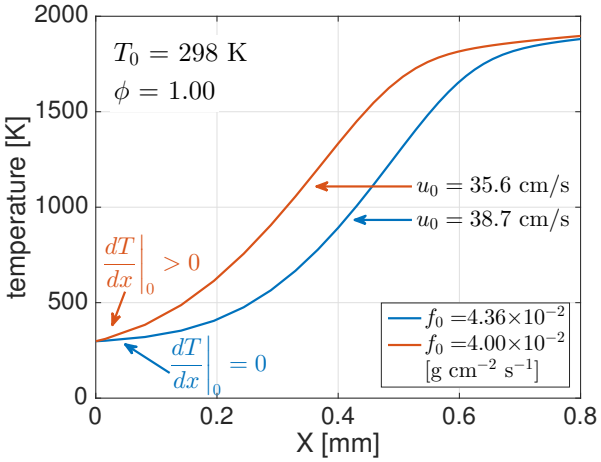

Figure 3.2: *Temperature profiles calculated with the burner-stabilized flame model for different flow rates. The temperature at $x = 0.8\,\mathrm{mm}$ is not the equilibrium temperature T_b of the burnt gases as the reaction is not complete at this point.*

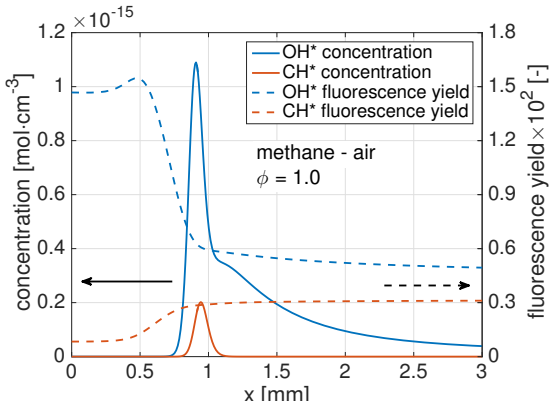

Figure 3.3: *concentration and fluorescence yield profiles of OH*, CH* radicals computed with REGATH.*

temperature gradient at $x = 0$ in Fig. 3.2, revealing a finite heat flux q towards the burner inlet:

$$q = \lambda \frac{dT}{dx}\Big|_{x=0} \tag{3.17}$$

This heat loss lowers the flame temperature and hence the flame propagation speed, until an equilibrium is achieved with the gas velocity u_0 leading to a flame stabilized by heat losses (Warnatz 1978; Joulin and Clavin 1979).

3.3 Chemiluminescence intensity

The chemiluminescence emission intensities from the OH* and CH* radicals are deduced from the concentration profiles of excited radicals given by the REGATH flow solver. In addition, as shown in the Introduction, all excited radicals do not emit a photon. Instead, most of them end up with a collisional quenching without light radiation. The method described by Kojima et al. (2005) is therefore used to take into account the fluorescence yield y_k, *i.e.* the fraction of radiative decay of the k^{th} excited radical. The chemiluminescence intensity I_k of the k^{th} excited species (OH* or CH*) can be written as:

$$I_k = y_k c_k \tag{3.18}$$

where c_k is the concentration of the k^{th} excited species. The fluorescence yield y_k is given by

$$y_k = \frac{A_{21}}{A_{21} + Q_{21}} \tag{3.19}$$

where A_{21} denotes the rate of radiative decay and Q_{21} the global rate of quenching, calculated by:

$$Q_{21} = \sum_j c_j k_j \tag{3.20}$$

with c_j the concentration of the j^{th} perturbing molecule (N_2, O_2, H_2O, H_2, CO, CO_2, CH_4) and k_j the corresponding quenching reaction rate. The quantities A_{21} and k_j can be found in the chemical reaction mechanism in Tab. 3.1(Smith et al. 2002; Alviso et al. 2015). As an example, the concentration and fluorescence yield profiles of OH^*, CH^* are shown in Fig. 3.3 for a stoichiometric methane-air flame.

Integration of the local intensity I_k over the numerical domain yields the chemiluminescence intensity per unit flame surface area.

$$< I_k >_{\text{unit surface}} = \int_0^L I_k dx \tag{3.21}$$

where the length L represents the limit of the flame front.

The chemical mechanism used for the simulations carried out in this work does not include the excited CO_2^* radical. Calculation of this signal intensity is performed with a simplified model assuming that the CO_2^* radicals are created by the combination of CO and O ($CO + O \rightarrow CO_2^*$), as proposed by Samaniego et al. (1995). The CO_2^* intensity can therefore be expressed by:

$$I_{CO_2^*} = I^0_{CO_2^*} \cdot c_{CO} \cdot c_O \tag{3.22}$$

where c_{CO} and c_O represent the concentrations of CO and O respectively. The intensity $I^0_{CO_2^*}$ is a temperature dependent function, and is given, according to Samaniego et al. (1995), by:

$$I^0_{CO_2^*} = 2.5 \times 10^6 e^{-1600/T} \tag{3.23}$$

The fluorescence yield y is not taken into account to estimate the light emission from CO_2^* radicals, due to a lack of knowledge on chemistry of this excited radical.

Chapter 4

Effects of fuel composition

This chapter aims at understanding effects of the fuel composition on the OH^*, CH^* and CO_2^* chemiluminescence intensities. The focus is put on methane/air mixtures with inert components of N_2 and CO_2 and secondary fuel components including C_3H_8, C_2H_6 and H_2. Experiments are carried out with the conical flame burner and the cylindrical multi-perforated burner. They are followed by numerical simulations of 1-D flames with the REGATH flow solver. The relationship between the chemiluminescence intensity and the flame temperature is briefly discussed. Based on the experimental results, the choice of equivalence ratio indicators for the flame monitoring system is discussed.

4.1 Chemiluminescence intensity vs. secondary component percentage

The aim of this work is to use the flame chemiluminescence to monitor the combustion state when the composition of the natural gas varies. It is therefore important to understand the effects of gas composition on the chemiluminescence intensity.

Apart from methane, the major secondary components of natural gases include nitrogen, carbon dioxide, ethane, propane and other higher hydrocarbon fuels (Tab. 0.1). Hydrogen may also be added to the list considering the ongoing discussion of injecting hydrogen into the gas network as mentioned in the Introduction. In this chapter, five secondary components are considered, including N_2, CO_2, H_2, C_2H_6 and C_3H_8. The concentration of the other components, such as heavier hydrocarbons, are generally negligible in the natural gas, with

Table 4.1: *Experimental conditions for the investigation of effects secondary natural gas components on the chemiluminescence intensity.*

Burner	Fuel	ϕ	P [kW]	X^{fuel}
Conical flame	CH_4/N_2	0.83	1.3	0 - 0.2
Conical flame	CH_4/CO_2	0.83	1.3	0 - 0.2
Conical flame	CH_4/H_2	0.83	1.5	0 - 0.2
Conical flame	CH_4/C_2H_6	0.83	1.5	0 - 0.2
Conical flame	CH_4/C_3H_8	0.83	1.5	0 - 0.2

volumetric fractions below 1%. Also, their behaviors can be inferred from the results of the five secondary components investigated.

Experiments are first carried out with the conical flame burner (Fig. 2.2). To evaluate the effects of secondary components, N_2, CO_2, H_2, C_2H_6, C_3H_8 are progressively added to methane from $X^{\text{fuel}} = 0$ to 20% where X^{fuel} represents the volumetric fraction of the secondary component with respect to the methane and secondary component blend, while the power and equivalence ratio are kept constant.

The test conditions are summarized in Tab. 4.1. The flame power is lowered for N_2- and CO_2-diluted flames to avoid flame blow-off. When the secondary component is a combustible (H_2, C_2H_6, C_3H_8), the power and equivalence ratio values refer to the air/methane/secondary component mixture.

Numerical simulations with the REGATH flow solver are performed at the same operating conditions to compare the results with the experimental data. The chemiluminescence intensity per unit flame surface area given by Eq. 4.1 is divided by the thermal power to obtain the intensity per unit power :

$$< I >_{\text{unit power}} = \frac{\int_0^L I dx}{\rho_0 u_0 \sum_k Y_k \Delta h_k^0} \tag{4.1}$$

where Δh_k^0 is the reaction enthalpy per unit mass of the k^{th} combustible species (CH_4, H_2, C_2H_6, C_3H_8).

The chemiluminescence intensities of OH^*, CH^* and CO_2^* obtained from experiments and numerical calculations are normalized by their values for the pure methane case, and plotted as a function of the secondary component fraction in Fig. 4.1. The experimental results are denoted by circles with error bars and the numerical results correspond to the dashed lines. They are split in two groups (N_2, CO_2 and H_2 in the left column and C_2H_6 and C_3H_8 in the right column) to allow for an appropriate y-axis scale for each curve. Also, in the

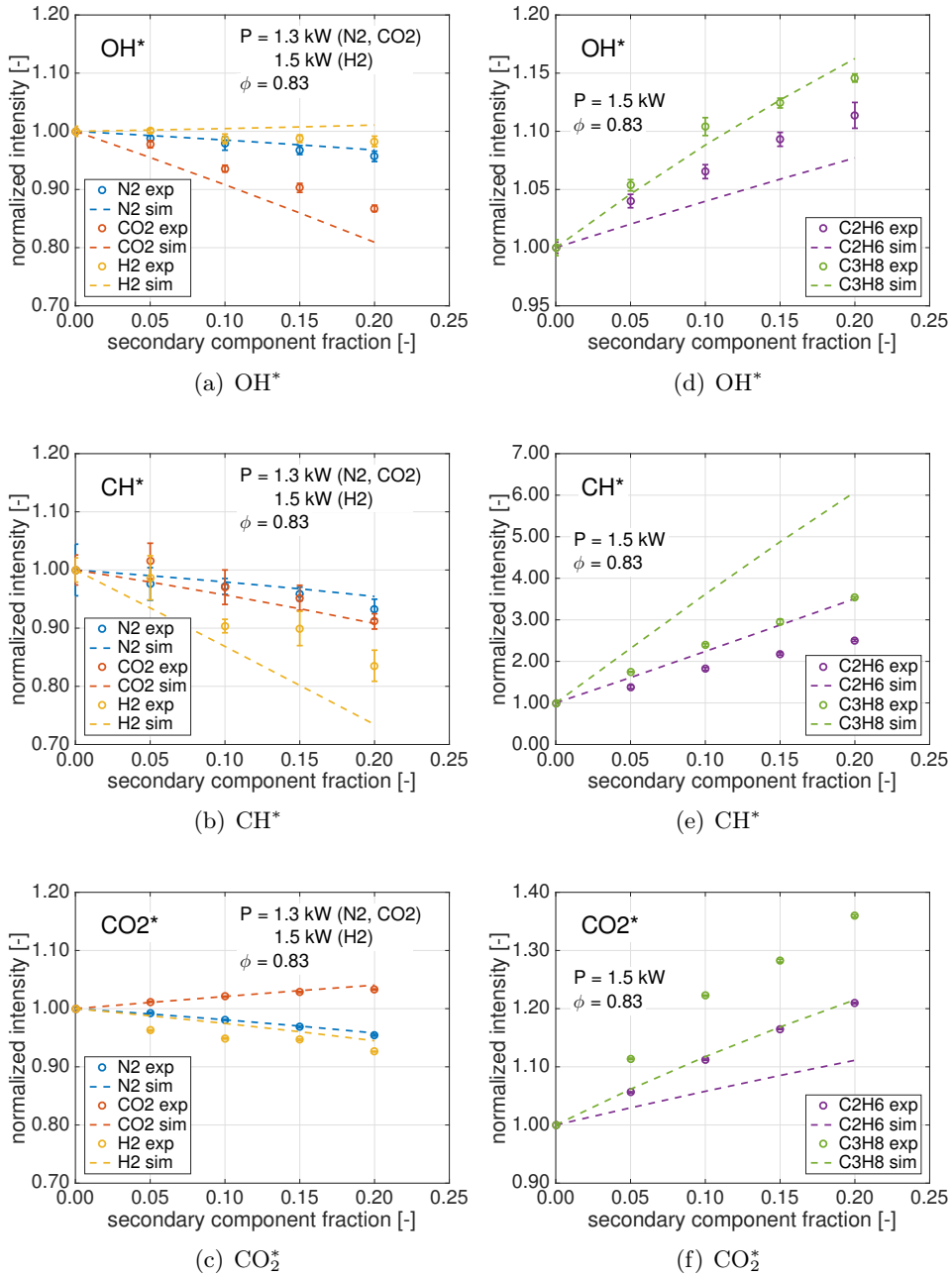

(a) OH* (d) OH*

(b) CH* (e) CH*

(c) CO_2^* (f) CO_2^*

Figure 4.1: *Evolution of the chemiluminescence intensity with the secondary component molar fraction. Experimental data are obtained with the conical flame burner. Simulations are carried out under the freely-propagating flame regime.*

numerical model, the chemical mechanisms are different for the two groups, as additional species and reactions accounting for C_2H_6 and C_3H_8 are included for the second group (see Section 3.1).

- In Fig. 4.1.a, N_2 and CO_2 dilution leads to a drop of the OH^* intensity and the change caused by CO_2 dilution is much larger than for N_2 dilution. This trend is shown by both experiments and simulations. For H_2 enrichment, the loss of OH^* originating from CH_4 is compensated by the production of OH^* radicals originating from H_2 and the global level of the OH^* intensity remains roughly unchanged.

- In Fig. 4.1.b, N_2 and CO_2 dilution also results in a drop of the CH^* intensity, but the reduction caused by CO_2 is only slightly stronger than N_2 dilution. On the other hand, H_2 enrichment causes a stronger drop of the CH^* intensity. It is partly attributable to the lower CH_4 flow rate to keep the same flame power, when H_2 is added to the fuel. However, the CH_4 volumetric flow rate is only reduced by about 7% for $X^{\text{fuel}}(H_2) = 0.20$ compared to operation without hydrogen $X^{\text{fuel}}(H_2) = 0$, but both experiments and simulations indicate a drop of the CH^* intensity larger than 15% for $X^{\text{fuel}}(H_2) = 0.20$. Other factors should have contributed as well to the drop of CH^* intensity when H_2 is injected.

- In Fig. 4.1.c, N_2 and H_2 addition cause a slight decrease while CO_2 dilution causes a slight increase of the CO_2^* intensity. These changes are well reproduced by the numerical simulations. In the case of H_2 enrichment, the decrease of the CH^* intensity seems to be roughly coherent with the decrease of the CH_4 flow rate. The increase of the CO_2^* signal with higher CO_2 concentrations indicates that CO_2 cannot be considered as an inert component with only changes of the flame temperature. Instead, this molecule has participated in the combustion reaction and modifies the CO_2^* chemiluminescence signal.

- In the right column of Fig. 4.1, the enrichment of C_2H_6 or C_3H_8 causes an increase of the OH^* and CO_2^* intensities (Fig. 4.1.d and f), and a more remarkable increase of the CH^* intensity (Fig. 4.1.e). For the same volumetric fraction, C_3H_8 has a stronger impact on the chemiluminescence intensities than C_2H_6. One explanation for the remarkable change of the CH^* signal is that C_2H_6 and C_3H_8, thanks to the longer chain of carbon, facilitate the formation of C_2H species, a precursor of CH^* (Fig. 0.5). The numerical results generally reproduce qualitatively the trends observed in the experiments and the order of magnitude of the changes. However, a gap is noticeable between the experimental and numerical results.

In the following section, a brief discussion is conducted on the underlying physical reasons leading to these observations.

Table 4.2: *Flame conditions for the investigation of the chemiluminescence intensity as a function of the burnt gas temperature.*

Fuel	T_0	ϕ	X^{fuel}
CH_4	160 - 460 K	0.83	
CH_4	298 K	0.75 - 0.92	
CH_4/N_2	298 K	0.83	$X^{\text{fuel}}(N_2) = 0$ - 0.30
CH_4/CO_2	298 K	0.83	$X^{\text{fuel}}(CO_2) = 0$ - 0.30
CH_4/H_2	298 K	0.83	$X^{\text{fuel}}(H_2) = 0$ - 0.30

4.2 Chemiluminescence intensity vs. burnt gas temperature

Changes of the flame chemiluminescence intensity with the injection of secondary natural gas components may result from several factors, but it is natural to first investigate if this could be related to changes of the flame temperature. It has been shown in the previous section that the numerical methodology allows to well reproduce the OH^*, CH^* and CO_2^* emission intensities observed in the experiments from N_2-, CO_2-diluted and H_2-enriched methane/air mixtures. It is used here to examine whether these changes could be exclusively attributed to the modifications of the flame temperature.

The analysis carried out in this section is similar to the work of Samaniego et al. (1995) but with two differences. First, the emission intensities in Fig. 4.2 are given per unit power, while Samaniego et al. (1995) presented their results per unit surface area. Second, Samaniego et al. (1995) limited their results to the CO_2^* emission at two equivalence ratios and for N_2 diluted methane/air flames, while in the present work, it is extended to include CO_2 dilution and H_2 enrichment, and three radicals OH^*, CH^* and CO_2^*.

The flame conditions for this investigation are listed in Tab. 4.2, with a set of combustible mixtures featuring different inlet gas temperatures, equivalence ratios and N_2, CO_2 and H_2 molar fractions. Injections of C_2H_6 and C_3H_8 is not considered in this analysis. One may however already conclude that in these cases the flame temperature is not major factor altering the chemiluminescence intensity in the right column in Fig. 4.1, because the flame temperature barely changes with C_2H_6 and C_3H_8 enrichment at fixed equivalence ratio.

In Fig. 4.2, the chemiluminescence intensity per unit power calculated with Eq. 4.1 is plotted as a function of the burnt gas temperature T_b.

- In Fig. 4.2.a, results for the OH^* intensity increase with the burnt gas temperature, yet the slopes for each data series are different. Therefore

the flame temperature alone is not sufficient to account for the changes of OH^* intensity.

- In Fig. 4.2.b, for the CH^* signal, N_2 and CO_2 dilution of methane-air mixtures have the same effect as a change of inlet gas temperature T_0 in a methane/air mixture. The corresponding markers collapse almost on the same curve. A slight deviation from this curve is observed when the equivalence ratio of the CH_4/air mixture is varied (magenta markers). One possible explanation is that the higher CH_4 molar fraction in richer flames promotes the formation of the C_2H species, predecessor of CH^*, thanks to more frequent C1-C1 (species with one carbon atom) molecule collisions. Another difference concerns the results obtained with H_2 enrichment, showing a completely different trend as the other cases studied. It is reminded that with 30% vol. H_2 injection in the fuel blend, the CH_4 flow rate is reduced by about 11% in order to keep the power constant, which contributes partly to the drop of CH^* intensity. Also, H_2 enrichment hinders the formation of CH^*.

- In Fig. 4.2.c, The modification of the CO_2^* intensity with the equivalence ratio and the N_2 dilution leads to the same response as a change of inlet gas temperature of a CH_4/air mixture. The deviations observed for CO_2 dilution and H_2 enrichment are attributed respectively to a higher and lower number of carbon atoms in the reactive mixture. The decrease of CO_2^* intensity with H_2 enrichment roughly corresponds to the decrease of CH_4 flow rate. The CO_2^* intensity is reduced by $\sim 9\%$ for $X^{\text{fuel}}(H_2) = 0.3$ compared to the operation without hydrogen $X^{\text{fuel}}(H_2) = 0$, while the CH_4 flow rate is reduced by $\sim 11\%$.

4.3 Equivalence ratio indicator

4.3.1 Requirements

Making a diagnostic of the flame state with the flame chemiluminescence requires an indicator for the equivalence ratio. Calibration curves of indicator *vs.* equivalence ratio, can then be constructed. Certain properties are desired for a good equivalence ratio indicator:

- Monotonic over a wide range of equivalence ratio.

- Sensitive to changes of equivalence ratio

- Ideally independent of parameters other than the equivalence ratio (*e.g.*

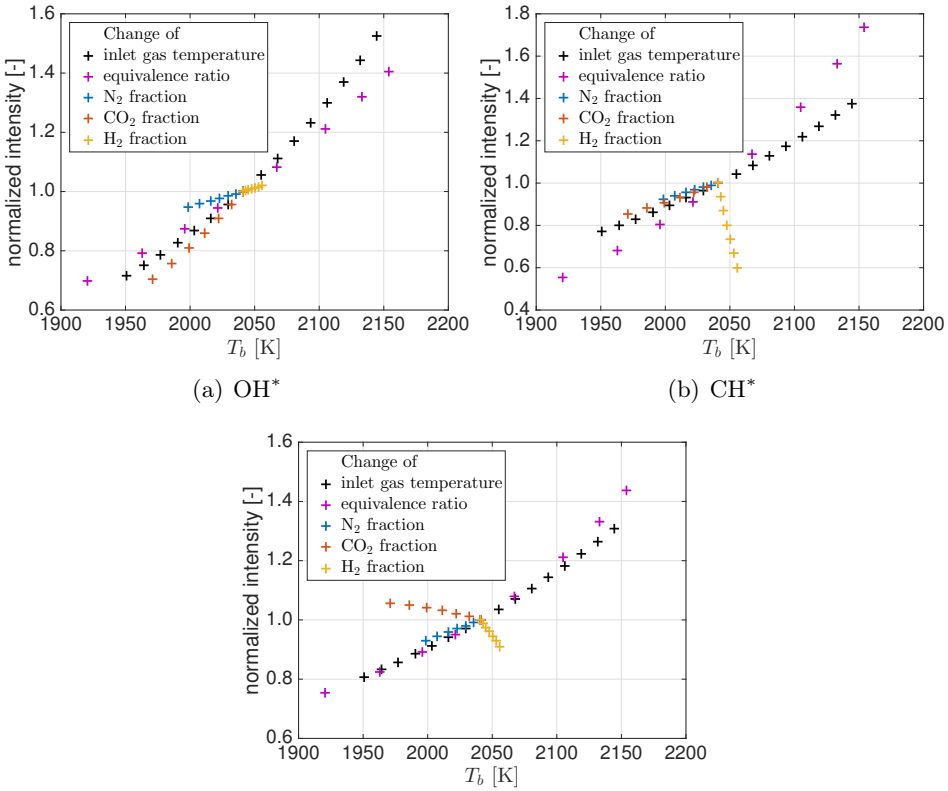

(a) OH^* (b) CH^*

(c) CO_2^*

Figure 4.2: *Numerical results for the chemiluminescence intensity per unit power as a function of the burnt gas temperature T_b for different inlet gas temperature T_0, equivalence ratio ϕ and secondary component molar fraction X^{fuel} listed in Tab. 4.2. Intensity values are normalized according to a methane-air flame at $\phi = 0.83$ and $T_0 = 298\,\text{K}$.*

power, strain rate, etc.).

- Robust with all fuel scenarios envisaged.

In practice, it is difficult to find an indicator fulfilling all these requirements and compromises need to be made. For example, when the indicator is sufficiently sensitive to equivalence ratio, small variations with disturbing factors can be tolerated. In this case, the error of the predicted equivalence ratio depends on the drift of the indicator normalized by the slope of the calibration curve. Also, when the impact of the flame power cannot be excluded, it is still possible to construct a series of calibration curves dedicated to different power levels.

When the flame chemiluminescence intensities depend on factors other than the equivalence ratio, one common technique is to take the ratio of two emission

Table 4.3: *Experimental conditions explored for the identification of equivalence ratio indicators.*

Burner	Fuel	X^{fuel}	P [kW]	ϕ
Conical flame	CH_4		1.5	0.77 - 1.00
Conical flame	CH_4/N_2	$X^{fuel}(N_2)$=0.1	1.5	0.77 - 1.00
Conical flame	CH_4/CO_2	$X^{fuel}(CO_2)$=0.1	1.5	0.77 - 1.00
Conical flame	CH_4/H_2	$X^{fuel}(H_2)$=0.2	1.5	0.77 - 1.00
Conical flame	CH_4/C_2H_6	$X^{fuel}(C_2H_6)$=0.1	1.5	0.77 - 1.00
Conical flame	CH_4/C_3H_8	$X^{fuel}(C_3H_8)$=0.05	1.5	0.77 - 1.00
Multi-perforated	CH_4		3 - 13	0.59 - 1.11
Multi-perforated	CH_4/N_2	$X^{fuel}(N_2)$=0.1	5 - 13	0.67 - 1.11
Multi-perforated	CH_4/CO_2	$X^{fuel}(CO_2)$=0.1	5 - 13	0.67 - 1.11
Multi-perforated	CH_4/H_2	$X^{fuel}(H_2)$=0.2	5 - 13	0.67 - 1.11
Multi-perforated	CH_4/C_2H_6	$X^{fuel}(C_2H_6)$=0.1	5 - 13	0.67 - 1.11
Multi-perforated	CH_4/C_3H_8	$X^{fuel}(C_3H_8)$=0.05	5 - 13	0.67 - 1.11

intensities. A widely used indicator is the CH^*/OH^* ratio (Kojima et al. 2000). As mentioned in Section 1.4.2, it helps to remove the impact of the flame power and strain rate.

In this section, the validity of the CH^*/OH^* intensity ratio is tested for different fuel scenarios and at different flame powers. Alternative indicators are discussed in a second step. Experiments are carried on the conical flame burner and the cylindrical multi-perforated burner, with the test conditions listed in Tab. 4.3. Measurements conducted for methane-air flames serve as a reference. Secondary components are then added to the fuel in order to see whether they cause drifts of the calibration curve. Their volumetric fractions, as listed in the third column in Tab. 4.3, are chosen to represent the maximum value expected in future natural gas blends (also considering the injection of biogas and hydrogen).

Experiments with the conical flame burner are limited to a fixed power of 1.5 kW and a relatively narrow range of equivalence ratio within $\phi = 0.77 - 1.00$, in order to keep the flame stabilized on the burner rim. The power and equivalence ratio range are extended to $P = 3 - 13$ kW and $\phi = 0.67 - 1.11$ for the multi-perforated burner, thanks to its large stable operating range. The quartz tube set around the burner keeps the secondary flame outside the spectrometer field of view and allows for studies of fuel rich regimes when $\phi > 1$.

4.3.2 Validity of CH^*/OH^* as equivalence ratio indicator

Results for the CH^*/OH^* intensity ratio are plotted as a function of the equivalence ratio in Fig. 4.3 for data gathered with the conical flame burner. The

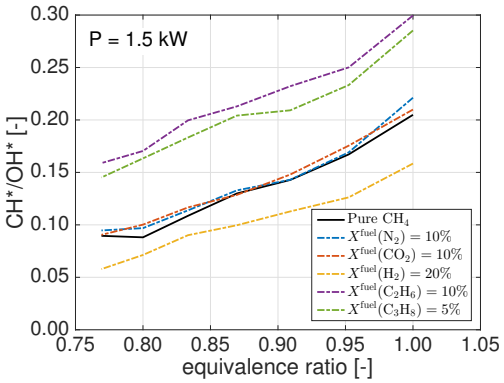

Figure 4.3: *CH*/OH* vs. equivalence ratio for the different fuel composition scenarios listed in Tab. 4.3 and flames stabilized above the conical flame burner.*

calibration curve obtained with pure methane (black solid line) remains valid for moderate N_2 or CO_2 dilutions. This is consistent with the observations made in Figs. 4.2.a and 4.2.b, in which the changes observed for the OH* and CH* intensities caused by the dilution are quantitatively close. The injection of H_2 yields a noticeable error of the predicted equivalence ratio ($\Delta\phi \sim 0.05$ for $X^{\text{fuel}}(H_2) = 20\%$). It is caused by the different response of the CH* and OH* emissions to H_2 enrichment. The CH* intensity is considerably reduced while the OH* value remains roughly unchanged due to the compensation of OH* supplied by the H_2 reactions. For C_2H_6 and C_3H_8, however, even a modest molar fraction of a few percent in the fuel mixture causes considerable errors ($\Delta\phi > 0.1$), which may not be acceptable for the aimed application of combustion control. The gaps for the curves of H_2, C_2H_6 and C_3H_8 with regard to pure CH_4 result from the different effects of these components on CH* and OH* intensities revealed in Figs. 4.2.d and 4.2.e.

Results are then presented for the cylindrical multi-perforated burner used in real domestic gas boilers. The calibration curves obtained for pure methane for $P = 3$ to 13 kW are plotted in Fig. 4.4. These curves remain close for $\phi < 0.8$. Yet a clear separation is seen for $\phi > 0.8$, meaning that the impact of the flame power is not completely removed by taking the ratio of the CH* and OH* intensities for flames stabilized on this particular burner. Nevertheless, the deviation tends to be smaller at high power. It is seen that the curves for $P = 11$ kW and 13 kW remain the same over the whole range of equivalence ratio explored. For application to a real gas boiler, this separation of curves would cause errors of the predicted equivalence ratio for $\phi > 0.8$ if one single calibration curve is used for all levels of power. However, when the targeted equivalence ratio is below $\phi = 0.8$, errors at higher equivalence ratios can be tolerated. As the curves remain monotonic over the range of equivalence ratio investigated, the control system is still able to correct drifts of the operating

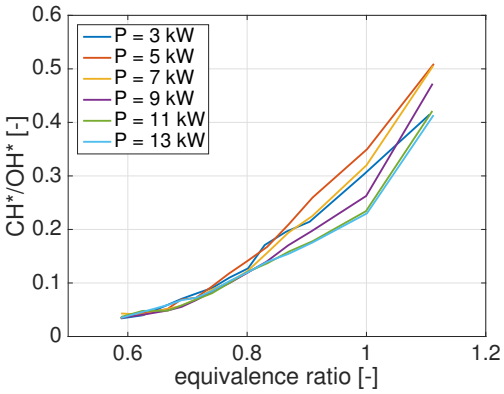

Figure 4.4: *CH^*/OH^* vs. equivalence ratio for methane-air flames stabilized on the cylindrical multi-perforated burner operated a different thermal powers.*

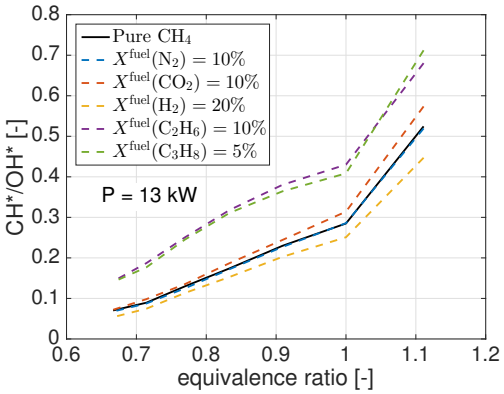

Figure 4.5: *CH^*/OH^* vs. equivalence ratio for different fuel blend compositions listed in Tab. 4.3 and flames stabilized on the cylindrical multi-perforated burner.*

point to richer conditions and bring it back to the set point, despite the errors of the predicted equivalence ratio value.

The separation of curves for $\phi > 0.8$ in Fig. 4.4 is believed to result from the heat exchange between the flame and the burner, when it works under the radiation mode. A detailed study of this phenomenon is carried out in Chapter 5.

The calibration curves for different fuel blend compositions are shown in Fig. 4.5 for flames stabilized on the cylindrical multi-perforated burner. The conclusions are similar to Fig. 4.3 obtained for flames stabilized with the conical flame burner. One slight difference is that the shift due to H_2 enrichment is smaller for the flames stabilized on the cylindrical multi-perforated burner. This might also be related with the flame-burner heat exchange phenomenon discussed in Chapter 5.

In summary, CH^*/OH^* calibration curves as a function of equivalence ratio obtained from methane-air flames remain valid when the fuel is diluted with N_2 and CO_2. Small deviations are found for H_2 enriched fuel blends. When C_2H_6 or C_3H_8 is added to the fuel, a big gap is seen with respect to the pure methane curve, and the resulting errors are generally unacceptable for equivalence ratio monitoring purpose. In addition, for the cylindrical multi-perforated burner, the CH^*/OH^* intensity ratio is slightly sensitive to the flame power for mixtures with $\phi > 0.8$. This commonly used indicator failing to fulfill all the requirements, alternative indicators need to be identified.

4.3.3 Alternative equivalence ratio indicators

4.3.3.1 CO_2^*/OH^*

In the first place, it is still favorable to use the ratio of two emission intensities as equivalence ratio indicator, considering the possibility to at least partially remove the impact of the flame power. Since the problem with the CH^*/OH^* indicator mainly results from the large increase of the CH^* intensity with C_2H_6 and C_3H_8 enrichment, it is advisable to take the two other major emissions of CO_2^* and OH^*.

The CO_2^*/OH^* intensity ratio is plotted as a function of the equivalence ratio in Fig. 4.6 for the data gathered with the conical flame burner. The CO_2^* intensity is measured with the photomultiplier tube equipped with a bandpass optical filter centered at 450 nm, while the OH^* is determined with the spectrometer. Although the CO_2^*/OH^* works perfectly with C_2H_6 and C_3H_8 enriched fuel blends, the deviation from the pure methane calibration curve with CO_2 and H_2 enrichment is in this case quite large. Another weakness of this indicator is that the resulting curves are relatively flat, making this indicator more vulnerable to various measurement uncertainties.

In addition, the CO_2^*/OH^* intensity ratio cannot be used with the cylindrical multi-perforated burner when the CO_2^* intensity is estimated by its emission near 450 nm. In Fig. 4.7, it is seen that at 5 kW the contribution from the thermal radiation of the burner already becomes comparable to the chemiluminescence signal, and the measured CO_2^* intensity would be mistakingly increased by about 20%. Considering the flat slope of the curves shown in Fig. 4.6, the resulting errors on the equivalence ratio are significant. When the CO_2^* intensity is taken near 370 nm, deviations of the calibration curve with respect the reference of pure methane are much larger than in Fig. 4.6. The CO_2^*/OH^* intensity ratio is therefore not a good indicator either.

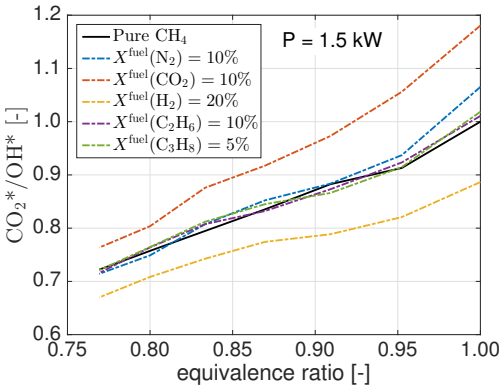

Figure 4.6: *CO_2^*/OH^* vs. equivalence ratio for the different fuel blend compositions listed in Tab. 4.3 and flames stabilized above the conical flame burner.*

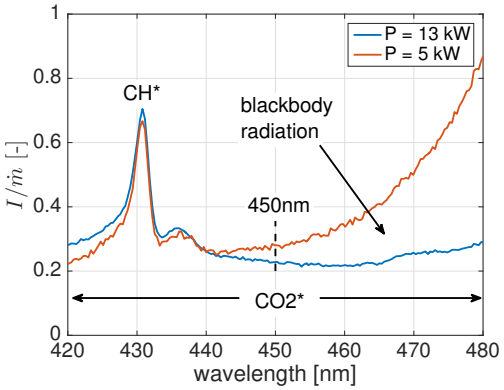

Figure 4.7: *Invasion of thermal radiative emission near* 450 nm *with the cylindrical multi-perforated burner.*

4.3.3.2 C_2^*/CH^*

Another potential indicator is the C_2^*/CH^* ratio. The corresponding calibration curves plotted in Fig. 4.8.b show that the error made on the predicted equivalence ratio is reduced to $|\Delta\phi| < 0.03$ for the experiments conducted with the cylindrical multi-perforated burner over $\phi = 0.83 - 1.11$. The deviation is a bit larger for the results shown for the conical flame burner in Fig. 4.8.a seemingly due to a weak signal-to-noise ratio. Figure 4.9.a also shows that taking the intensity ratio helps to remove effects of the power at least over the range of $P = 9 - 13\,\mathrm{kW}$.

However, the C_2^* intensity suffers from two major weaknesses when used to deduce the equivalence ratio in a domestic gas boiler. First, C_2^* emission remains weak for methane-air flames and is almost invisible at lean conditions of $\phi \lesssim 0.8$. The range of validity of C_2^*/CH^* to recover safely the equivalence ratio

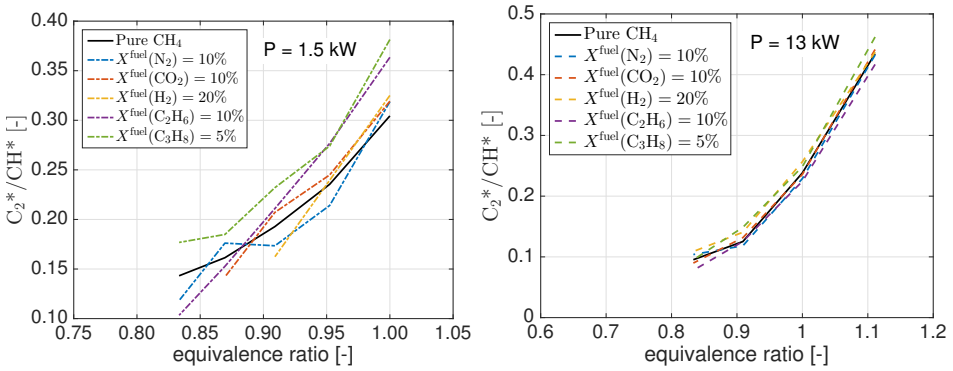

(a) Conical flame burner (b) Multi-perforated burner

Figure 4.8: *C_2^*/CH^* vs. equivalence ratio for different fuel composition scenarios.*

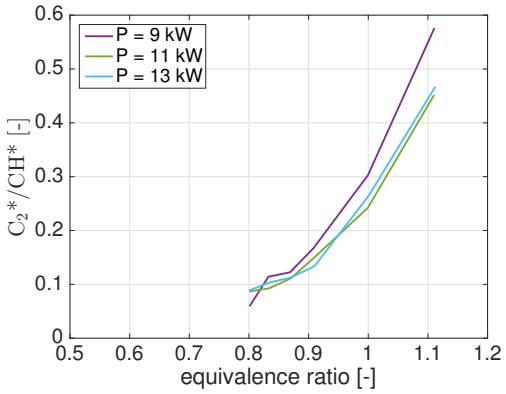

Figure 4.9: *C_2^*/CH^* vs. equivalence ratio for methane-air flames stabilized on the cylindrical multi-perforated burner at different thermal powers.*

in Fig. 4.8 is insufficient for domestic gas boilers operating around $\phi = 0.8$. Nevertheless, the C_2^*/CH^* intensity ratio may have the potential to be applied to other apparatus operating near the stoichiometry, or used in combination with another indicator accounting for leaner conditions. The second problem is that the C_2^* peak emission at 516 nm is hidden by the thermal emission spectrum from the burner hot surface when operating in radiation mode (see Fig. 0.4). Its intensity is therefore difficult to be correctly isolated. In Fig. 4.9, the curve for $P = 9\,\text{kW}$ starts to deviate from the two other curves for $P = 11$ and $13\,\text{kW}$ because of the stronger thermal radiation at low power. For $P < 9\,\text{kW}$, the signal-to-noise ratio is too high to build the ratio C_2^*/CH^* in Fig. 4.9 with the current method due to a weaker chemiluminescence intensity and a stronger thermal radiation.

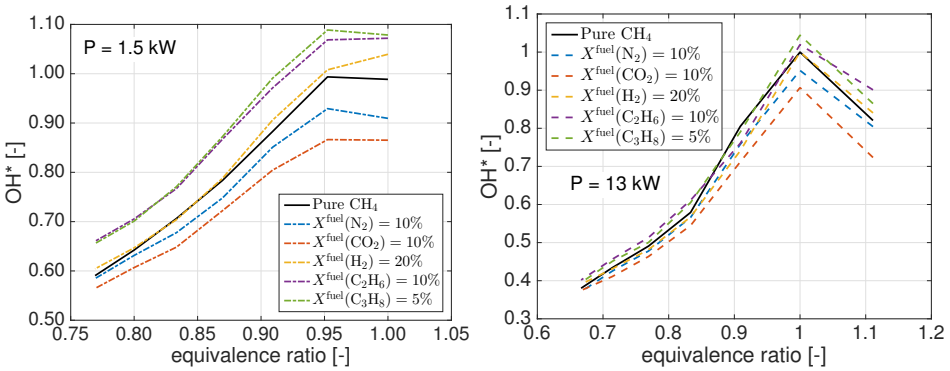

(a) Conical flame burner (b) Multi-perforated burner

Figure 4.10: *OH* normalized intensity vs. equivalence ratio for different fuel blends and the two burners tested.*

4.3.3.3 OH* alone

A simpler alternative is to use the OH* signal only emitted in the UV. In Fig. 4.1, it is observed that the OH* intensity is less altered by the injection of secondary components in the fuel blend. Relative changes are limited to ±15% for molar fractions up to $X^{\text{fuel}} = 0.2$. This observation is valid for any of the five components investigated. This property makes it a potential candidate as an alternative indicator.

The evolution of the OH* intensity for the different fuel blends tested is plotted in Fig. 4.10. Results are shown as a function of equivalence ratio for experiments made with the conical flame burner and the cylindrical multi-perforated burner. The differences between the results with secondary components in the combustible mixture with respect to the signal recorded for a pure methane/air mixture are reduced to less than $|\Delta\phi| < 0.03$ for both burners. This is acceptable for the operation point monitoring purpose.

It is worth recalling that the results plotted in Fig. 4.1 are obtained at a fixed thermal power. It is obvious that by only recording the OH* chemiluminescence intensity, the impact of the thermal power cannot be removed. This means that a series of calibration curves, each dedicated to a different power level, needs to be constructed. Another drawback for industrial application is that the signal attenuation due to the contamination of the optical acquisition system cannot be corrected by itself and may lead to a shift of the predicted equivalence ratio.

Table 4.4: *Summary of advantages and drawbacks of potential equivalence ratio indicators.*

	Advantages	Drawbacks
CH^*/OH^*	• Valid with injection of N_2, CO_2 and H_2. (multi-perforated burner). • Partially independent of power ($\phi < 0.8$).	• large error with C_2H_6, C_3H_8 and other heavier hydrocarbon enrichment.
CO_2^*/OH^*	• Valid with N_2, C_2H_6, C_3H_8.	• Large error with CO_2 and H_2. • Impact of thermal radiation spectrum near 450 nm.
C_2^*/CH^*	• Valid with the 5 secondary components studied (N_2, CO_2, H_2, C_2H_6, C_3H_8).	• C_2^* signal is weak for CH_4-air flames and undetectable below $\phi = 0.8$. • Impact of the thermal radiation spectrum near 516 nm.
OH^*	• Valid with the 5 secondary components studied (N_2, CO_2, H_2, C_2H_6, C_3H_8).	• Dependence on flame power.

4.3.3.4 Choice of equivalence ratio indicator

Based on the above discussions, the advantages and drawbacks of potential equivalence ratio indicators CH^*/OH^*, CO_2^*/OH^*, C_2^*/CH^* and OH^* are summarized in Tab. 4.4. Considering the targeted application in real domestic gas boilers, using the signal of OH^* alone appears as a reasonable compromise.

Conslusion

Addition of a secondary component N_2, CO_2, H_2, C_2H_6 and C_3H_8 to a pure methane/air mixture leads to changes of the chemiluminescence signal, which have been thoroughly characterized in this chapter.

The most remarkable effect is the significant increase of the CH^* intensity with even a small fraction of C_2H_6 or C_3H_8 in the combustible mixture. This sensitivity results in a considerable error for the predicted equivalence ratio when the CH^*/OH^* ratio is used as an indicator. The CO_2^*/OH^* intensity ratio appears to be unadapted to operation with the multi-perforated burner at low power due to the strong thermal radiation of the burner. The C_2^*/CH^*

intensity ratio features the same drawback and is also inadequate to operation at lean conditions due to the weak C_2^* emission.

The OH^* intensity alone is proposed as an alternate candidate to determine the mixture equivalence ratio with an acceptable compromise between (1) a weak sensitivity to all secondary components injected, (2) a good dynamical range for lean and stoichiometric mixtures and (3) a fairly good precision for equivalence ratio sensing. The tests made under quasi-adiabatic conditions with the conical flame burner and with flames stabilized by heat losses with the multi-perforated burner show that the equivalence ratio is predicted with $|\Delta\phi| < 0.03$ for all fuel blends tested with the five secondary components up to a molar fraction of $X^{\text{fuel}} = 0.2$. The main drawback of this indicator is that the thermal power needs to be known.

Chapter 5

Effects of flame-burner heat exchange

This chapter focuses on the chemiluminescence signal from flames with significant heat loss to the burner. This is an important feature of the burner used in domestic gas boilers with a large turn-down ratio. Experiments and simulations are carried out to characterize the evolution of chemiluminescence intensity with the inlet gas velocity and temperature. A correlation between the chemiluminescence intensity with the burnt gas temperature is revealed by the simulation.

5.1 Flame-burner heat exchange

One particular feature of the cylindrical multi-perforated burner is its wide power modulation range needed to meet the varying heating power demand, as described in Section 2.1.1.

For premixed flames, the upper power limit is generally set by flame blow-off at high gas flow rate and the lower limit is imposed by the laminar burning velocity to avoid flash back. The lower power limit may be extended by reducing the size of the injection holes below the quenching distance (Lee et al. 2011a). In this way laminar premixed flames can be stabilized above the burner even when the gas velocity drops below the adiabatic laminar burning velocity S_L. The flames are in this case stabilized very close to the burner surface with a large heat transfer towards the burner. The flame-burner distance is lower than the flame thermal thickness and the burner outlet surface lies within the flame preheating zone (de Goey et al. 2011). The heat loss lowers the flame temperature and hence the actual flame propagating speed, which then differs

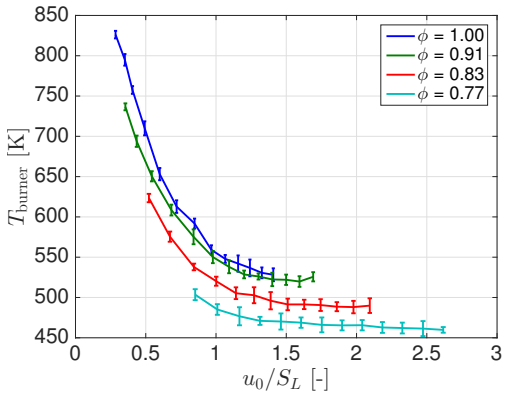

Figure 5.1: *Porous plug burner temperature as a function of u_0/S_L. u_0 : gas flow velocity at the burner outlet. S_L : adiabatic laminar burning velocity at the gas outlet temperature T_0.*

from the adiabatic laminar burning velocity S_L. The flame finally achieves an equilibrium with the gas velocity u_0. Asymptotic analysis can be used as a guide to determine the stability boundaries of these flame regimes (Joulin and Clavin 1979).

This heat transfer can be highlighted by measuring the burner surface temperature. This temperature is plotted for the porous plug burner in Fig. 5.1 as a function of u_0/S_L, where u_0 is the bulk velocity at the burner outlet and S_L denotes the adiabatic laminar burning velocity. These measurements are made with a Fluke 572 IR thermometer as explained in Section 2.6.1. The emissivity of bronze is set to be $\epsilon = 0.55$ and the sampling region is a circular zone of about 20 mm diameter.

The burner surface temperature monotonically increases in Fig. 5.1 for decreasing flow rates over the investigated range of u_0/S_L. The trend qualitatively indicates a larger absolute heat flux transferred from the flame to the burner as the flow rate is reduced. Obviously, the heat loss fraction ξ_{loss}, *i.e.*, the ratio of absolute heat loss to the flame power, also increases when the flow rate is reduced. It is worth pointing out that, when u_0/S_L continues to decrease beyond the investigated range, the trend for heat loss fraction ξ_{loss} is supposed to be unchanged, while the absolute heat loss, hence the burner temperature, is expected to reach a maximum and then drops as the absolute flame power lowers. The heat transfer is strong when $u_0/S_L < 1$ and is less intense high flow rates, but does not vanish at least within the investigated range of conditions explored.

A quantitative investigation of the heat flux is difficult with the current experimental setup. However, this kind of measurement has been done for example by Botha and Spalding (1954) with a water-cooled burner, and more recently

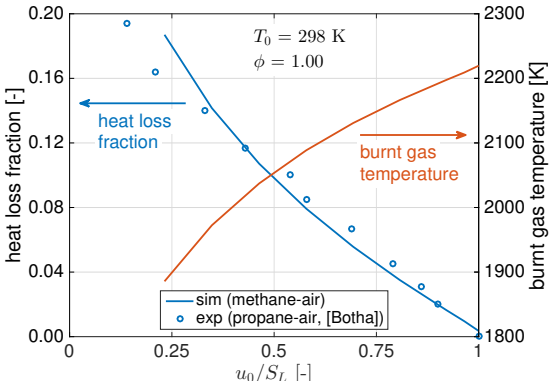

Figure 5.2: *Evolution of the heat loss fraction ξ_{loss} and burnt gas temperature T_b with the normalized flow rate u_0/S_L. The solid lines correspond to simulation results. Circles are experimental results taken from Botha and Spalding (1954).*

by Van Maaren et al. (1994) by measuring the temperature gradient along their porous plug burner.

The experimental results from Botha and Spalding (1954) obtained for propane/air mixtures are compared in Fig. 5.2 with the simulation results obtained with the REGATH flow solver for methane/air mixtures. This figure shows the evolution of the heat loss fraction ξ_{loss} and the burnt gas temperature T_b as a function of u_0/S_L. The fraction ξ_{loss} of heat which is lost with respect to the thermal power is calculated as:

$$\xi_{\text{loss}} = \frac{\lambda \frac{dT}{dx}\Big|_{x=0}}{f_0 Y_{\text{CH}_4} \Delta h^0_{\text{CH}_4}} \tag{5.1}$$

where $\Delta h^0_{\text{CH}_4}$ is the reaction enthalpy per unit mass and Y_{CH_4} the mass fraction of methane. f_0 denotes the mass burning flux.

When u_0/S_L decreases, the heat losses increase and the burnt gas temperature drops in Fig. 5.2. The simulated behavior of the burner reproduces well the experimental results from Botha and Spalding (1954) obtained for stoichiometric propane-air flames stabilized over a porous plug burner. This behavior is also consistent with the conclusions drawn from Fig. 5.1 except that ξ_{loss} goes to zero at $u_0/S_L = 1$ in Fig. 5.2, while the temperature measurements shown in Fig. 5.1 indicate that the heat exchange still persists for $u_0/S_L > 1$ though it is reduced. It is suggested that the difference results from a small fraction of the flame with u_0/S_L locally below unity in the experiments.

On the other hand, the hot burner may transfer part of the energy back to the flow by preheating the reactant stream passing through. In Fig. 5.3, the reactant stream temperature for the porous plug burner and the multi-perforated

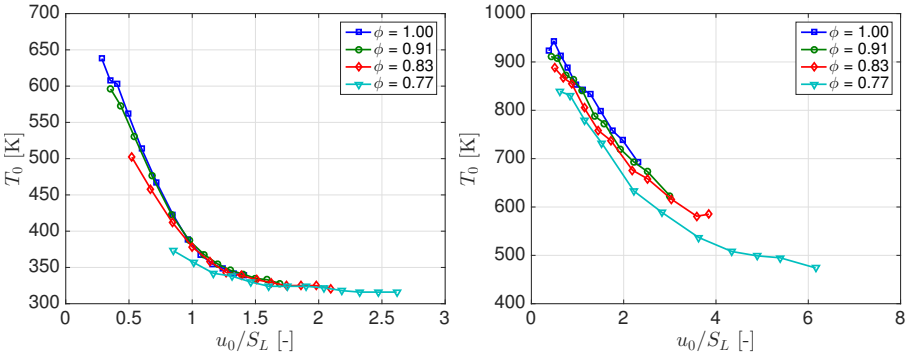

(a) Porous plug burner (b) Multi-perforated burner

Figure 5.3: *Reactant stream temperature T_0 as a function of u_0/S_L. u_0 : gas flow velocity at the burner outlet. S_L : adiabatic laminar burning velocity at T_0.*

burner is measured with the method explained in Fig. 2.6.2. A clear rise of temperature is noticed at low u_0/S_L values. However, the heat retrieved through preheating is always lower than the loss from the flame, as part of the heat is dissipated by the burner through thermal radiation, and also conduction through the metallic burner components. In a boiler, the heat dissipated is mostly retrieved by the heat exchanger downstream. This global enthalpy loss from the burner makes it different from superadiabatic burners described for example by Barra and Ellzey (2004).

5.2 Non-adiabatic flame chemiluminescence

The chemiluminescence intensity is known to be altered by several factors (Section 1.3). In the present work, the flames stabilized on the three burners studied are laminar and effects of flame curvature are limited (Law and Sung 2000). Moreover, there is no large gradient in the velocity field of the fresh stream of reactants, and effects of strain rate can be ignored. Flames also remain steady in a laminar regime for all the operating conditions investigated. The remaining factors controlling the chemiluminescence signal are the equivalence ratio ϕ, mixture mass flow rate $\dot{m}$ and gaseous stream temperature T_0 at the burner outlet. Effects of the equivalence ratio on the chemiluminescence emission are well known.

The main objective of this study is to understand effects of the mixture flow rate (or flame power) and reactant stream temperature on the chemiluminescence signal from methane/air flames. It will be shown that the observed features can be closely related to the burner-flame heat exchange in the investigated

configurations.

For the purpose of a fundamental parametric study, the porous plug burner featuring at low flow rates large heat losses to the burner is a better model as compared to the multi-perforated burner, thanks to its simpler geometry. This burner is also well suited for the 1-D numerical flow simulations of non-adiabatic flames described in Section 3.2.2. In addition, experiments are also conducted on the conical flame burner, which serves as a reference.

The experimental conditions explored in this chapter are synthesized in Tab. 5.1.

The evolution of chemiluminescence intensity with the fuel-air mixture flow rate at fixed equivalence ratios is first investigated in Section 5.3 for the three burners (*i.e.* conical flame burner, porous plug burner and cylindrical multi-perforated burner). For the two latter burner configurations, the bulk gas temperature T_0 at the injector outlet could not be kept constant when the mixture mass flow rate $\dot{m}$ is varied, due to the preheating by the hot burner. The impact of this temperature increase is ignored at first in the analysis carried out. This approximation is however discussed *a posteriori* in Section 5.4.2.

In Section 5.4, effects of the reactant stream preheating are analyzed with experiments carried out on the porous plug burner with the help of an electrical heating tube (see Fig. 2.3.b and Fig. 5.4). The study is not repeated for the conical flame burner and the multi-perforated burner since their large heat inertia makes it difficult to heat up the reactant stream to reach a sufficiently high temperature.

In addition, numerical simulations are conducted to investigate the impact of the flow rate and gas temperature. Numerical results are compared to the experimental data for the porous plug burner.

Table 5.1: *Experimental conditions. The temperature T_u denotes the gas temperature at the outlet of the electrical heating tube before the porous plug burner.*

Burner	ϕ	P [kW]	T_u	Section
conical flame	0.77 - 1.00	1.0 - 2.0	20 °C	§ 5.3
porous plug	0.77 - 1.00	0.6 - 1.8	20 °C	§ 5.3
multi-perforated	0.77 - 1.00	3.0 - 13.0	20 °C	§ 5.3
porous plug	1.00	0.6 - 1.8	20 - 180 °C	§ 5.4

To ease the interpretation of the experimental and numerical results, the following quantities are clarified:

- T_u corresponds to the unburnt gas temperature before entering the burn-

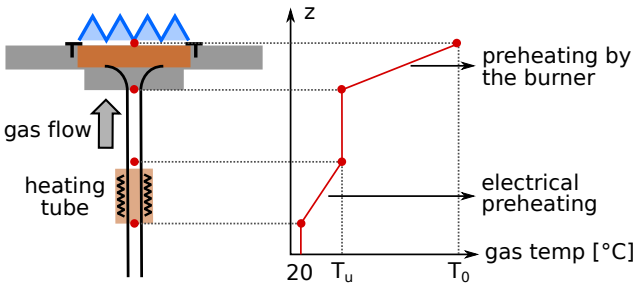

Figure 5.4: *Evolution of the reactant gas temperature in the porous plug burner setup.*

ers (see Fig. 5.4). The reactant stream is supplied at room temperature ($T_u = 20\,°C$) except in Section 5.4 where electrical heating is used.

- T_0 denotes the burner outlet gas temperature (see Fig. 5.4), which also corresponds to the temperature at the numerical domain inlet for the flow simulations. For the porous plug burner and the multi-perforated burner, the reactant stream is preheated by the hot metallic parts and the temperature T_0 is higher than T_u. The technique used to determine T_0 is described in Section 2.6.2 and the results are presented in Fig. 5.3. For the conical flame burner, preheating remains weak and changes of T_0 can be ignored.

- u_0 is the bulk velocity of the reactant stream at the burner outlet. This velocity is calculated by dividing the volumetric flow rate of the reactant stream at the temperature T_0 by the area of all injection holes for the conical flame burner and the multi-perforated burner. For the porous plug burner, the volumetric flow rate is divided by the porous plate area.

- u_0/S_L corresponds to the normalized inlet gas velocity. In this expression S_L is the adiabatic laminar burning velocity at the temperature T_0. For a given mass flow rate, u_0/S_L is a function of T_0 because S_L increases with T_0 faster than u_0 for methane-air mixtures (Lewis and Von Elbe 1987; Konnov 2015). The regime $u_0/S_L < 1$ corresponds to flames stabilized by heat loss.

- I_s is the specific chemiluminescence emission intensity:

$$I_s = I/\dot{m} \tag{5.2}$$

  where $\dot{m}$ is the mass flow rate of the reactant stream. The superscripts "exp" and "sim" are used to denote experimental and numerical results.

- $f_0 = \rho u$ corresponds to the mass burning flux, where ρ is the gas density and u the gas velocity.

5.3 Specific intensity vs. mass flow rate

For adiabatic premixed systems, the chemiluminescence intensity of a given species is found to be proportional to the mixture flow rate (Hurle et al. 1968; Higgins et al. 2001; Higgins et al. 2001) when the equivalence ratio is kept constant. In this case, the specific intensity given by Eq. 5.2 should remain constant. This linearity relationship is examined in this section for the three burner configurations.

5.3.1 Conical flame burner

Results are first analyzed for the conical flames stabilized with the setup shown in Fig. 2.2. A series of spectra are recorded for powers ranging within $P = 1.0 - 2.0\,\mathrm{kW}$ and equivalence ratios $\phi = 0.77 - 1.00$.

Figure 5.5 shows for different equivalence ratios the evolution of the specific intensity I_s^{exp} with u_0/S_L and indicates that these two quantities are independent. This confirms that the OH^*, CH^* and CO_2^* chemiluminescence intensities linearly increase with the mixture flow rate under adiabatic operating conditions.

A brief analysis is made to evaluate the impact of flame stretch on the chemiluminescence signal. The stretch rate for the investigated conical flames hardly exceeds $100\,\mathrm{s}^{-1}$ except over a very small fraction of the flame surface at the apex of the conical flame (Law and Sung 2000). Changes of the chemiluminescence intensity are then estimated to be lower than 5% according to the results from Panoutsos et al. (2009). In addition, it can be deduced that for conical flames the stretch rate barely varies with the gas velocity u_0 for a given laminar burning velocity S_L (or equivalence ratio ϕ). According to Law and Sung (2000), the stretch rate for a conical flame can be estimated as

$$\kappa = -\frac{u_0 \sin 2\alpha}{2r} \tag{5.3}$$

where α is the half apex angle of the cone, r the distance of the flame from the axis. By assuming a small half apex angle α, the formula can be simplified as:

$$\kappa \sim S_L/r \tag{5.4}$$

It is then not a function of u_0. Therefore the stretch rate can be considered to remain roughly constant for each curve in Fig. 5.5 and does not modify the shape of the curves.

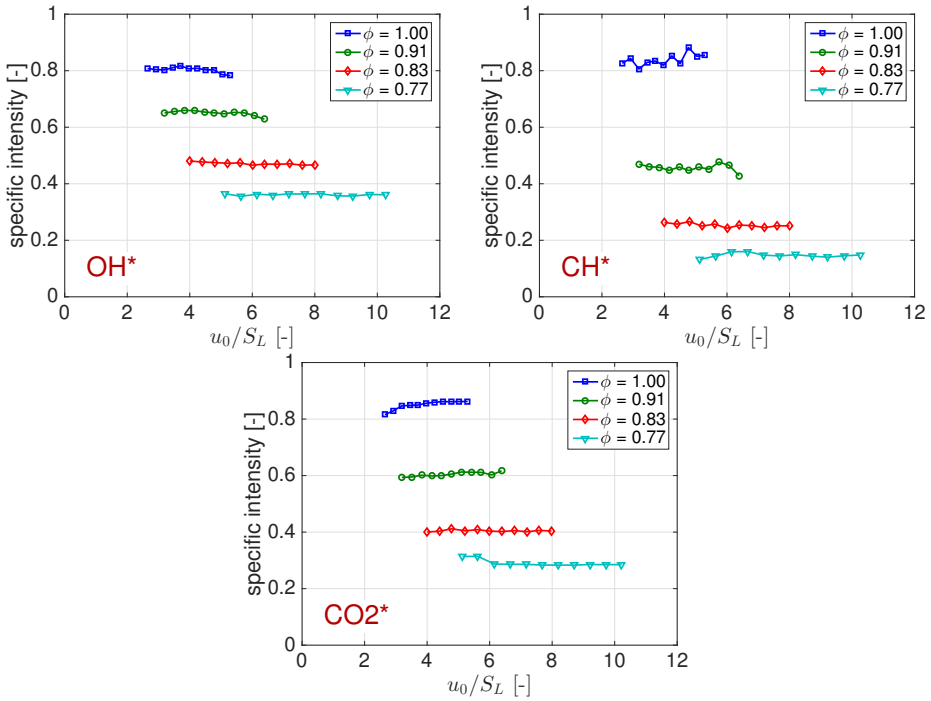

Figure 5.5: *Specific emission intensities I_s^{exp} of OH^*, CH^* and CO_2^* for measurements conducted with the conical flame burner operating in nearly non-adiabatic mode.*

5.3.2 Porous plug burner

5.3.2.1 Experimental results

The same measurements are repeated with the porous plug burner shown in Fig. 2.3 operating at powers $P = 0.6 - 1.8\,\text{kW}$ and equivalence ratios $\phi = 0.77 - 1.00$. Results are presented in Fig. 5.6. It is noticed here that the behavior of I_s^{exp} may be split into two regimes. The specific intensity remains constant for $u_0/S_L > 1$ and then changes with the mass flow rate injected when u_0/S_L drops below unity.

The left part of the curves plotted in Fig. 5.6 therefore indicates that the proportional relationship between the chemiluminescence intensity and the mixture mass flow rate $\dot{m}$ is violated in this regime. It is hypothesized that this phenomenon is due to the heat transfer between the flame and the burner. Heat losses reduce the flame temperature, hence the specific intensity I_s^{exp} is lower than the value expected for an adiabatic freely-propagating flame.

When $u_0/S_L > 1$, conical flames are formed above the porous burner (see Fig. 2.4.a). The combustion reaction mainly takes place at a distance of a

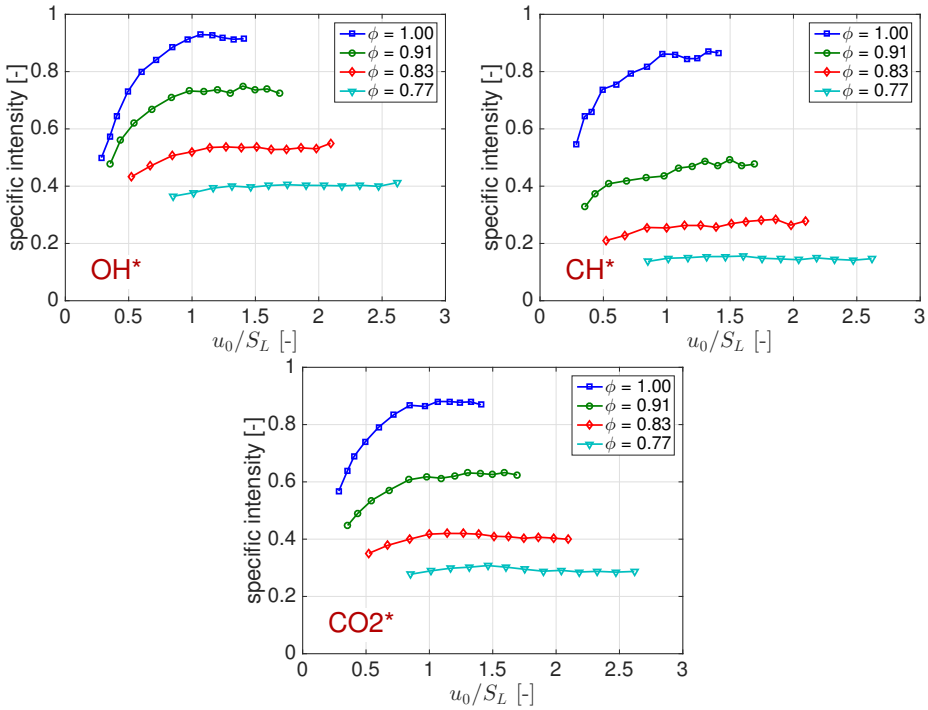

Figure 5.6: *Specific emission intensities I_s^{exp} of OH^*, CH^* and CO_2^* for measurements conducted with the porous plug burner.*

few millimeters away from the porous surface. This distance being larger than the flame thermal thickness (1 mm), heat losses to the burner are drastically reduced.

These results obtained with the porous plug burner complete those found for the conical flame burner shown in Fig. 5.5. The range of conditions explored in Fig. 5.5 corresponds to $u_0/S_L > 1$, over which I_s^{exp} remains constant. Flames cannot be stabilized above this conical flame burner when $u_0/S_L < 1$ due to flashback.

5.3.2.2 Numerical results

The behavior of OH^* and CH^* emissions in the $u_0/S_L \leq 1$ regime is also investigated with the numerical model adapted to burner-stabilized flames. The reactants are injected in the numerical domain at the same velocity u_0 and temperature T_0 as in the experiments (Fig. 5.3.a). The specific intensity of the k^{th} species is obtained by dividing the emission intensity per unit surface area

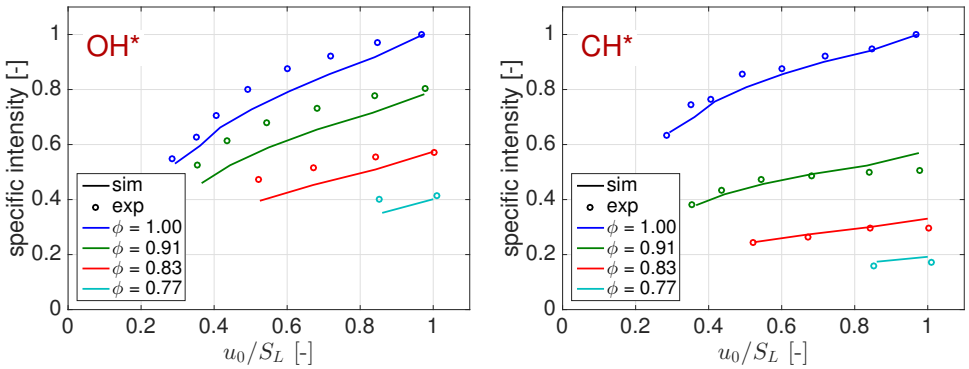

Figure 5.7: *Evolution of OH* and CH* specific intensities for the porous plug burner with the normalized gas velocity u_0/S_L at different equivalence ratios. Lines : simulations. Circles : measurements.*

in Eq. 3.21 by the mass burning flux f_0:

$$I_{s,k}^{\text{sim}} = \frac{\int_0^L I_k dx}{f_0} \tag{5.5}$$

Numerical results together with the experimental data for the porous plug burner are shown in Fig. 5.7. To ease comparisons, the scales for the specific intensities I_s^{exp} and I_s^{sim} are adapted so that the values for $u_0/S_L = 1.0$ and $\phi = 1.0$ are set equal to unity.

These simulations support the experimental observations that the specific intensity is not constant in the regime $u_0/S_L < 1$. For CH* intensity (Fig. 5.7.b), the simulations (solid lines) match well the experiments (circles). The small difference for $\phi = 0.91$ (dark green) near $u_0/S_L = 1$ can be attributed to a slight drift of the transition point from the linear to the nonlinear regime that can be seen in Fig. 5.6.b. This drift causes I_s^{exp} to be slightly underestimated at $u_0/S_L = 1$. For OH* (Fig. 5.7.a), the specific intensity values at $u_0/S_L = 1$ is correctly predicted. For $u_0/S_L < 1$, the slope of the curves are relatively well reproduced, but the experimental data lie slightly above the simulation curves.

5.3.3 Cylindrical multi-perforated burner

The same experiments are finally repeated with the cylindrical multi-perforated burner for powers $P = 5 - 13\,\text{kW}$ and equivalence ratios $\phi = 0.77 - 1.00$. The velocity profile of the gaseous mixture leaving this burner is not uniform over the burner surface due to its complex internal multi-layer structure. In addition, the gas jet velocity exiting the burner slits and the small circular holes rapidly

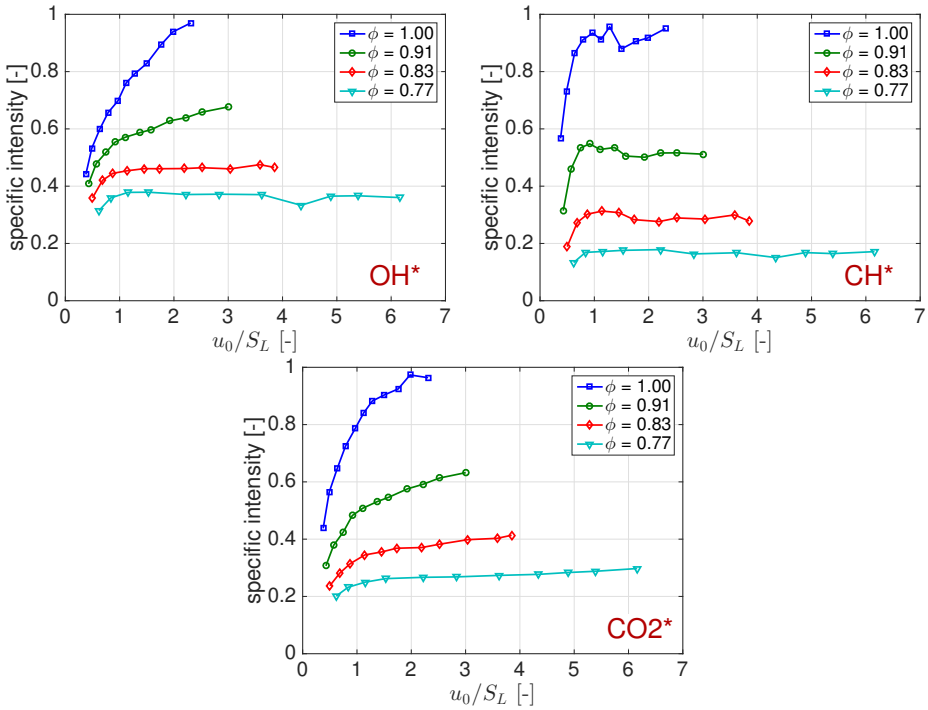

Figure 5.8: *Specific emission intensities I_s^{exp} of OH^*, CH^* and CO_2^* for measurements conducted with the cylindrical multi-perforated burner.*

drops downstream due to the expansion of the flow which occupies the interspace between the holes. As a reference, we still use here the bulk velocity u_0 obtained by dividing the volumetric flow rate by the sum of the surface areas of all injection holes to examine the chemiluminescence results.

Figure 5.8 shows the evolutions of OH^*, CH^* and CO_2^* specific intensities I_s^{exp}. The CH^* curves are similar to those found for the porous plug burner in Fig. 5.6 with two distinct regimes. I_s^{exp} first increases for low u_0/S_L values and then remains constant at high values. The transition between these two regimes is again found close to $u_0/S_L \simeq 1$, though slight deviations are observed in some cases.

There is however a major difference between these data and those found for the porous plug burner when the OH^* and CO_2^* signal evolutions are examined. In Fig. 5.8, the specific intensities I_s^{exp} of the two emissions increase over the whole range of flow rates explored. There is no regime transition observed for $\phi = 1.00$ and $\phi = 0.91$, even at the maximum flow rate tested. Yet for lower equivalence ratios, $\phi = 0.83$ and $\phi = 0.77$, this transition can again be identified around $u_0/S_L \simeq 1$ and a constant specific intensity can be noticed at high flow rates. For the evolution of the CO_2^* emission shown in Fig. 5.8, the flat part is more difficult to reach at high flow rates and we still notice a slight increase of

the specific intensity even at $\phi = 0.77$.

Like for the porous plug burner, these results obtained on the multi-perforated burner indicate that the linear relationship $I \propto \dot{m}$ is not valid for operation at $u_0/S_L < 1$. However, the distinct features of the OH^* and CO_2^* emission signals compared to the CH^* signal suggest that heat losses alter the flame chemiluminescence by different mechanisms in this configuration.

5.4 Specific intensity vs. inlet gas temperature

As explained in Section 5.1, when flame-burner heat exchange takes place, the metallic components of the burner at high temperature cause a preheating of the reactant stream. The raised temperature of the gaseous stream may alter the chemiluminescence intensity and these effects are investigated in this section.

5.4.1 Experimental results

The experiments are carried out on the porous plug burner (see Fig. 5.4). With an upstream electrical heating tube, the reactant stream is supplied at different temperatures from T_u =20 °C to 180 °C. This stream is further heated up when flowing through the hot porous plate to reach the temperature T_0 at the burner outlet. This temperature T_0 is measured with the method described in Section 2.6.2. The power ranges between 0.6 and 1.8 kW and the equivalence ratio is set to $\phi = 1.00$.

The specific chemiluminescence intensity is plotted in Fig. 5.9 as a function of T_0 for different values of the mass flux f_0 injected. The corresponding value of u_0/S_L is a function of both f_0 and T_0. They are indicated in Fig. 5.9.a at the limits of each data set for information.

Two distinct behaviors are observed in this figure. First, for $f_0 = 6.81 \times 10^{-2}$ g cm^{-2} s^{-1}, the data in blue lie in the regime $u_0/S_L > 1$, corresponding hence to freely-propagating flames. In this case the OH^*, CH^* and CO_2^* chemiluminescence intensities all increase with the reactant stream temperature T_0. On the other hand, for $f_0 = 3.79 \times 10^{-2}$, 3.05×10^{-2} and 2.27×10^{-2} g cm^{-2} s^{-1}, the ratio u_0/S_L is way below unity. These conditions correspond thus to planar flames stabilized above the burner by heat loss. In this case, the OH^*, CH^* and CO_2^* intensities are found to be independent of T_0, at least over the temperature range investigated. Results obtained for $f_0 = 4.92 \times 10^{-2}$ g cm^{-2} s^{-1} lie in the regime $u_0/S_L \leq 1$, but are very close to the limit ($u_0/S_L = 1$). Due to the nonuniform velocity distribution of the gas flow at the porous plug burner out-

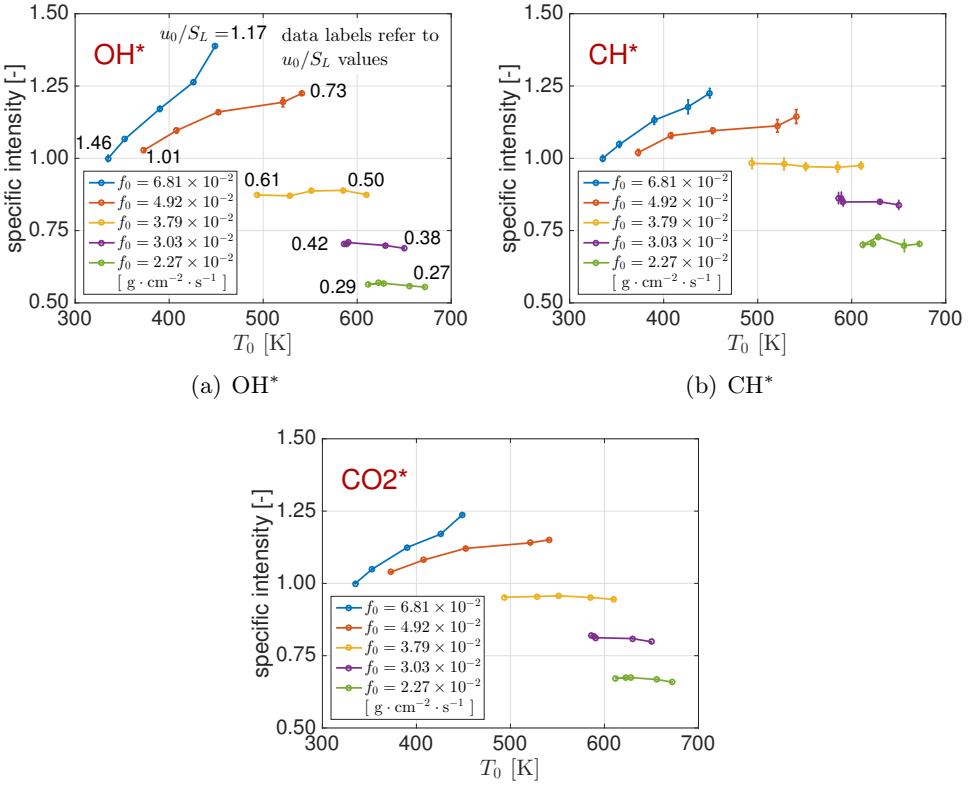

(a) OH*

(b) CH*

(c) CO_2^*

Figure 5.9: *Evolution of the chemiluminescence intensity with the reactant stream temperature T_0 measured on the porous plug burner for stoichiometric mixtures $\phi = 1.00$. The corresponding values for u_0/S_L are indicated at the two ends of each data set gathered at a fixed burning flux f_0 in the left plot. These limits are the same for the two other plots.*

let, the gas velocity can locally exceed S_L even though the global mean speed u_0 still remains below S_L. In these flow conditions, part the reaction layer detaches from the burner surface and takes a corrugated shape, while the other part remains planar and well attached to the burner. In this case, the OH*, CH* and CO_2^* chemiluminescence intensities slightly increase with T_0, but with a reduced slope.

It is also worth pointing out that the set of data in blue in Fig. 5.9, though obtained for a fixed mass burning flux of $f_0 = 6.81 \times 10^{-2}\,\mathrm{g\,cm^{-2}\,s^{-1}}$, is indeed the same for any adiabatic flame with $u_0/S_L \geq 1$, because the specific intensities have been found to be independent of the mixture mass flow rate $\dot{m}$ (or mass burning flux f_0) in this regime. This is highlighted by the fact that the first point of the red data set obtained for $f_0 = 4.92 \times 10^{-2}\,\mathrm{g\,cm^{-2}\,s^{-1}}$ and $u_0/S_L = 1.01$ in Fig. 5.9 lies close to the blue data set obtained for

$f_0 = 6.81 \times 10^{-2}\,\mathrm{g\,cm^{-2}\,s^{-1}}$.

5.4.2 Discussion on preheating

Effects of preheating were ignored in Section 5.3 when studying the influence of the mass flow rate injected in the system on the flame chemiluminescence intensities. A discussion of this issue is now conducted.

It has been shown that for planar flames stabilized by heat losses, the temperature T_0 has no effect on the chemiluminescence intensity in Fig. 5.9 when $u_0/S_L \lesssim 0.6$. For $u_0/S_L > 1$, the chemiluminescence intensity is altered by T_0, but Fig. 5.3.a also reveals that changes of T_0 are relatively small in this regime, and consequently this temperature barely modifies the measured signal. However, when $0.6 \lesssim u_0/S_L \lesssim 1$, the flames are stabilized over the porous plug burner in a complex fashion with a corrugated pattern exhibiting conical and planar patterns. In this regime, variations of T_0 with the flow rate cannot be neglected. As a consequence, the specific intensity plotted in Fig. 5.6 also includes the contribution of T_0, which moves the experimental points a bit upward for $0.6 \lesssim u_0/S_L \lesssim 1$ and leaves unchanged intensity values for $u_0/S_L \lesssim 0.6$ and $u_0/S_L > 1$.

The conclusion drawn for the porous plug burner that the chemiluminescence intensity remains independent of the gas temperature T_0 when $u_0/S_L < 1$ cannot easily be extended to the cylindrical multi-perforated burner. In Section 9.4, the OH^* intensity is observed to change with the burner temperature over time even for $u_0/S_L < 1$. Indeed, the globally averaged values u_0 and S_L are not well suited to describe local variations. In addition, the conclusions obtained under steady conditions may not be applicable to the transitional state when the temperature is not stabilized.

5.4.3 Numerical results

The OH^* and CH^* specific intensities calculated with the numerical model are plotted in Fig. 5.10 as a function of the bulk gas temperature T_0, together with the experimental results (circles with error bars). The scales are adapted using the experimental and numerical data for $f_0 = 2.27 \times 10^{-2}\,\mathrm{g\,cm^{-2}\,s^{-1}}$ as a reference. The blue curves in the two graphs in Fig. 5.10 for $u_0/S_L = 1$ are calculated with the freely-propagating flame model. As explained above, these numerical results are valid for any flame with $u_0/S_L \geq 1$. The other curves are simulated with the burner-stabilized non-adiabatic flame model when $u_0/S_L < 1$.

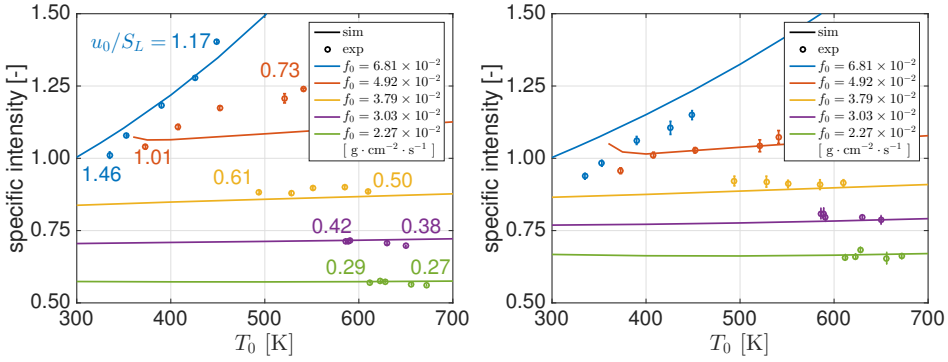

(a) OH* (b) CH*

Figure 5.10: *Evolution of OH* and CH* chemiluminescence intensities for stoichiometric mixtures $\phi = 1.00$ and the porous plug burner with the reactant stream temperature T_0. Lines : simulations. Circles : measurements. Scales are adapted with the experimental and simulation results for the reference mass burning flux* $f_0 = 2.27 \times 10^{-2}\,\mathrm{g\,cm^{-2}\,s^{-1}}$.

In both experiments and simulations, the specific intensity increases with T_0 for $u_0/S_L \geq 1$, while for $u_0/S_L < 1$, the specific intensity remains quasi-constant, with a relative variation of less than 5% over the range $T_0 = 300 - 700\,\mathrm{K}$. Simulations reproduce well the experiments for the OH* and CH* signals in most cases. One difference between experiments and simulations concerns results for $f_0 = 4.92 \times 10^{-2}\,\mathrm{g\,cm^{-2}\,s^{-1}}$ where the slope of the numerical predictions for OH* is smaller than the one found in the measurements. This is attributed to the non-uniformity of the gas velocity distribution at the burner outlet in the experiments, a feature which is not considered in the numerical model.

5.5 Specific intensity vs. burnt gas temperature

The above experiments and simulations reveal that the specific chemiluminescence intensity I_s is altered by the normalized bulk velocity u_0/S_L and the reactant stream temperature T_0 at the injector outlet. In this section, a similar approach as the one used in Section 4.2 is made to unify the different results presented above by exploiting the simulations.

The OH* and CH* specific intensities are plotted in Fig. 5.11 as a function of the burnt gas temperature T_b. For each data series, either u_0/S_L or T_0 is kept constant and the other quantity varies. The numerical data, calculated for different operating conditions, all collapse on a unique curve, highlighting thus a correlation between the burnt gas temperature T_b and the specific intensity I_s^{sim}.

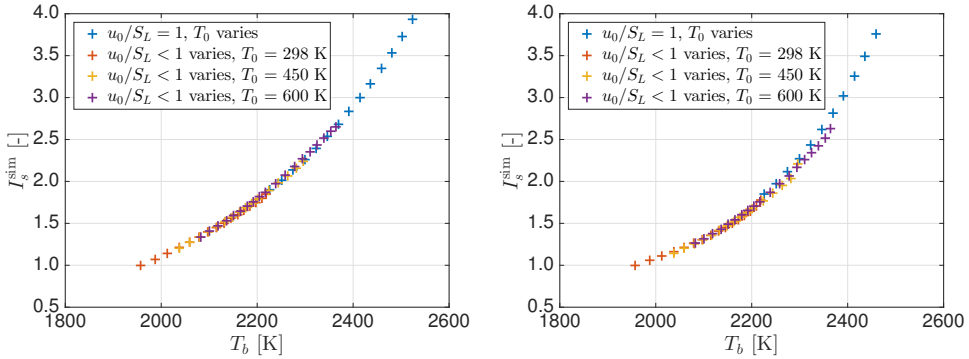

(a) OH* (b) CH*

Figure 5.11: *Evolution of the specific intensity I_s^{sim} with the burnt gas temperature T_b calculated by the REGATH solver.*

This observation indicates that heat losses alter the chemiluminescence intensity mainly through a change of the burnt gas temperature, probably because most reactions, including the chemiluminescence related ones, take place at high temperatures close to T_b. The correlation is better than the one found in Fig. 4.2 because the numerical calculations are done with a fixed fuel (pure methane) and equivalence ratio ($\phi = 1.0$) and the temperature becomes the unique dominant factor.

The influence of the inlet gas temperature T_0 for operation at a fixed mass burning flux f_0 in the regime of $u_0/S_L < 1$ is not directly visible in Fig. 5.11. It is demonstrated here that the same correlation is also valid in this case. The evolution of T_b with T_0 is presented in Fig. 5.12 for $u_0/S_L = 1$ and various mass burning fluxes f_0 in the regime $u_0/S_L < 1$. The burnt gas temperature T_b is in this case barely altered by T_0. Changes of T_b are two orders of magnitude lower than the differences of T_0. Therefore each curve in Fig. 5.10 and Fig. 5.12 ($u_0/S_L < 1$) becomes a single point in Fig. 5.11.

The quasi-constant temperature T_b observed in the simulations is due to the fact that there is no significant change of the total enthalpy in the system when the reactant stream temperature T_0 is varied. When T_0 at the burner outlet increases, the chemical reactions start earlier and bring the flame closer to the porous wall. The simulations suggest that the heat loss also increases in this case, and approximately equals the excess enthalpy of the reactant stream flowing out of the burner at a higher temperature T_0. This balance explains why the burnt gas temperature T_b remains almost unchanged.

This thermal energy balance may be analytically understood by examining the boundary conditions Eqs. (3.14) to (3.16) of the numerical flame model. The mass burning flux $f = \rho u$ remains constant over the whole numerical domain.

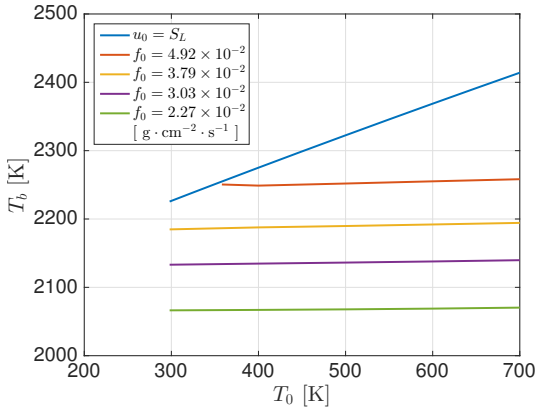

Figure 5.12: *Evolution of the burnt gas temperature T_b with the reactant stream temperature T_0 calculated by the REGATH solver.*

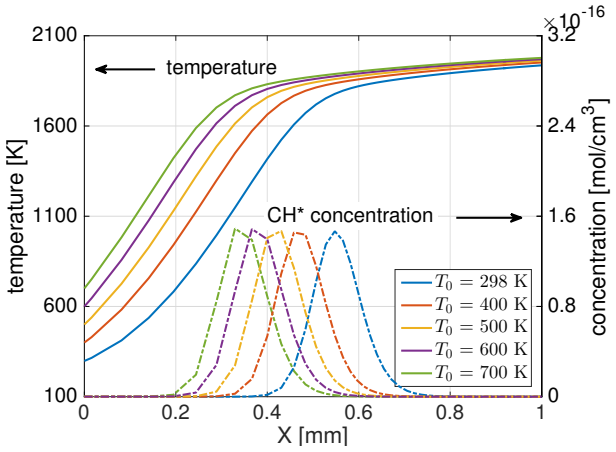

Figure 5.13: *Temperature and CH* concentration profiles for $T_0 = 298 - 700\,\mathrm{K}$ and $f_0 = 3.79 \times 10^{-2}\,\mathrm{g\,cm^{-2}\,s^{-1}}$.*

Also, before the chemical reactions take place in the reaction zone (roughly before $T = 1400\,\mathrm{k}$), the term $W_k\dot{\omega}_k$ in the species balance Eq. 3.2 is virtually 0 hence $Y_k + (\rho Y_k V_k/\rho_0 u_0)$ remains roughly constant. As a result, numerical solutions for the temperature and species mass fraction profiles for a different value of T_0 can be obtained through a translation of an existing solution as long as the inlet boundary condition $x = 0$ still remains in the preheating zone. As the temperature gradient vanishes at $x = +\infty$, the burnt gas temperature T_b remains unchanged by this translation.

An illustration of this process for the temperature T and CH* mass fraction profiles is given in Fig. 5.13 for different inlet temperatures T_0 and a fixed mass burning flux $f_0 = 3.79 \times 10^{-2}\,\mathrm{g\,cm^{-2}\,s^{-1}}$. Figure 5.13 clearly reveals that a translation of the temperature profile to the left leads to larger values of the

temperature gradient dT/dx at $x = 0$, and hence also to a larger heat flux from the flame to the burner.

5.6 Impact on the CH^*/OH^* ratio

Since the evolution of chemiluminescence signal with the gas flow rate is found to be nonlinear in regimes with heat loss to the burner, it is worth exploring if the use of the CH^*/OH^* intensity ratio still allows to remove the impact of power as for the determination of the equivalence ratio.

The CH^*/OH^* intensity ratio deduced from the experiments made with the three burners are presented in Fig. 5.14. In addition, numerical results are compared with experimental data for the porous plug burner in Fig. 5.14.b. The numerical results are multiplied by a factor of 2.3 to take into account the response function of the spectrometer.

For the conical flame burner, the CH^*/OH^* values in Fig. 5.14.a are independent of the normalized injection velocity u_0/S_L. As already discussed, heat transfer to the burner remains weak in this configuration and the burner operates mainly in an adiabatic mode.

For the porous plug burner, experimental results of CH^*/OH^* ratio values (circles in Fig. 5.14.b) remain approximately constant in the $u_0/S_L > 1$ regime. In the other regime $u_0/S_L < 1$, the CH^*/OH^* ratio slightly increases when u_0/S_L is reduced, especially for the equivalence ratios $\phi = 0.91$ and 1.00. The trend of CH^*/OH^* is also reproduced by the simulations. The curves are calculated with the burner-stabilized flame model for $u_0/S_L < 1$ (solid lines) and the 1-D freely-propagating flame model for $u_0/S_L > 1$ (dashed-dotted lines).

For the cylindrical multi-perforated burner, the CH^*/OH^* values in Fig. 5.14.c do not remain constant for $\phi = 1.00$ and 0.91 when u_0/S_L varies. It was already shown in Fig. 5.8 that the OH^* and CH^* intensities are modified by heat losses in different ways for mixtures close to stoichiometry. This feature also explains the separation of the CH^*/OH^* curves in Fig. 4.4 close to the stoichiometry. Nevertheless, when the equivalence ratio drops below $\phi \leq 0.83$, the CH^*/OH^* ratio becomes again roughly independent of the normalized bulk injection velocity u_0/S_L. In particular, it is noticed that the response at $\phi = 0.77$ is perfectly flat.

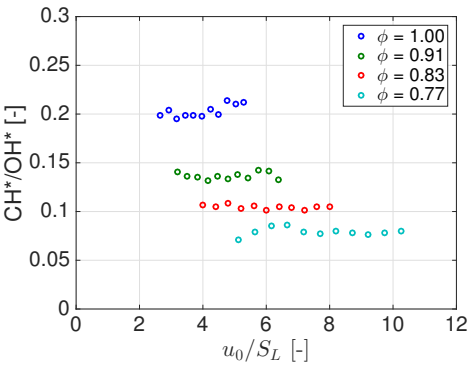

(a) Experiments on the conical flame burner

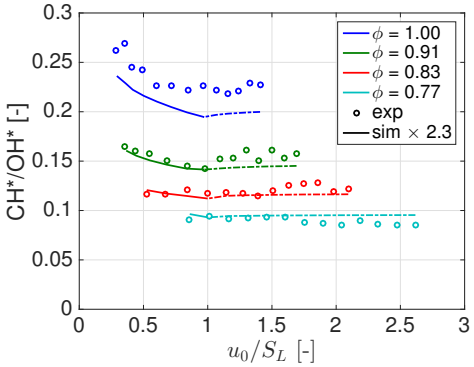

(b) Experiments (circles) on the porous plug burner and numerical simulations (lines).

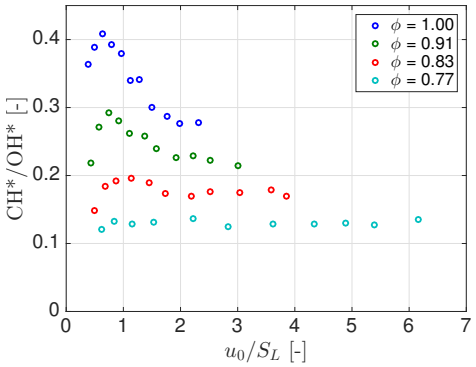

(c) Experiments on the multi-perforated burner

Figure 5.14: *Evolutions of CH^*/OH^* ratios with $u_0/S_L < 1$.*

Conclusion

The heat exchange taking place between planar flames and the burner surface when the gaseous flow velocity at the burner outlet drops below the adiabatic burning velocity ($u_0/S_L < 1$) is found to alter the flame chemiluminescence intensity.

The chemiluminescence signal is proportional to the gas flow rate only for freely-propagating adiabatic flames when $u_0/S_L \geq 1$. The change of the chemiluminescence signal with the gas flow rate is nonlinear for burner-stabilized flames with heat losses when $u_0/S_L < 1$.

In addition, a higher inlet gas temperature T_0 is observed to enhance the chemiluminescence signal for adiabatic flames in the regime $u_0/S_L \geq 1$, but increas-

ing this temperature has little impact for flames stabilized by heat losses when $u_0/S_L < 1$. However, this latter conclusion obtained for the porous-plug burner in which the flow velocity remains roughly uniform needs to be taken with caution and cannot easily be extended to the cylindrical multi-perforated burner.

The 1-D flame simulations conducted with the REGATH flow solver confirm these observations and allow quantitative comparisons with experiments as long as the flame remain planar.

The numerical approach also reveals that the effects of both the gaseous flow velocity u_0 and the inlet gas temperature T_0 result indeed from the changes of burnt gas temperature. This observations leads to a unique rule unifying the findings in this chapter.

Finally, the CH^*/OH^* intensity ratio is also observed to be altered by the flame-burner heat exchange.

Chapter 6

Disturbing factors for chemiluminescence characterization.

This chapter adresses several mechanisms altering the chemiluminescence signal. Different interfering phenomena are identified including light emissions from radicals in the post-flame zone, the impact of downstream confinement of the combustion zone, and the light absorption by ground state OH radicals. Some knowledge on these effects is necessary to safely exploit the chemiluminescence signal and infer the equivalence ratio in real domestic gas boilers.

6.1 Spatial distribution of flame chemiluminescence

The flame chemiluminescence recorded with the optical setup in Fig. 2.11 yields a signal integrated along the line-of-sight. The spectrometer cannot differentiate the origin of light emissions. With the field of view set as in Fig. 2.12, the resulting spectrum contains contributions from the region of flame front and of burnt gases. A precise knowledge of the spatial origin of the light emission is important to get a correct characterization of the flame chemiluminescence spectrum in a real gas boiler.

A series of experiments are made in the following to analyze the light emissions originating from the flame front and from the burnt gases. Measurements are carried out with the three burners presented in Section 2.1, *i.e.*, the conical flame burner, the porous plug burner and the cylindrical multi-perforated burner. They all give useful information on different aspects.

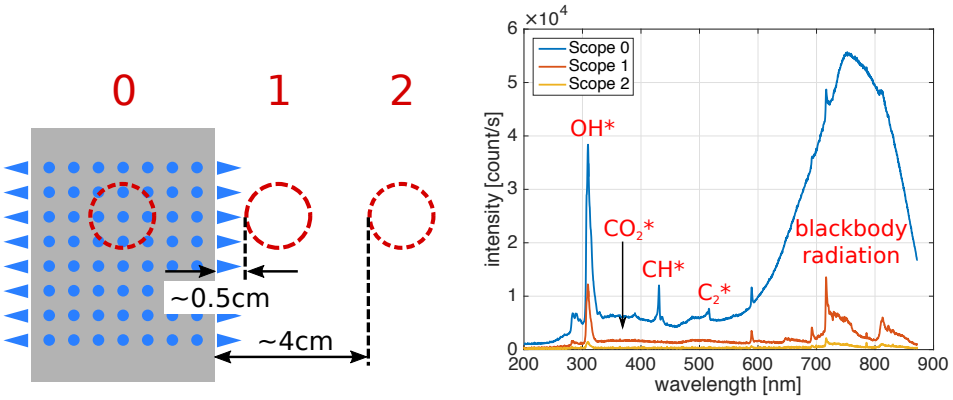

(a) Field of view (b) Spectrum

Figure 6.1: *Characterization of the spatial distribution of chemiluminescence signal for the cylindrical multi-perforated burner. Experiments are made without quartz tube around the burner.*

6.1.1 Cylindrical multi-perforated burner

Experiments are first carried out with the cylindrical multi-perforated burner, operating at $P = 13\,\text{kW}$ and $\phi = 1.0$. The quartz tube around the burner is removed to avoid any reflections in the following experiments.

All the spectra on this burner in previous chapters are obtained with a fixed scope shown in Fig. 2.12.c, or scope marked "0" in Fig. 6.1. The light collected from this region originates from the burner surface, the flame front, and the downstream burnt gases. The corresponding spectrum in Fig. 6.1.b (blue line) contains the contributions from the chemiluminescence emissions of OH^* (309 nm), CH^* (431 nm), CO_2^* (300-600 nm) and C_2^* (516 nm) radicals, and several peaks in the red and near infrared ranges, including the sodium peak at 589 nm, superposed on the continuous spectrum due to thermal radiation from the burner hot metallic components at wavelengths higher than 500 nm.

To investigate the emissions from the burnt gases, the optical system is slightly turned to probe the downstream region marked "1" in Fig. 6.1.a. The border of the investigated field of view lies at a distance of about 0.5 cm from the burner surface. This probed region thus excludes the flame front. In the corresponding spectrum (red line) in Fig. 6.1.b, the CH^* and C_2^* emissions, as well as the continuous thermal radiation from the burner surface, are absent. This means that CH^* and C_2^* are produced only in the flame front. However, the OH^* and CO_2^* signals are still detected, so they are also emitted from the burnt gases. The conclusion is confirmed by a third spectrum recorded further away from the burner surface at about 4 cm (yellow line) in Fig. 6.1.b, with the corresponding

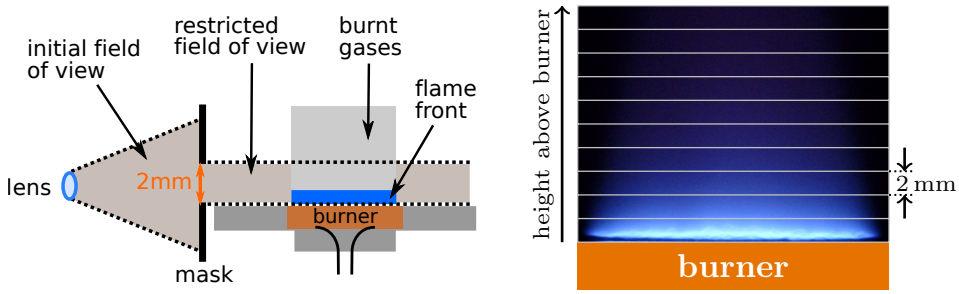

(a) Field of view (b) Photo

Figure 6.2: *Configuration for the measurement of flame spectrum by slice above the porous plug burner.*

scope is marked "3" in Fig. 6.1.a, although the OH^* and CO_2^* intensities are much reduced.

6.1.2 Porous plug burner

The investigation then continues with the porous plug burner. The relatively simple 1-D geometry of the flame allows for a more detailed study of the spatial distribution of the chemiluminescence signal. Instead of integrating the whole flame region as in Fig. 2.12.b, a mask with a 2 mm × 100 mm rectangular aperture is set between the flames and the lens, restricting the field of view to a slice of 2 mm height as shown in Fig. 6.2.a. The mask together with the lens is then moved in the vertical direction to perform a slice-by-slice scan of the chemiluminescence emission signal.

The burner operates at $P = 1.0\,\text{kW}$ and $\phi = 1.0$, corresponding to $u_0/S_L = 0.6$. The flame front is in this case thin and relatively flat with a reaction sheet stabilized just above the burner surface. Figure 6.2.b reveals tiny corrugations of flame front due to the nonuniform velocity distribution at the porous plate outlet, but the entire combustion reaction layer stay within the first 2 mm slice above the burner.

In addition, measurements carried out in this configuration are compared with numerical results obtained with the REGATH solver under the same conditions. Figure 6.3 gives the resulting OH^* and CH^* profiles calculated for a methane-air flame at $\phi = 1.0$ and $u_0/S_L = 0.6$. The emission intensity of n^{th} slice is determined in the simulation as:

$$I_n = \int_{(n-1)\Delta L}^{n\Delta L} y_k c_k dx \tag{6.1}$$

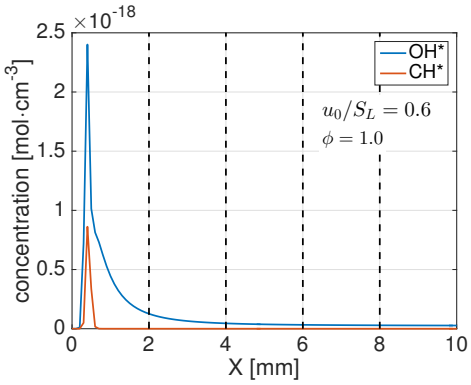

Figure 6.3: *Numerical results on the concentration profiles of OH* and CH* of a burner-stabilized methane-air flame with* $\phi = 1.0$ *and* $u_0/S_L = 0.6$.

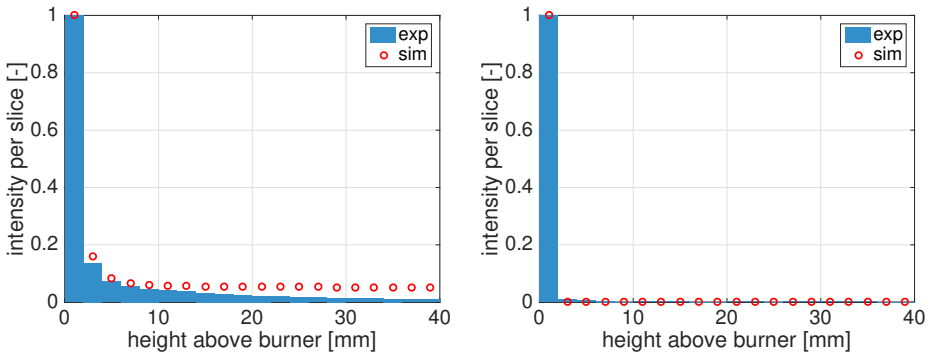

(a) OH* (b) CH*

Figure 6.4: *Experimental (blue bars) and numerical (red circles) results of OH* and CH* intensities along the vertical axis above the porous plug burner. Intensity values are normalized by their values within the first slice above the burner.*

with $\Delta L = 2\,\text{mm}$.

To ease the comparison, the OH* and CH* emission intensities obtained from experiments and numerical simulations are normalized by their values in the first slice above the burner. Results plotted in Fig. 6.4 are consistent with the observations made on the cylindrical multi-perforated burner. The CH* emission is present only within the first 2 mm slice, while the OH* emission continues further downstream. Numerical results for the OH* intensity are coherent with the experimental data for the first slices, but the drop observed further downstream beyond 10 mm is not reproduced. This drop may result from the lower burnt gas temperature downstream in the experiments due to their dilution with the surrounding air, which is not considered in the numerical model.

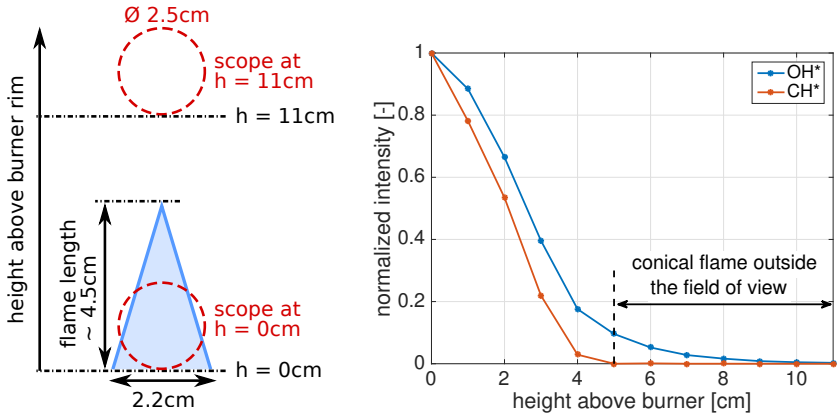

(a) Field of view (b) OH^* and CH^* intensity

Figure 6.5: *Measurement of the spatial distribution of chemiluminescence intensity above the conical flame burner.*

6.1.3 Conical flame burner

Experiments are then conducted with a nearly adiabatic conical flame at $P = 1.8\,\text{kW}$ and $\phi = 1.0$. The resulting flame length is about 4.5 cm. The spectrometer field of view corresponds to a disk of 2.5 cm diameter in Fig. 6.5.a. In this way the optical acquisition system does not cover the entire flame region as in Fig. 2.12.a. The lens is then moved upwards and spectra are recorded every one centimeter from $h = 0$ to 11 cm where h is the height above the burner. At $h = 5\,\text{cm}$, the conical flame reaction layer lies fully outside the spectrometer field of view. The CH^* intensity then drops to zero, while OH^* emission continues further downstream in Fig. 6.5.b.

The relatively stronger light signal obtained from the conical flame enables further analysis of the OH^* spectrum structure. Figure 6.6 shows a zoom of the OH^* peak structure with the scope of the spectrometer at different heights above the burner outlet varying from $h = 0$ to 11 cm. All spectra are normalized by the intensity value at 309 nm. It is seen that the shapes of the OH^* peaks are not all self-similar.

From $h = 0$ to 4 cm, the spectrum includes the contributions of both the flame reaction layer and the burnt gases. The contribution from the flame front gradually decreases as the height h increases. In the corresponding spectra, the emission intensity above 312 nm, attributed to $A^2\Sigma^+(\nu' = 0) \rightarrow X^2\Pi_i(\nu'' = 0)$, decreases faster than the emission below 312 nm, attributed to $A^2\Sigma^+(\nu' = 1) \rightarrow X^2\Pi_i(\nu'' = 1)$. For $h \geq 5\,\text{cm}$, only the light emission from the burnt gases is collected by the spectrometer. The shapes of the OH^* intensity distributions are in this case self-similar.

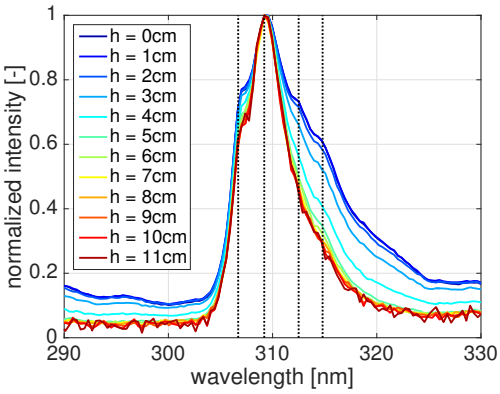

Figure 6.6: *Structure of the OH* spectrum gathered for a conical methane/air flame with the scope of the spectrometer at different heights above the burner rim. Dotted lines correspond to the wavelengths* 306.7 nm, 309.2 nm, 312.5 nm *and* 314.8 nm. *The fine structure of the spectrum is not visible due to 2 nm resolution of the spectrometer.*

This observation indicates that the OH* emissions from the flame front and the burnt gases have different spectral structures. The emission related to the transition $A^2\Sigma^+(\nu' = 1) \rightarrow X^2\Pi_i(\nu'' = 1)$ is either weaker or absent in the burnt gases. However, the current device resolution does not allow for a more detailed investigation.

6.2 Downstream confinement

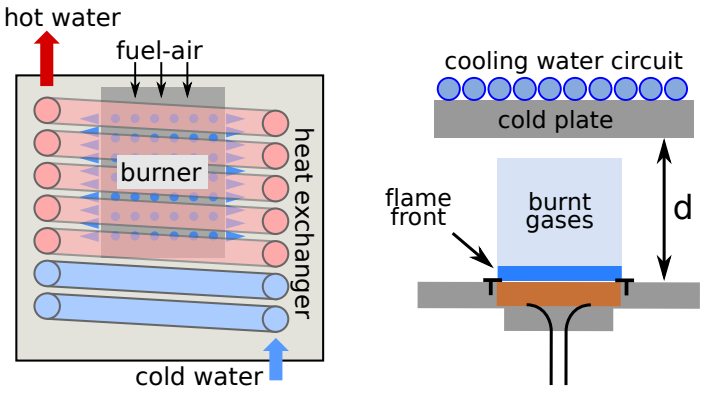

(a) Setup in a real gas boiler (b) Setup in laboratory

Figure 6.7: *Burner setups with heat exchanger downstream the flame.*

In a gas boiler, a heat exchanger is set around the burner to collect the heat released by the combustion (Fig. 6.7.a). The presence of the heat exchanger

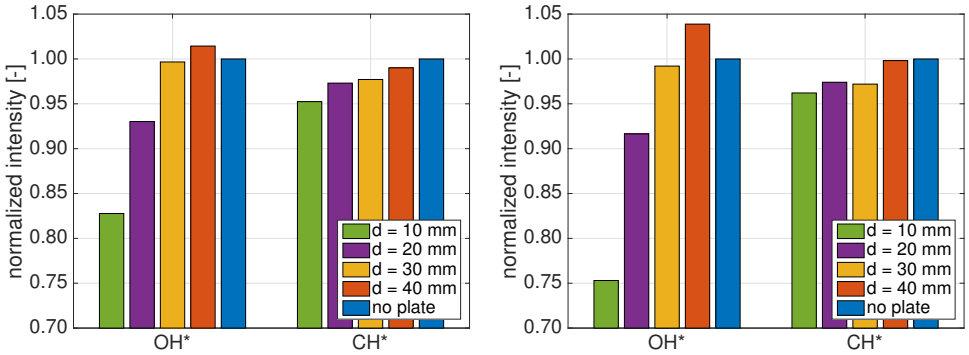

(a) Results obtained by measuring the total emission

(b) Results obtained summation over all 2 mm slices

Figure 6.8: *OH* and CH* intensities with the cold plate at increasing distances $d = 10$ to 40 mm from the burner surface. The intensity without cold plate (blue bar) is used as reference to normalize the results.*

may modify the flame chemiluminescence emission, especially when its distance to the burner surface is small.

The experimental setup shown in Fig. 6.7.b mimics this situation in which the effect of a heat exchanger can be analyzed. A water-cooled metallic plate is added downstream the flame at a distance d, adjustable during the experiments. The flow rate of cooling water is adjusted so as not to condensate the water vapor from the burnt gases on the cooled surface.

The chemiluminescence intensity is recorded with two methods:

- A direct measurement of the total emission is made with the spectrometer and the field of view set as in Fig. 2.12.b. The effective field of view is a semicircular region with a radius of about 5 cm above the burner plate.
- A summation of the emission intensity is made per 2 mm slice along the axis, with the optical acquisition system configured as in Fig. 6.2.a. The effective field of view is a rectangular region of 10 cm wide and a height corresponding to the burner-plate distance d.

Figure 6.8 shows the OH* and CH* intensities measured with the cold plate set at distances varying between $d = 10$ to 40 mm. An additional measurement without cold plate serves as a reference. Both methods give similar results. The OH* intensity is considerably reduced when the cold plate is set at $d = 10$ and 20 mm, but this signal remains stable once the cold plate is moved to $d = 30$ mm or further away. The CH* intensity is barely altered by the presence of the cold plate.

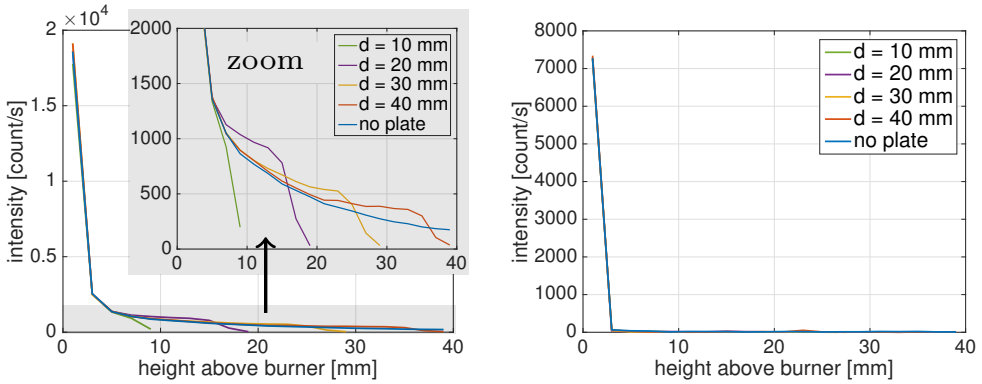

(a) OH^* (b) CH^*

Figure 6.9: *OH^* and CH^* intensity along the vertical axis with the cold plate at a distance d from the burner.*

Apart from offering a support for the direct measurement of total intensity, the slice-by-slice technique allows in addition to see the evolution of emission intensities along the vertical axis. The evolutions of the OH^* and CH^* profiles with the cold plate distance varying from $d = 10$ to 40 mm is plotted in Fig. 6.9. The profiles measured without cold plate serve again as a reference.

All the OH^* emission profiles with the cooling plate collapse at short distances in Fig. 6.9.a on the distribution measured for the reference signal (black) obtained without plate. When the flow approaches the cold plate, the OH^* intensity first slightly increases with respect to the reference curve and then suddenly drops to zero about 2 mm before reaching the plate. This is probably due to the lower temperature of the flow near the cooled plate that quenches the approaching radicals leading to a drop of the OH^* intensity over a short distance between the burner and the cold plate in Fig. 6.8. The slight increase of the OH^* intensity seen just before the sudden drop may be attributed to the initially upward burnt gas flow diverted in the radial direction.

Figure 6.9.b confirms the previous observations made for the CH^* emission, which is only found in the flame reaction layer. As no CH^* emission is present in the burnt gases, the cooling plate does not show significant impact on this signal and all measurements collapse on the same curve in Fig. 6.9.b.

6.3 Light absorption of ground state OH radicals

The phenomenon of light absorption by the ground state OH radicals has been explained in Section 1.2.3. It is now observed on the cylindrical multi-perforated

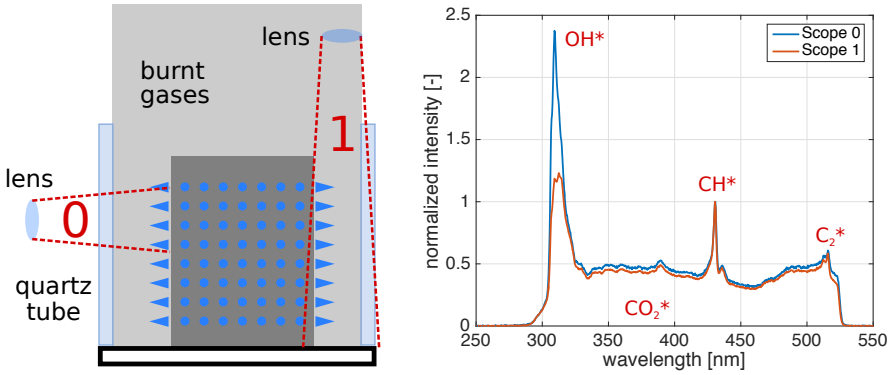

(a) Angle of observation (b) Spectrum

Figure 6.10: *Light absorption by ground state OH radicals in the burnt gases. The spectra in (b) are normalized by the CH* peak height.*

burner operating at $P = 13\,\text{kW}$ and $\phi = 1.0$ in Fig. 6.10.a with a quartz tube to confine the burnt gases.

In these experiments, the angle of observation of the chemiluminescence signal is switched from the "0" to "1" to collect the light from the side of the burner or from the top. The lens collecting the light from the top is set at about 70 cm above the top of the burner. The photons need in this case to travel a relatively long distance within the burnt gases before reaching the collecting lens. The traveling distance in the burnt gases is much shorter for the observation angle marked "0" on the side. In this case the light crosses a 3 cm burnt gas layer between the burner surface and the quartz protection tube.

As the CH* intensity is assumed to be insensitive to the angle of observation, the spectra recorded from the two observation positions are normalized by the CH* peak height in Fig. 6.10.b. The OH* intensity from the observation angle "1" is reduced almost by half compared to the record made at the angle "0". The drop of the OH* signal is attributed to the absorption of OH radicals which are abundant in the burnt gases.

Conclusion

Several disturbing factors of the flame chemiluminescence signal have been considered in this chapter. Due to the presence of OH* and CO_2^* species in the burnt gases and light absorption of ground state OH radicals, the chemiluminescence intensity of these radicals depends on the view angle, the sensor position and the region of the flow scrutinized by the detector. On the other hand, the

CH^* emission intensity only depends on the region scrutinized by the detector, as it only emerges from the reaction layer of the flame.

Consequently, it appears difficult to achieve universally applicable laws to detect the equivalence ratio based only on the exploitation of the OH^*, CO_2^* and CH^* chemiluminescence intensities without consideration of the optical setup. Instead, the sensing strategy needs to be constructed for specific angles of observation and sensor positions.

The impact of the presence of a cold plate, mimicking the heat exchanger in a gas boiler, on the chemiluminescence signal has also been investigated. This device has been found to alter the OH^* chemiluminescence signal when it is set too close to the flame region. However, this perturbation needs only to be considered when the flame is very close to the solid surface.

Part II

Flame ionization current

Chapter 7

Literature review on flame ionization current

This chapter explains the basics of flame ionization current, including the formation of charged species in flame and the flame electrical properties under external bias voltage. A brief literature review is done on the existing flame monitoring techniques exploiting the ionization current.

7.1 Charged species in flames

The electrical conductivity of hydrocarbon flames is related to the ions and electrons created during the combustion process. An extensive review of ions in flames is carried out by Fialkov (1997). The ionization energy required to remove a valence electron from a molecule can be supplied either by the chemical reactions or by the high temperature reached by the flow in the reaction layer. The two corresponding mechanisms are named chemi-ionization and thermal ionization (Franke 2002).

For laminar premixed flames at atmospheric pressure as investigated in the present thesis, the chemi-ionization is the dominant mechanism. The nature of the ions produced is generally studied with mass spectrometry and empirical formula are assigned, though ambiguities may exist for their composition and structure. This type of work has been done for example by Goodings et al. (1979a) and Goodings et al. (1979b) in flat methane-oxygen flames.

Profiles for selected cations (positive ions) under lean ($\phi = 0.216$) and rich ($\phi = 2.15$) conditions taken from these works are reproduced in Fig. 7.1. The position $z = 0$ marks the limit of the luminous zone and the scales have been

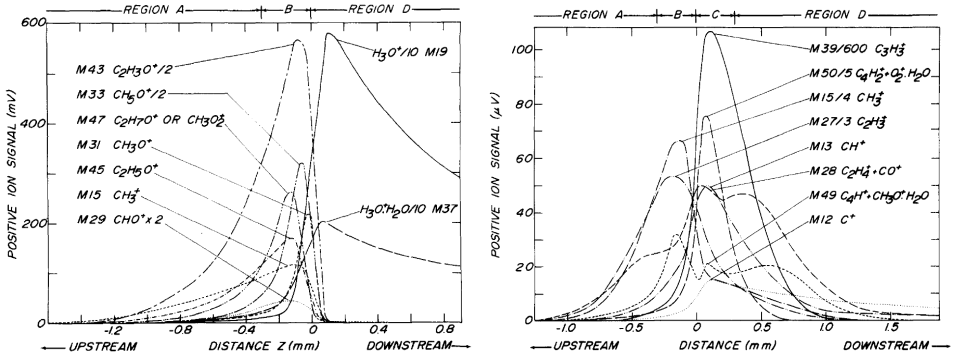

(a) Fuel lean (CH_4-O_2, $\phi = 0.216$) (b) Fuel rich (CH_4-O_2, $\phi = 2.15$)

Figure 7.1: *Selected positive ion profiles for methane-oxygen flat flames (Goodings et al. 1979a). $z = 0$ corresponds to the downstream limit of the luminous zone.* H_3O^+ *and its hydrates* $H_3O^+ \cdot nH_2O$ *are not represented in (b), but their profile is similar to (a).*

adapted to clearly distinguish all profiles in the same graph. It is believed that the ionization process begins with the reaction:

$$CH + O_2 \rightarrow CHO^+ + e^- \tag{7.1}$$

Despite its low concentration in the mixture, CHO^+ is an important species as a source of ionization in hydrocarbon flames (Fialkov 1997; Calcote 1961). The proton in CHO^+ is then transferred to other species with a higher proton affinity.

At lean condition in Fig. 7.1.a obtained for $\phi = 0.215$, the positive ion species identified in the $z < 0$ region include $C_2H_3O^+$, CH_5O^+, $C_2H_7O^+$, etc. Under the fuel-rich condition in Fig. 7.1.a at $\phi = 2.15$, $C_3H_3^+$ has a predominately high concentration. According to Knewstubb and Sugden (1958), its creation is related with the excited radical CH^*:

$$CH^* + C_2H_2 \rightarrow C_3H_3^+ + e^- \tag{7.2}$$

All these species are then almost exclusively converted to H_3O^+ and its hydrates $H_3O^+ \cdot nH_2O$ in the post chemiluminescence zone for both lean and rich conditions (not shown in Fig. 7.1.b). This complex proton exchange process may thus as a first approximation be simplified as:

$$CHO^+ + H_2O \leftrightarrow H_3O^+ + CO \tag{7.3}$$

It is however reminded that the process may be indirect.

The negative charge carriers include anions and free electrons. The free electron profile can be inferred from the difference between the total cation and anion

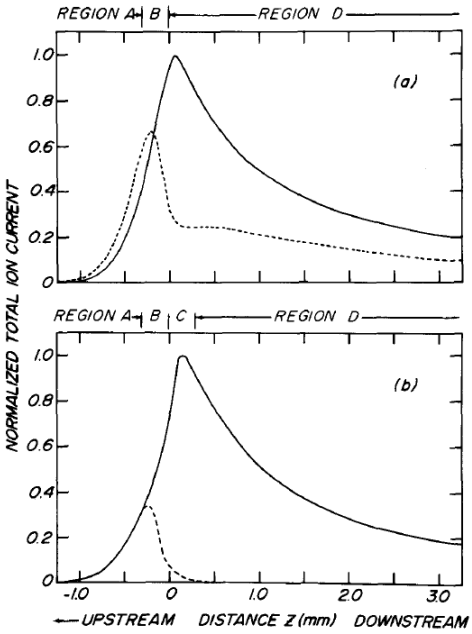

Figure 7.2: *Total positive (solid lines) and negative (dashed lines) ion profiles for (a) fuel-lean and (b) fuel-rich flames. The difference of the two profiles corresponds to free electrons (Goodings et al. 1979b).*

profiles in Fig. 7.2. In the $z < 0$ region at low temperature, free electrons are almost inexistent due to their attachment to electronegative species such as O_2:

$$e^- + O_2 \leftrightarrow O_2^- \tag{7.4}$$

In the post-chemiluminescence region, the negative charge carriers are almost exclusively free electrons for the fuel-rich flame, while for the fuel-lean flame anions and free electrons coexist. In the latter case, the chemical equilibrium between anions and free electrons can be described with the temperature dependent equilibrium constant $K(T)$ (Franke 2002).

Mass spectrometry investigation of ions in a propane-air flame has been carried out by Rodrigues et al. (2007). In the flame front, the concentration of $C_2H_3O^+$ is one order of magnitude higher than any other cation species, while in the post-chemiluminescence region H_3O^+ and its hydrates $H_3O^+ \cdot nH_2O$ are still the most abundant. The major anions include HCO_2^- in the flame front, CO_3^- and HCO_3^- in the burnt gases.

Ionization in a pure hydrogen flames is much weaker. The concentration of the two major charge carriers H_3O^+ and e^- is of the order of $10^9\,cm^{-3}$, compared to $10^{10} - 10^{11}\,cm^{-3}$ in hydrocarbon flames (Fialkov 1997).

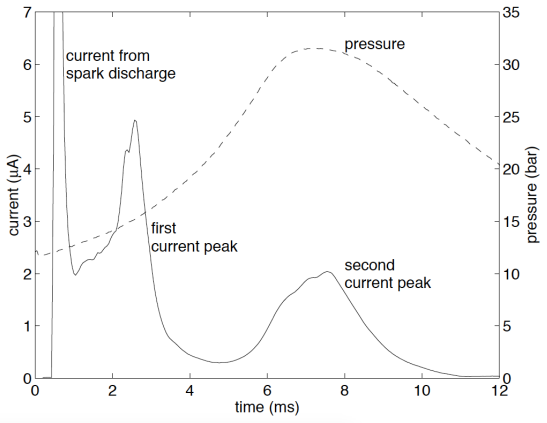

Figure 7.3: *Typical ionization current signal and corresponding pressure measured in an internal combustion engine (Franke 2002).*

7.2 Ionization current

A flame ionization current can be detected when a bias voltage is applied between two electrodes inserted into the flame. In many cases the metallic burner serves as one of the electrodes. Studies of the flame ionization current in industrial burners and engines have been motivated by its potential for flame monitoring, especially in internal combustion engines and domestic gas boilers (Franke 2002; Rodrigues 2005; Karrer et al. 2010; Kiefer et al. 2012).

Franke (2002) studied the ionization current for the purpose of diagnostics in internal combustion engines and some of the results useful for the present work are summarized here. The effects of equivalence ratio and electrodes were investigated in a cubic constant volume combustion chamber. A typical ionization current measured in an internal combustion engine is shown in Fig. 7.3. It is suggested that the first current peak following the spark discharge is due to chemi-ionization, and the second current peak, coinciding with the pressure peak, results from thermal ionization. Measurements were performed with quiescent natural gas - air mixtures at different equivalence ratios. It is found that, for both peaks, the integration of the current over time, corresponding to the charges transferred, is correlated with the equivalence ratio and reaches its maximum at $\phi = 1.1$.

Experiments were also performed in Franke (2002) to understand the effects of the electrode geometry. A disk is attached to one or both of the threaded electrodes. Figure 7.4 taken from Franke (2002) shows a peak when the spherical flame front gets in contact with the disk attached to the cathode. On the other hand, the current is only slightly enhanced when the disk is added on the anode. These results clearly demonstrate the importance of the contact area

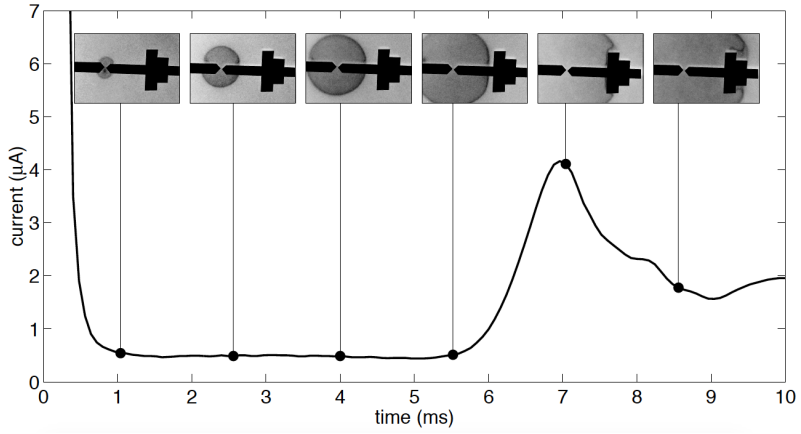

Figure 7.4: *Ionization current signal during the flame development and the corresponding flame photographs (Franke 2002).*

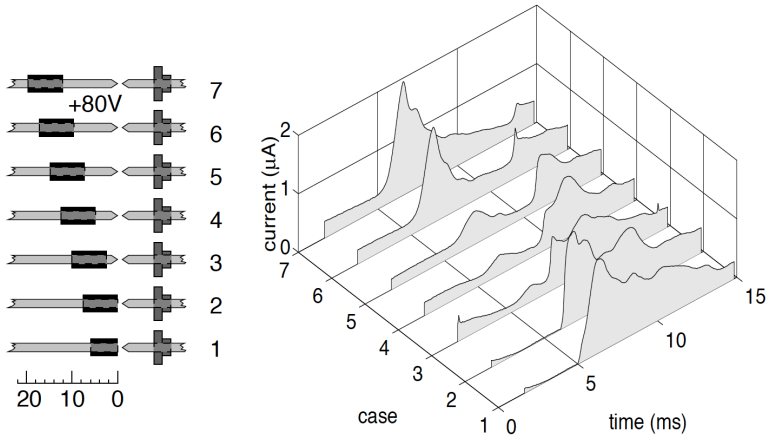

Figure 7.5: *Ionization current signal with a ceramic isolator added on the anode (Franke 2002).*

between the flame front and the cathode, while the shape of the anode is not the limiting factor of the ionization current.

Nevertheless, when a ceramic insulator is added on the anode, as shown in Fig. 7.5 the ionization current signal is suppressed over the time interval when the contact between the flame front and the anode is blocked. It is also worthing noticing that the current is virtually zero when the isolator is located at the tip of the anode. In other cases, a weak residual current can still be detected, as the contact between the anode tip and the burnt gases helps to close the electric circuit.

Rodrigues (2005) measured the distribution of the electrical potential over a pla-

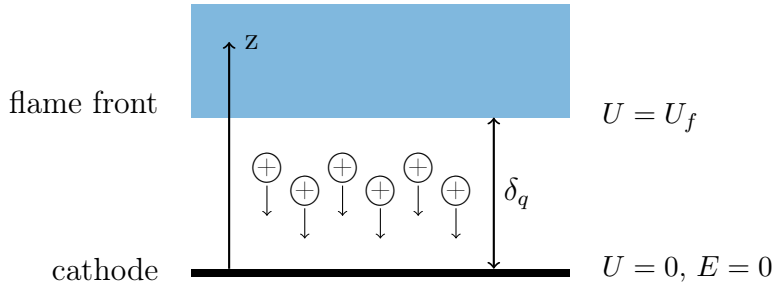

Figure 7.6: *Simplified model for the electrical properties of a flame above the dead space near the cathode.*

nar premixed methane-air flame at $\phi = 0.8$ between two cylindrical electrodes, polarized respectively at +9 V and -9 V. The author found that a voltage drop of 2 V takes place near the anode and a drop of 16 V near the cathode, while the electrical potential is almost constant over the flame in between. The much higher potential drop near the cathode than the anode is suggested to be related to the different charge carriers in the two regions. The current is driven by cations near the cathode, and essentially by free electrons near the anode. The much higher mobility of electrons, thanks to the much smaller mass, makes the voltage drop lower near the anode.

Another interesting conclusion put forward by Rodrigues (2005) and Karrer (2009) is that the ionization current is correlated with the quenching distance between the flame and the cathode. A simplified 1-D model from Karrer (2009) gives an analytical explanation. In Fig. 7.6, the flame front stays at a distance of δ_q from the negatively biased electrode. The investigated zone in the vicinity of the cathode is devoid of free electrons and anions as the electrical field pushes negative charge carriers away from the electrode. The current is then only driven by the cations:

$$j = j_i + j_e \sim j_i = e n_i \mu_i E \tag{7.5}$$

where j is the current density, e the elementary charge of an electron, n the concentration number of charges, μ the mobility of the carrier and E the electrical field. The subscripts i and e stand respectively for (positive) ions and free electrons. The electrical field can be determined with the Poisson equation:

$$\frac{dE}{dz} = \frac{e(n_i - n_e)}{\epsilon_0} \sim \frac{e n_i}{\epsilon_0} = \frac{j}{\mu_i \epsilon_0 E} \tag{7.6}$$

Considering in addition $E = dU/dz$ and the boundary conditions $U\big|_{z=0} = 0$, $U\big|_{z=\delta_q} = U_f$, $E\big|_{z=0} = 0$, the current density can be determined:

$$j = \frac{9 \mu_i \epsilon_0 U_f^2}{8 \delta_q^3} \tag{7.7}$$

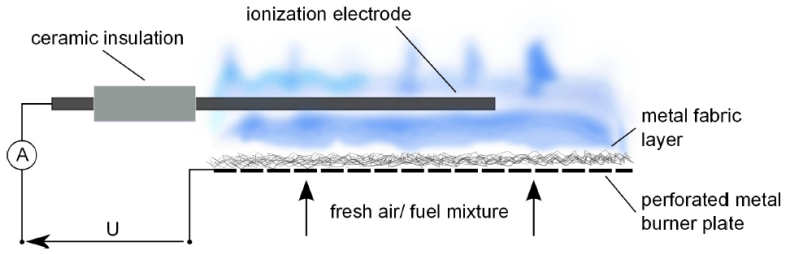

Figure 7.7: *Ionization current sensing setup in a domestic gas boiler (Kiefer et al. 2012).*

Since U_f is approximately constant, the ionization current density j decrease as δ_q^{-3} when the quenching distance δ_q increases.

7.3 Flame monitoring with ionization current

The flame ionization current is widely used in domestic gas boilers, but for a long time only as a flame detector. More recently, applications to flame state monitoring are emerging as the current intensity has been shown to be related to the flame equivalence ratio (Kiefer et al. 2012; Näslund 2014).

The configuration for ionization current detection is generally very simple. A schematic from Kiefer et al. (2012) gives an example in Fig. 7.7. The metallic burner surface is used as one of the electrode and a voltage is applied on an ionization probe inserted into the flame.

Kiefer et al. (2012) have also developed a simple strategy to control the combustion state with the ionization current. The air flow rate is adjusted by the fan speed according to the required burner power, and the fuel flow rate is set by the opening gas valve to achieve the optimum equivalence ratio. As the current intensity changes monotonically with the equivalence ratio, a set point can be determined according to the curve plotted in Fig. 7.8.a. When the current intensity shifts from the value due to variations of equivalence ratio, the opening of the natural gas valve is adapted to bring it back to the optimized point. However, Figure 7.8.b also shows that the ionization current is also impacted by the burner load. Therefore the current set point is also a function of burner load.

Boilers equipped with ionization current based combustion control systems are already emerging. Tests have shown that the control system considerably improves the reduction of CO and NOx emissions for natural gas with higher or lower calorific values (Näslund 2014). However, some technical reports have

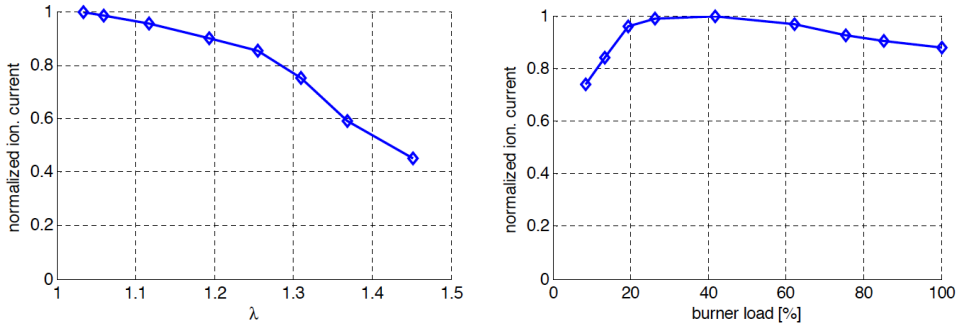

(a) Ionization current *vs.* λ ($\lambda = 1/\phi$), with constant burner load

(b) Ionization current *vs.* burner load, with constant equivalence ratio ($\phi = 0.8$)

Figure 7.8: *Evolution of ionization current with equivalence ratio and burner load in a domestic gas boiler (Kiefer et al. 2012).*

shown that the system is unable to adjust the equivalence ratio when up to 30% vol. hydrogen is injected into the natural gas (Nitschke-Kowsky 2012).

Knowledge on change of the ionization current with modification of the fuel composition needs to be further improved and remains at this stage insufficient for the application to a combustion monitoring system. This has motivated the analysis conducted in the next chapter to help understanding the evolution of the ionization current with various factors, including the probe position, gas flow velocity, fuel blend composition and equivalence ratio. Another objective is to identify the key macroscopic parameters controlling these evolutions.

Chapter 8

Experiments on flame ionization current

This chapter presents the experiments conducted on the flame ionization current. They aim at understanding how the current intensity changes with the probe position within the flame, the flow velocity at the burner outlet, the mixture equivalence ratio and fuel blend composition. These investigations are necessary for the design of a flame monitoring system based on the ionization current signal. A coupled equivalence ratio sensing strategy is then developed employing both the ionization current and chemiluminescence. Finally, it shown that results obtained for the ionization current are mainly related to the size of the dead space between flame base and the burner rim.

8.1 Change of ionization current with various parameters

It is first interesting to know whether a universal calibration procedure can be used with a ionization probe set at different positions within the flame. Domestic gas boilers generally operates with varying loads and Kiefer et al. (2012) have shown a power dependence of the ionization signal. Effects of the gas flow velocity on the ionization current need thus to be further understood. Assessing the changes of the ionization current with variations of the gas composition is the main target with the objective to develop a combustion monitoring system. The impact of the equivalence ratio and effects of secondary components in the fuel blend need to be understood for the evaluation of the detection system robustness.

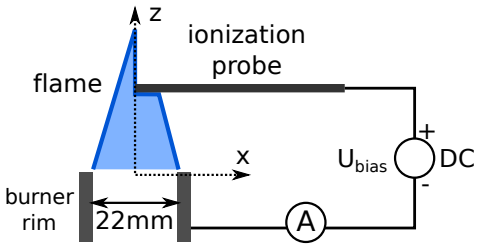

Figure 8.1: *Experimental setup for the flame ionization current measurements.*

8.1.1 Experimental setup

These experiments are conducted with the conical flame burner. The configuration shown in Fig. 8.1 with an electrode in contact with the flame front mimics the situation in a real gas boiler, but with a simplified geometry. A cylindrical probe (2 mm diameter) is installed horizontally above the burner exit. The position of the probe tip is specified in the following by the coordinates (x, z) as shown in Fig. 8.1. A continuous high bias voltage U_{bias} is applied between the probe and the burner nozzle. The metallic burner serves always as the cathode in order to achieve a strong current signal. It has been shown that the contact area between the flame and the cathode is the major bottleneck of ionization current, as the current in this region is driven by cations with a much lower mobility than free electrons (Kiefer et al. 2012; Franke 2002). The multimeter used to measure the ionization current gives intensity values in μA with 2 decimal places yet generally only the first is reliable. Once stabilized, current intensity fluctuations remain within $\pm 0.1\,\mu A$.

8.1.2 Ionization current at different probe positions

The ionization current measured for different positions of the probe tip within the flow is mapped in Fig. 8.2. The colormap indicates the measured current intensity. The flame front position is also indicated in the figure to ease the interpretation of the data. The ionization probe is inserted from the right and stays horizontal throughout the experiment.

Several observations can be made. When the probe is in contact with, or very close to the flame front, the current intensity remains almost constant at all probe positions investigated. Technically, the flame is still separated from the probe by a quenching distance. In this case, the conical flame shape is deformed by the probe due to the obstruction of gas flow by the electrode. The surface area of the contact between the probe and the reaction layer also varies when the probe is moved inside the flow. These modifications do not lead to significant

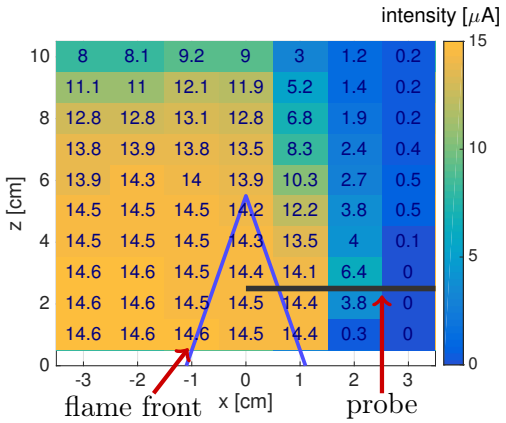

Figure 8.2: *Ionization current as a function of probe tip position within the flow. Methane - air flame,* $u = 1.5\,\mathrm{m/s}$, $\phi = 0.83$, $U_{bias} = 300\,\mathrm{V}$. *The color map indicates the bias current intensity.*

differences on the recorded ionization current signal. A slight increase of signal could eventually be observed when the probe crosses entirely the flame, with the probe tip in the lower left region in Fig. 8.2. These observations are in agreement with Franke (2002). The ionization current is found to be insensitive to the contact area with the anode.

When the probe is moved further away on the right while staying within the burnt gas region, a decrease of the bias current is observed (green and blue zones) in Fig. 8.2. The conductivity of the burnt gases seemingly results from the residual anions and electrons in the post-chemiluminescence region shown in Fig. 7.2 (Goodings et al. 1979b). For the lean conditions explored ($\phi = 0.83$), part of the free electrons are attached to residual oxygen in the burnt gases. In addition, when the distance to the flame front increases, the influence of the surrounding air also becomes stronger leading both to cooling and electron attachment.

The ionization current signal finally drops to zero in Fig. 8.2 when the probe is taken away from the burnt gas region.

8.1.3 Impact of the gas velocity

Figure 8.3.a gives the evolution of the ionization current with the gas velocity (flame power) for experiments carried out at the equivalence ratio $\phi = 0.83$. The ionization current is plotted at three probe tip locations at $x = 0\,\mathrm{cm}$, $z = 2$, 5 and 8 cm. These data show different trends with respect to the gas velocity. This is due to the simultaneous impact of two factors *i.e.* the gas velocity and

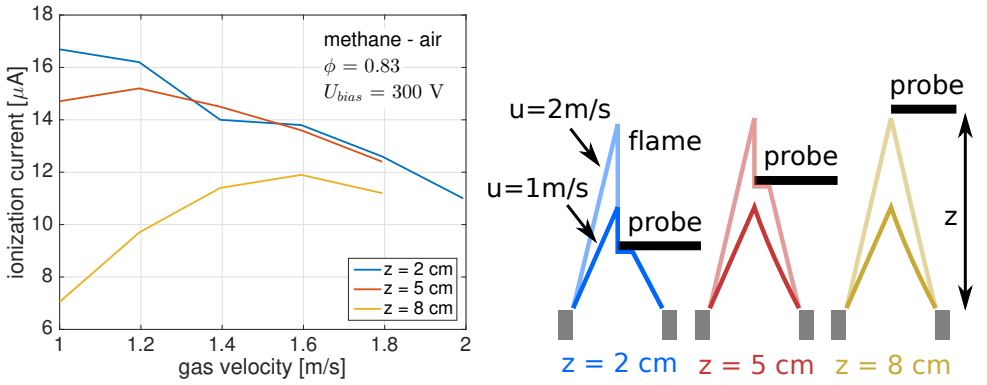

(a) Ionization current *vs.* gas velocity

(b) Indicative flame topology with different gas velocities and probe positions

Figure 8.3: *Evolution of the ionization current with the gas velocity.*

the probe-flame distance.

This phenomenon is schematically illustrated in Fig. 8.3.b. At $z = 2\,\text{cm}$ (blue curve in Fig. 8.3.a), the probe is in contact with the flame over the whole range of bulk flow velocities explored. The ionization current decreases in this case monotonically when the gas velocity increases. At $z = 5\,\text{cm}$ (red curve), the probe is located in the burnt gas region at minimum power. When the gas velocity increases from u_0=1 to 1.2 m/s, the flame gets longer and the distance between the flame tip and the rod is reduced. The bias ionization current is therefore enhanced. Once the flame reaches the probe for a bulk flow velocity $u = 1.4\,\text{m/s}$, it has been shown that the probe position is no longer important. In this case, the red curve joins the blue one obtained at $z = 2\,\text{cm}$. A similar trend is seen for the data gathered at $z = 8\,\text{cm}$ (yellow curve), but the maximum current is achieved in this case at a higher gas velocity.

Despite the different trends observed for the signals in Fig. 8.3 due to the combined effects of the probe position with respect to the flame front and the gas velocity, the three curves indicate that, when the probe is in contact with the flame front, the ionization current decreases for increasing gas velocities. The reason is discussed below in Section 8.3. It is also worth mentioning that the same type of evolution, with a maximum current at medium power, is also observed in real gas boilers as well as in Fig. 7.8.b from Kiefer et al. (2012).

8.1.4 Impact of the fuel composition

A similar approach as in Section 4.1 is adopted to evaluate the effects of the fuel composition on the ionization current. In a first series of tests, the secondary

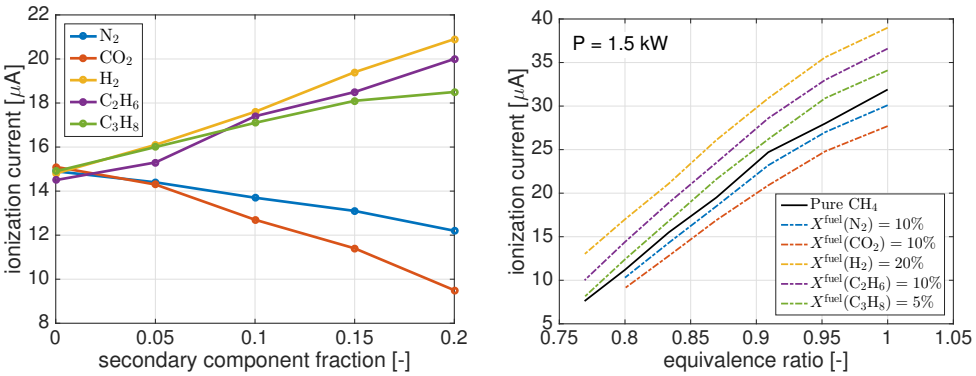

(a) Ionization current *vs.* secondary component fraction ($P = 1.5\,\text{kW}$, $\phi = 0.83$)

(b) Ionization current *vs.* equivalence ratio with different fuel scenarios ($P = 1.5\,\text{kW}$)

Figure 8.4: *Effects of secondary natural gas components on the ionization current.*

components N_2, CO_2, H_2, C_2H_6, C_3H_8 are progressively added to methane from $X^{\text{fuel}} = 0$ to 20% vol., while the power and equivalence ratio are kept constant. In a second series of tests, the ionization current is determined as a function of the equivalence ratio. These data are recorded for pure methane and binary fuel blends as listed in Tab. 4.3 (upper part) to test the possibility to use the ionization current as an equivalence ratio indicator.

Dilution by N_2 and CO_2 causes in Fig. 8.4.a a decrease of the ionization current, while the other components cause an increase of this current. The changes caused by CO_2, H_2, C_2H_6 and C_3H_8 are in absolute value similar, while the impact of N_2 is slightly weaker.

The current is plotted in Fig. 8.4.b as a function of the equivalence ratio for the fuel scenarios listed in Tab. 4.3. It is worth recalling that the ionization current depends on the gas velocity and the curves in Fig. 8.4 are only valid for the given power. All the secondary components cause a drift of the data from the ones obtained with pure methane. But the gaps remain relatively small. The errors made in sensing the equivalence ratio with the bias ionization current remain moderate. The maximum difference is observed for 20% vol. H_2 addition, with a shift of $\Delta\phi = 0.08$ for the same flame ionization current achieved with pure methane at $\phi = 1.0$. The error is the largest when approaching stoichiometry. In all other cases, differences between the current with and without secondary component in the combustible mixture are relatively small leading to differences in equivalence ratio lower than $\Delta\phi = 0.05$ for $0.80 \leq \phi \leq 1.00$. However, the different magnitudes of error are not so much related to the nature of the secondary component, but depend more on their fraction in the fuel blend.

The error in sensing the equivalence ratio turns out to be non-negligible for

Table 8.1: *Estimated errors $\Delta\phi$ of the predicted equivalence ratio for conical flames with three sensing strategies.*

secondary component	ionization current	chemiluminescence	coupled
$X^{\text{fuel}}(N_2)$=10%	$0.01 - 0.02$ (–)	$0.01 - 0.02$ (+)	~ 0.01
$X^{\text{fuel}}(CO_2)$=10%	$0.02 - 0.05$ (–)	$0.01 - 0.02$ (+)	< 0.02
$X^{\text{fuel}}(H_2)$=20%	$0.05 - 0.08$ (+)	~ 0.05 (–)	~ 0.01
$X^{\text{fuel}}(C_2H_6)$=10%	$0.02 - 0.05$ (+)	$0.1 - 0.15$ (+)	~ 0.05 (+)
$X^{\text{fuel}}(C_3H_8)$=5%	$0.01 - 0.03$ (+)	$0.1 - 0.15$ (+)	$0.05 - 0.1$ (+)

combustible mixtures with high secondary component fractions. A new sensing strategy is proposed in the following section combining the ionization current and the flame chemiluminescence as an attempt to reduce the uncertainty in the equivalence ratio determination.

8.2 Coupled equivalence ratio sensing strategy

Figure 4.3 obtained for the CH^*/OH^* ratio and Fig. 8.4.b obtained for the ionization current as a function of the equivalence ratio show the drift of the signal caused by secondary natural gas components. The estimated bias errors of the predicted equivalence ratio values with these two techniques are synthesized in Tab. 8.1 for the five gas composition scenarios conducted with the conical flame burner. The + sign in the parentheses means that the predicted equivalence ratio is higher than the real value and vice versa.

Since the flame ionization current and chemiluminescence signal are two independent parameters, a sensing strategy can be conceived coupling both techniques. The product of the ionization current and CH^*/OH^* chemiluminescence intensity ratio is used in Fig. 8.5 as an equivalence ratio indicator. The results obtained with this new indicator for N_2, CO_2 and H_2 in the fuel blend lie all very close to the reference curve obtained for pure CH_4. Nevertheless, the results for C_2H_6 and C_3H_8 addition still show relatively large gaps with respect to the reference case.

Estimations of the errors made with the coupled sensing strategy are listed in Tab. 8.1. The coupled strategy is especially advantageous in the case of H_2 injection, with a much smaller drift than the two other techniques. The ionization current and chemiluminescence signals cause indeed bias errors in different directions, which are then neutralized by taking the product of the two signals. On the other hand, addition of C_2H_6 and C_3H_8 cause drifts in the same direction for the two techniques, hence the coupled strategy does not

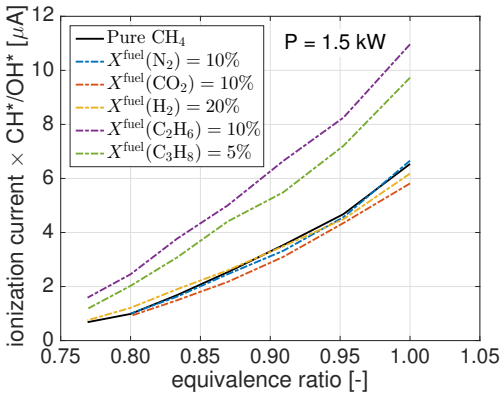

Figure 8.5: *Ionization current × CH*/OH* vs. equivalence ratio for the different fuel composition scenarios listed in Tab. 4.3.*

help to reduce the error. It is also worth reminding that the ionization current depends on the gas flow velocity meaning that each calibration curve as in Fig. 8.5 is also specific to a fixed power level (gas velocity).

Measurements of the ionization current have not been conducted with the cylindrical multi-perforated burner and the validity of the coupled sensing strategy needs to be assessed on this burner. Cautions are needed when extrapolating the results from the conical flame burner to the cylindrical multi-perforated burner due to the various disturbing factors, such as the flame-burner heat exchange, which are absent in the conical flame setup.

8.3 Correlation between ionization current and dead space size

It has been emphasized in the literature review in Section 7.2 that, when a bias voltage is applied to a flame front, the drop of the electrical potential takes place essentially near the cathode. The region near the cathode constitutes a huge electrical resistance, which is the major bottleneck limiting the current intensity. It has also been demonstrated that the ionization current intensity is linked to the quenching distance between the flame and the negatively charged electrode, which is the metallic burner rim in the experiments conducted in this work.

In this section, these properties are investigated with the conical flame configuration shown in Fig. 8.1. The flame-cathode voltage is first measured. Then the ionization current intensity is correlated to the size of dead space between the flame and burner rim. This correlation is used to interpret the evolution

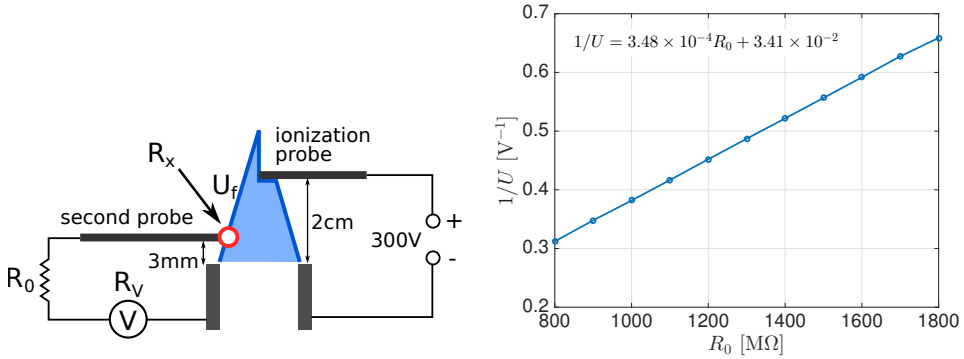

(a) Configuration (b) $1/U$ vs. R_0

Figure 8.6: *Flame front electrical potential measurement.*

of the ionization current when the flame parameters are varied in light of the results found in Section 8.1.

8.3.1 Measurement of flame-cathode voltage

The electrical potential of the flame front can be measured with a second probe with the setup shown in Fig. 8.6. The probe is set at a height of about 3 mm above the burner outlet. One difficulty is that the inter-space between the flame and the probe also constitutes a huge resistance of the order of 100 MΩ. This resistance is much higher than the input impedance of usual voltmeters, typically of the order of 10 MΩ. The voltage therefore cannot directly be inferred from the voltmeter readout.

Rodrigues (2005) made these measurements with an amplifier featuring an input impedance of $10^{12}\,\Omega$. An alternative method is used in this work. As shown in Fig. 8.6.a, another resistor R_0 is added in series with the voltmeter. The voltmeter readout U is recorded for different values of R_0 and the data $1/U$ are plotted as a function of R_0. These quantities are linked by:

$$\frac{1}{U} = \frac{1}{R_v U_f} R_0 + \frac{R_v + R_x}{R_v U_f} \tag{8.1}$$

where R_v is the voltmeter impedance, R_x the unknown resistance between the flame and probe. The voltage U_f between the flame and the burner rim is deduced from the slope of the linear regression of the data.

Measurements are made with a methane-air flame at $P = 1.5\,\text{kW}$ and $\phi = 0.83$. The voltage generator is set at U_{bias}=300 V ($\pm 0.1\%$). The values for the resistance R_0 range between 800 MΩ and 1.8 GΩ. These high resistance

Table 8.2: *Flame-cathode voltage U_f for a bias voltage $U_{\text{bias}} = 300\,\text{V}$ and different operating conditions of the conical flame burner.*

P [kW]	ϕ	Fuel	X^{fuel}	U_f [V]
1.5	1.00	CH_4		298
1.5	0.95	CH_4		298
1.5	0.91	CH_4		295
1.5	0.87	CH_4		289
1.5	0.83	CH_4		285
1.5	0.80	CH_4		284
1.0	0.83	CH_4		282
1.8	0.83	CH_4		282
1.5	0.83	CH_4/CO_2	$X^{\text{fuel}}(CO_2) = 0.2$	286
1.5	0.83	CH_4/H_2	$X^{\text{fuel}}(H_2) = 0.2$	281
1.5	0.83	CH_4/C_3H_8	$X^{\text{fuel}}(C_3H_8) = 0.1$	288
1.5	0.83	CH_4/C_3H_8	$X^{\text{fuel}}(C_3H_8) = 0.2$	290
1.5	0.83	C_3H_8	$X^{\text{fuel}}(C_3H_8) = 1$	298

values ensure that the measurement branch do not perturb the initial electrical circuit, and that the variations of the flame probe resistance R_x are negligible. The voltmeter impedance R_v is about 10.1 MΩ in the corresponding range (1 mV-4 V). The uncertainties for R_0 and R_v values are below 1%.

Figure 8.6.b plotting $1/U$ as a function of R_0 shows a very good linearity. The linear regression gives $U_f = 285\,\text{V}$ and $R_x \sim 90\,\text{M}\Omega$. Repetitive tests with the same operating conditions yield a relative uncertainty of about ±0.5%. Comparing U_f with U_{bias} =300 V at the voltage source, it is confirmed that the major electrical potential drop takes place near the cathode. Therefore the flame properties near the cathode mainly determine the ionization current. This feature also explains why the ionization current is relatively insensitive to the position of the ionization probe (anode) within the flow (see Fig. 8.2). Additional measurements with different flame conditions are listed in Tab. 8.2. When the equivalence ratio gets close to stoichiometry, the flame-cathode voltage U_f further approaches U_{bias} =300 V. This observation may be due to a reduced electron attachment to O_2, which further reduces the resistance near the anode.

CO_2 dilution and H_2 enrichment up to $X^{\text{fuel}} = 20\%$ do not cause significant changes of the flame-cathode voltage U_f. C_3H_8 enrichment is found to increase the voltage U_f, which gets close to the bias voltage U_{bias} when the fuel is switched to pure C_3H_8. Nevertheless, the differences observed for the flame-cathode voltage U_f remain below 20 V for a bias voltage of U_{bias} =300 V and all the operating conditions explored in Tab. 8.2.

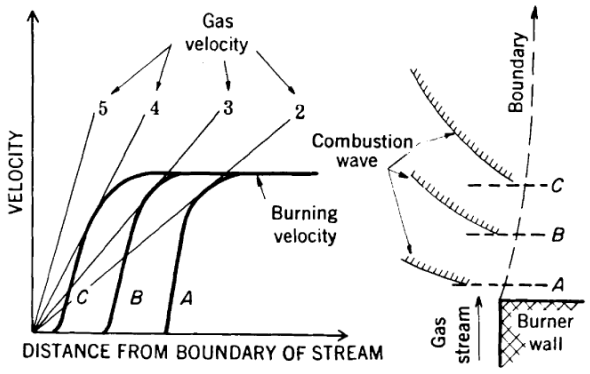

Figure 8.7: *Schematic illustration of a premixed flame stabilization above a burner tube (Lewis and von Elbe 1987).*

8.3.2 Ionization current *vs.* dead space size

Conical flames are stabilized at a finite distance from the burner rim, denoted as flame standoff distance. The combustion reaction in this region is quenched due to the heat loss to the solid wall (Daniel 1957; Popp and Baum 1997). This dead space is associated with the huge resistance near the cathode and its size can be related to the ionization current.

Former studies have shown that the flame standoff distance δ_q increases as the equivalence ratio of methane/air flames is reduced or the gas flow rate is increased (see among others Cullen 1950; Kedia 2010; Altendorfner et al. 2011). These changes can be understood with Fig. 8.7 taken from Lewis and von Elbe (1987). The distributions of both the gas velocity and the laminar burning velocity are not uniform in the vicinity of the burner wall (Lacour 2006). On the one hand, the velocity in the boundary layer increases roughly linearly with the distance to the wall. On the other hand, the flame is quenched near the burner wall and the burning velocity increases with the distance from the wall, in both radial and axial (downstream) directions, thanks to a reduced heat loss, until its adiabatic value is achieved. The flame base is stabilized at the tangent point of the profiles of the burning velocity (bold line in Fig. 8.7) and of the gas velocity (thin line in Fig. 8.7). When the adiabatic laminar burning velocity is reduced or when the gas velocity is increased, in order to maintain the equilibrium, the stabilization point has to shift downstream (from A towards C in Fig. 8.7) to enhance the burning velocity by reducing the heat loss. It leads then to a larger flame standoff distance.

In this work, the flame standoff distance is measured with an ICCD camera (Princeton Instrument, PI-Max, 512×512 pixels) equipped with a Nikkor 105 mm F/2.8 lens. The setup allows for a zoom of a tiny zone near the flame

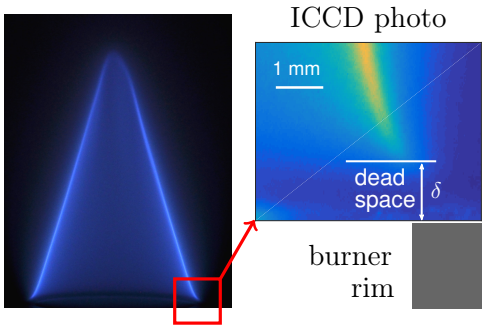

Figure 8.8: *Dead space between flame base and burner rim.*

Table 8.3: *Flame standoff distance δ at different operating conditions of the conical flame burner, measured from ICCD photos. The uncertainty is estimated to be* ±2 pixel *or* ±0.05 mm. *Original images for the determination of δ are provided in Appendix B.*

P [kW]	ϕ	Fuel	X^{fuel}	δ [mm]
1.5	1.00	CH_4		0.58
	0.91			0.61
	0.83			0.80
	0.77			1.38
1	0.83	CH_4		0.63
1.4				0.80
1.8				1.07
1.5	0.83	CH_4/CO_2	$X^{\text{fuel}}(CO_2) = 0.1$	1.04
			$X^{\text{fuel}}(CO_2) = 0.2$	1.26
1.5	0.83	CH_4/H_2	$X^{\text{fuel}}(H_2) = 0.1$	0.68
			$X^{\text{fuel}}(H_2) = 0.2$	0.56
1.5	0.83	CH_4/C_3H_8	$X^{\text{fuel}}(C_3H_8) = 0.1$	0.80
			$X^{\text{fuel}}(C_3H_8) = 0.2$	0.80

base as shown in Fig. 8.8. The ICCD images obtained for different equivalence ratios, gas velocities (flame powers) and fuel compositions are provided in Appendix B. The position of the flame base is determined by setting a threshold of 25% of the maximum intensity. The uncertainty is estimated to be ±2 pixel or ±0.05 mm.

The measured flame standoff distances at different operating conditions are listed in Tab. 8.3. This distance increases with the gas velocity (flame power) or CO_2 dilution, and decreases with H_2 enrichment or when the equivalence ratio approaches the stoichiometry, yet remains constant with C_3H_8 enrichment at fixed power. To synthesize these change, a higher bulk gas velocity u_0 or a lower adiabatic laminar burning velocity S_L causes the standoff distance to increase. It is coherent with the above analysis made for Fig. 8.7.

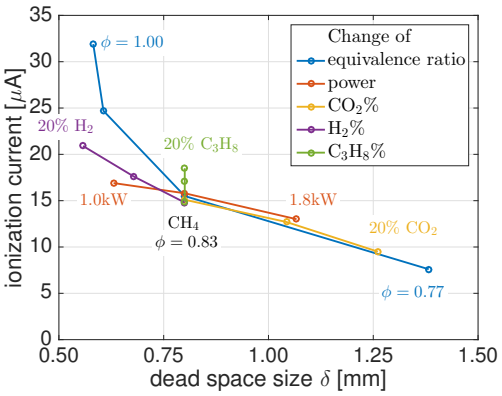

Figure 8.9: *Ionization current vs. dead space height. The flow operating conditions are listed in Tab. 8.3.*

The corresponding ionization current is then plotted as a function of the dead space height in Fig. 8.9. A low ionization current is almost always related to a large dead space. These two quantities are well correlated when the power, equivalence ratio ($\phi \leq 0.83$ or $\delta > 1.5\,\mathrm{mm}$), the H_2 or CO_2 molar fraction in the mixture blend are varied, meaning that the effect of dead space size is dominant. These results are found to be weakly altered by the choice of the intensity threshold level for the determination of the standoff distance in the images when the threshold is chosen between 15% and 40% of the maximum intensity.

Deviations are observed in Fig. 8.9 when the equivalence ratio gets closer to stoichiometry (blue line towards the left). Also, injection of C_3H_8 barely modifies the dead space size while the ionization current increases. These deviations result from factors that were neglected in this study, such as the populations of ions and the detailed electrical field near the cathode. Nevertheless, this correlation between the ionization current intensity and the size of dead space allows to interpret the main features of the evolution of the ionization current with the different flame parameters tested. It also qualitatively provides an experimental support for the theoretical analyses from Karrer (2009) and Rodrigues (2005).

It is now interesting to examine whether Eq. 7.7 proposed by Karrer et al. (2010) may be used to estimate the ionization current intensity measured in these experiments. An attempt is made for a methane-air flame with $P = 1.5\,\mathrm{kW}$ and $\phi = 0.83$ and several rough approximations. It is hypothesized that the current near cathode is sustained by H_3O^+ ion with a mobility of $\mu_i \sim 3 \times 10^{-4}\,\mathrm{m^2\,V^{-1}\,s^{-1}}$ (Karrer 2009). Also the contact area between the flame and the burner rim corresponds to the burner tip area $A = \pi D_i \Delta R = 2 \times 10^{-4}\,\mathrm{m^2}$ where $D_i = 22\,\mathrm{mm}$ is the internal diameter of the nozzle and

$\Delta R = 3\,\text{mm}$ the thickness of the metal. The dead space size $\delta = 0.8\,\text{mm}$ and the flame-cathode voltage $U_f = 285\,\text{V}$ are taken from the measurements. By taking a permittivity $\epsilon = 9 \times 10^{-12}\,\text{F m}^{-1}$, the resulting ionization current estimated with Eq. 7.7 leads to:

$$I_{ion} = A\frac{9\mu_i\epsilon_0 U_f^2}{8\delta^3} \sim 160\,\mu\text{A} \tag{8.2}$$

This estimate is one order of magnitude bigger than the experimental value $15\,\mu\text{A}$ that was measured, but needs to be taken with caution due to the very rough approximations made in the analysis made. The surface area A for the current density is for example not well known. The values taken for the permittivity and the mobility may also feature large deviations. On the other hand, one may however see that the scaling law $I_{ion} \propto \delta^{-3}$ is not reproduced in Fig. 8.9. The ionization current intensity does not drop so quickly with the dead space size in the experiments conducted in this work.

Conclusion

The experiments carried out in this chapter reveal that the ionization current across a conical flame changes when the inlet gas velocity, the fuel composition and the mixture equivalence ratio are modified. This current barely changes with the probe position when the latter is in contact with the flame front, but is progressively reduced when the probe is moved away from the flame.

The ionization current is not a function of the equivalence ratio only, but also depend on the flame power. The current intensity is also subject to changes of the natural gas composition, which leads to errors of the predicted equivalence ratio when the ionization current response from methane/air mixtures is used to infer the equivalence ratio of a methane/air blend with secondary components.

A new equivalence ratio sensing strategy coupling both the ionization current and the CH^*/OH^* ratio has been developed. This new indicator considerably reduces the error with H_2 injection in the fuel blend, compared to the use of either techniques alone to detect the equivalence ratio. However, it cannot be used with C_3H_8 and C_2H_6 natural gas blends.

Finally, a set of experiments has been conducted to infer the main parameters controlling the ionization current intensity. It has been found that it is mainly related to the flame standoff distance at the cathode, which leads to the largest resistance in the electrical circuit. These quantities have been determined and the correlation between the ionization current and flame standoff distance is robust when the flame power and fuel composition are varied, including H_2

enrichment and CO_2 dilution. Deviations are observed for nearly stoichiometric mixtures and for C_3H_8 natural gas blends. This correlation helps to interpret the experimental observations.

Part III

Demonstrative control loop

Chapter 9

Chemiluminescence-based equivalence ratio control

This chapter shows a demonstrative system that automatically detects and regulates the equivalence ratio of a methane/air fuel blend with secondary components in a cylindrical multi-perforated burner used in domestic gas boilers. The system exploits the chemiluminescence signal to determine the equivalence ratio of the combustible mixture and serves as a platform to test different sensing strategies. The feasibility and the limitations of the use of flame chemiluminescence as a technique for flame state monitoring are emphasized.

9.1 Equivalence ratio sensing strategies

The demonstrative system is developed for the cylindrical multi-perforated burner used in real domestic gas boilers. Lookup tables are constructed with measurements gathered on methane-air flames. During operation, the equivalence ratio of the unknown combustible mixture is deduced by matching some properties of the chemiluminescence signal with the stored data. Several equivalence ratio sensing strategies are studied based on the results from Chapter 4.

The first strategy is to use the CH^*/OH^* intensity ratio measured by the spectrometer. Ignoring the separation of the curves in Fig. 4.4 for $\phi > 0.8$, the sensing can be realized with one unique calibration curve for different power levels, which simplifies the control algorithm. Nevertheless, errors are expected when approaching stoichiometry as the CH^*/OH^* intensity ratio slightly depend on the flame power in these conditions. Also, the major drawback of this equivalence ratio detection technique is the considerable error made with

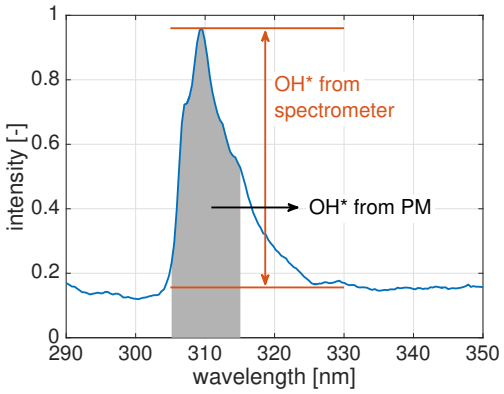

Figure 9.1: *OH* intensity obtained from the spectrometer and the photomultiplier tube.*

combustible mixtures enriched by C_2H_6 and C_3H_8.

A second strategy developed in Section 4.3.3.4 is to use the OH^* intensity alone, with the major advantage of being valid for a wide set of natural gas compositions with secondary components. A series of calibration curves need to be constructed in this case for the different power levels. In practice, however, the flame power is not readily known and can only be determined from the natural gas flow rate and its composition. Instead, the air flow rate is much easier to know and can be used to scale the calibration curves. In domestic gas boilers, the air flow rate is directly related to the speed of the air feeding fan, ignoring atmospheric variations due to changes of temperature and altitude. With this approximation in mind, calibration curves can therefore be generated for different air flow rates, mimicking the situation in real gas boilers.

For these two strategies, the CH^* and OH^* intensities are obtained from the spectrometer. A band-stop optical filter (525-800 nm) is in this case used to attenuate the light originating from thermal radiation of the hot burner solid surfaces. The integration time of the spectrometer can be automatically adjusted with a LabVIEW program so as to achieve the best resolution with a high intensity readout without reaching the saturation limit of the detection sensor. The raw spectrum is then corrected for the dark background signal and the intensity readout nonlinearity as described in Section 2.3.2. The CH^* and OH^* intensities are finally deduced from the peak height above the CO_2^* baseline as illustrated in Fig. 9.1.

An alternative technique is to determine the OH^* signal with a photomultiplier tube mounted with a bandpass optical filter centered at 310 nm. In this case, the resulting intensity results from all the light collected between 305 and 315 nm without the possibility to correct for the CO_2^* emission baseline (see Fig. 9.1).

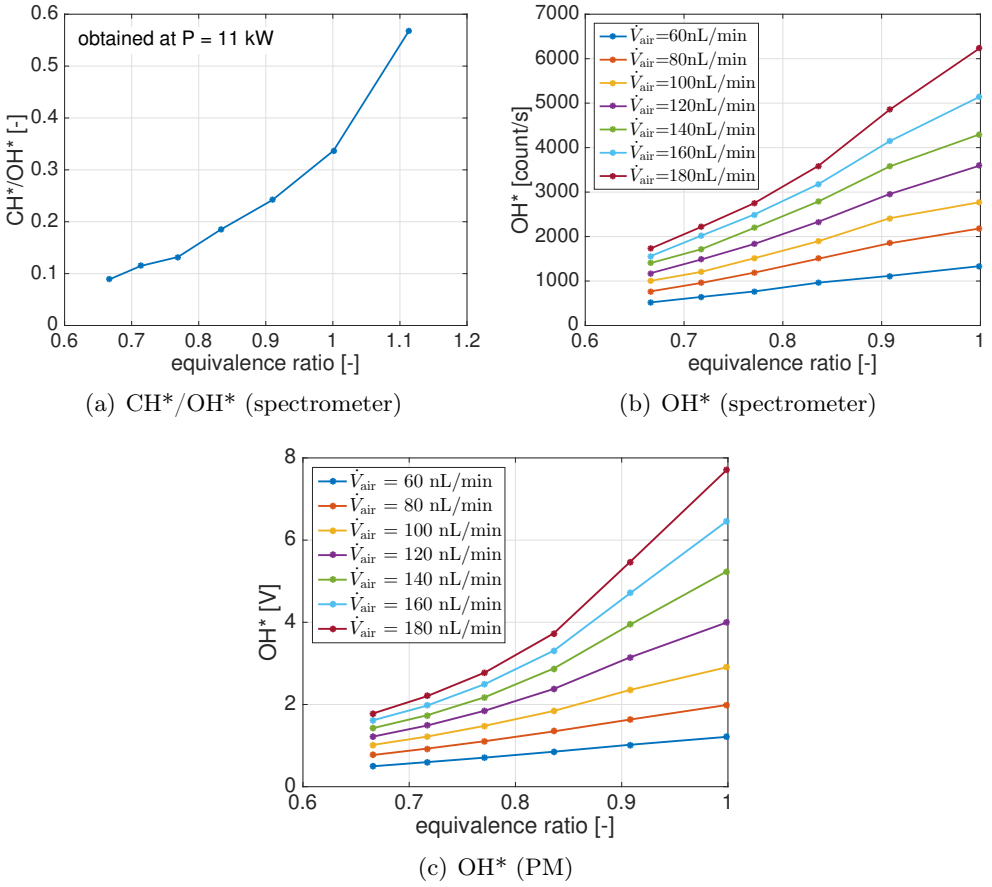

(a) CH*/OH* (spectrometer)

(b) OH* (spectrometer)

(c) OH* (PM)

Figure 9.2: *Calibration curves based on three different chemiluminescence signals.*

In summary, three different techniques are explored in this study. They are based on detecting the:

- CH*/OH* intensity ratio deduced from the spectrometer,
- OH* intensity deduced from the spectrometer,
- OH* intensity determined with the photomultiplier tube mounted with a bandpass optical filter, without correction for the CO_2^* emission.

The corresponding calibration curves obtained with pure methane/air mixtures are plotted in Fig. 9.2. The CH*/OH*-ϕ curve is determined at the power $P = 11\,\text{kW}$ and the same curve is used to determine the equivalence ratio at the other power levels. The OH* curves are constructed for several air flow rates. Their monotonic range is limited to lean operating conditions $\phi < 1$.

For the first strategy with the CH*/OH* intensity ratio, sensing the equivalence

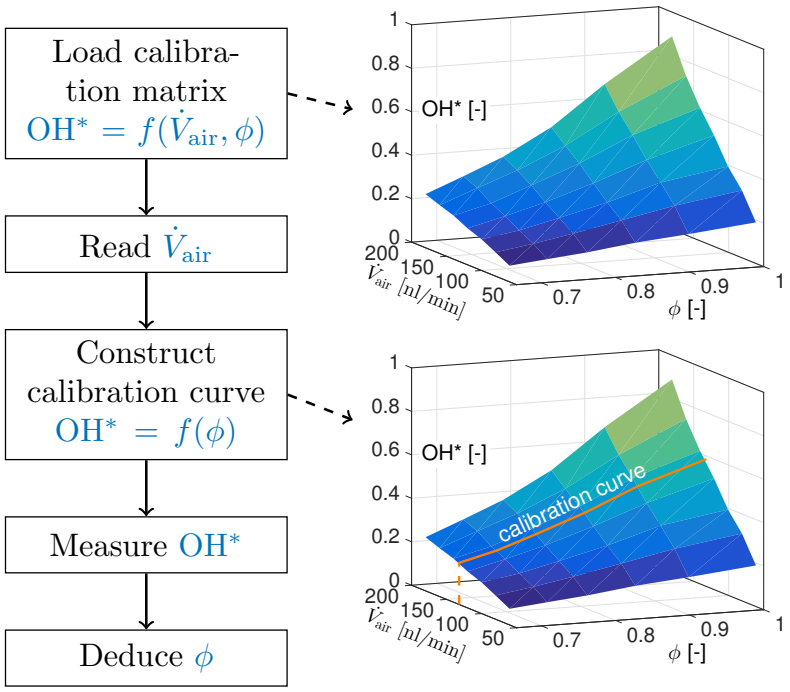

Figure 9.3: *Procedure for equivalence ratio sensing with the OH* intensity.*

is done by linear interpolation between the data. For the two other strategies based on the OH* intensity, the procedure to determine the equivalence ratio is described in Fig. 9.3. A calibration curve is first generated for the specific operating air flow rate with a bicubic interpolation of the OH* data gathered for 6 equivalence ratios and 7 air flow rates. The value of the equivalence ratio of the combustible mixture is then deduced from the measured OH* intensity through a second interpolation.

During operation of the cylindrical multi-perforated burner, it was observed that the OH* signal takes a relatively long time to reach a stable value after a cold start or when the flow operating conditions are modified. A more detailed investigation of this feature is carried out in Section 9.4. Consequently, the OH* signal needs to be recorded only when the signal has reached a stable state. This feature was considered when constructing the lookup table linking the OH* intensity to the equivalence ratio and during operation of the burner.

9.2 Test of sensing strategies

The performances of the equivalence ratio sensing technique with the three different strategies are examined for the flow operating conditions listed below,

for which four equivalence ratios $\phi = 0.67$, 0.74, 0.83, 0.95 were considered:

- Pure methane at $P = 4$ and 7 kW (with additional tests at 10 kW for the CH^*/OH^* strategy).
- Methane diluted with 10% and 20% vol. N_2 at 7 kW.
- Methane diluted with 10% and 50% vol. CO_2 at 7 kW. The 50% vol. CO_2 mimics the raw biogas scenario.
- Methane enriched with 20% vol. H_2 at 7 kW.
- Methane enriched with 5% vol. C_3H_8 at 7 kW.

The results from these experiments are synthesized in Tabs. 9.1-9.3. The sensing is performed when the OH^* signal is stabilized and is repeated 5 times to get an average value and determine a standard deviation. In these tables, ϕ represents the equivalence ratio calculated from the flow rates injected in the system and ϕ' denotes the value determined from the chemiluminescence signal. The quantity SD stands for the standard deviation of ϕ'.

Table 9.1 yields the results when the CH^*/OH^* signal determined from the spectrometer is used to infer the equivalence ratio. The bias error $|\phi' - \phi|$ for the five events reaches up to 0.04 even with a pure methane/air mixture. This is probably due to the fact that the calibration curve is constructed for a higher power of $P = 11$ kW and the flame-burner heat exchange cause deviations at lower operating power as seen in Fig. 4.4. Indeed the error does seem to be reduced at 10 kW. With N_2 and CO_2 dilution the bias errors are of the same order of magnitude. The detection of the equivalence ratio remains acceptably reliable with the raw biogas scenario containing 50% vol. CO_2 in the fuel blend. When the fuel is enriched with H_2, the errors made on the detection of the equivalence ratio are even smaller than for the pure methane case. By comparing Figs. 4.4 and 4.5, it is observed that a low power causes the CH^*/OH^* intensity ratio to rise, while H_2 enrichment causes it to drop. The two effects are then partially canceled out in this case. With C_3H_8 enrichment, the equivalence ratio is largely overestimated as expected. The large bias error of $(\phi' - \phi) \sim 0.15$ makes this equivalence ratio sensing technique difficult for application in a practical system. Another issue concerning the use of the CH^*/OH^* intensity ratio is the relatively large standard deviation found in the measurements as shown in the last column in Tab. 9.1. These fluctuations mainly result from the measurement uncertainties of the CH^* intensity because of its low level.

Table 9.2 shows the results obtained with the equivalence ratio sensing technique based on the OH^* intensity determined from the spectrometer. The

results are much better for pure methane and mild N_2, CO_2 dilutions with bias errors on the equivalence ratio $|\phi' - \phi|$ generally below 0.01. These better results are mainly attributed to the fact that the power is taken into account in the calibration lookup table. However, when the CO_2 dilution rises up to 50% vol., the equivalence ratio becomes largely underestimated, making the results unusable. Bias errors are slightly larger with H_2 enrichment and reach about $(\phi' - \phi) = 0.02$ with 20% vol, which still remains acceptable. With 5% vol. C_3H_8, the bias error is relatively large near stoichiometry ($\phi' - \phi \sim 0.05$) but drops within the acceptable limit at leaner conditions. The measurement uncertainty of the OH^* intensity from the spectrometer is smaller than CH^*/OH^* intensity ratio thanks to the relatively high intensity of the OH^* peak emission.

Table 9.3 shows the sensing results when the OH^* signal is determined with a photomultiplier tube, without correction for the CO_2^* emission background. The bias errors made on the equivalence ratio are close to those found in Tab. 9.2 for the results obtained with the spectrometer. The only main difference is that the bias error with H_2 enrichment goes from positive to negative values, while the absolute value remains of the same order ($|\phi' - \phi| \sim 0.02$). This feature results from the CO_2^* emission baseline, which is reduced by the injection of H_2 in the fuel mixture. The measurement uncertainty is further improved with the photomultiplier tube as compared to the spectrometer.

9.3 Choice of equivalence ratio sensing strategy

According to the above discussions on the results gathered in Tabs. 9.1-9.3, the OH^* signal from photomultiplier tube is the best sensing strategy to detect the equivalence ratio thanks to its excellent performances under various conditions:

- The bias error is very low for pure methane and remains moderate for N_2 and CO_2 dilution at various power levels ($|\phi' - \phi| < 0.01$).
- With H_2 enrichment up to 20% vol., the bias error remains still acceptable ($|\phi' - \phi| < 0.02$).
- With up to 5% vol. C_3H_8, the bias error remains acceptable at the operational equivalence ratio of gas boilers of $\phi \sim 0.8$, although it tends to grow close to the stoichiometry.

From the viewpoint of industrial application to real gas boilers, this strategy also offers several important advantages in addition:

- The measurement with a photomultiplier tube is much faster and much easier than with a spectrometer, while the uncertainty is lower at the same

Table 9.1: *Equivalence ratio sensing results based on the CH^*/OH^* signal deduced from the spectrometer measurements.*

Power [kW]	Secondary component	ϕ real	ϕ' detected	$(\phi' - \phi)$ $\times 10^3$	$(\phi' - \phi)/\phi$ $\times 100\%$	SD $\times 10^3$
4.0	(pure CH_4)	0.956	0.954	-2	-0.2%	17
		0.836	0.838	2	0.2%	9
		0.742	0.781	39	5.3%	10
		0.668	0.685	17	2.5%	9
7.0	(pure CH_4)	0.952	0.976	24	2.5%	5
		0.833	0.854	21	2.6%	7
		0.740	0.781	41	5.6%	15
		0.666	0.661	-5	-0.7%	8
10.0	(pure CH_4)	0.952	0.975	23	2.4%	3
		0.835	0.840	5	0.6%	6
		0.742	0.754	12	1.6%	15
		0.667	0.668	1	0.1%	5
7.0	$X^{\text{fuel}}(N_2) = 10\%$	0.952	0.992	40	4.2%	4
		0.833	0.865	32	3.8%	4
		0.740	0.776	36	4.9%	11
		0.666	0.667	1	0.2%	7
7.0	$X^{\text{fuel}}(N_2) = 20\%$	0.952	0.990	38	4.0%	7
		0.833	0.860	27	3.3%	6
		0.740	0.766	26	3.5%	17
		0.666	0.662	-4	-0.5%	6
7.0	$X^{\text{fuel}}(CO_2) = 10\%$	0.952	0.977	25	2.6%	4
		0.833	0.852	19	2.3%	6
		0.740	0.766	26	3.5%	15
		0.666	0.657	-9	-1.4%	9
7.0	$X^{\text{fuel}}(CO_2) = 50\%$	0.952	0.988	36	3.8%	3
		0.833	0.841	8	1.0%	8
		0.740	0.772	32	4.3%	7
		0.666	0.682	16	2.5%	8
7.0	$X^{\text{fuel}}(H_2) = 20\%$	0.951	0.952	1	0.1%	18
		0.833	0.831	-2	-0.2%	5
		0.741	0.743	2	0.2%	16
		0.666	0.651	-15	-2.2%	5
7.0	$X^{\text{fuel}}(C_3H_8) = 5\%$	0.951	1.058	107	11.3%	4
		0.832	0.992	160	19.2%	5
		0.739	0.895	156	21.1%	3
		0.665	0.818	153	23.0%	9

Table 9.2: *Equivalence ratio sensing results based on the OH* signal deduced from the spectrometer measurements.*

Power [kW]	Secondary component	ϕ real	ϕ' detected	$(\phi' - \phi)$ $\times 10^3$	$(\phi' - \phi)/\phi$ $\times 100\%$	SD $\times 10^3$
4.0	(pure CH_4)	0.956	0.958	2	0.2%	5
		0.836	0.836	0	0.0%	6
		0.742	0.745	3	0.4%	3
		0.668	0.660	-8	-1.2%	5
7.0	(pure CH_4)	0.952	0.958	6	0.6%	4
		0.833	0.836	3	0.4%	4
		0.740	0.743	3	0.5%	3
		0.666	0.662	-4	-0.6%	2
7.0	$X^{\text{fuel}}(N_2) = 10\%$	0.952	0.955	3	0.4%	7
		0.833	0.835	2	0.2%	2
		0.740	0.745	5	0.6%	1
		0.666	0.660	-6	-0.9%	0
7.0	$X^{\text{fuel}}(N_2) = 20\%$	0.952	0.945	-7	-0.8%	8
		0.833	0.832	-1	-0.2%	1
		0.740	0.744	4	0.5%	2
		0.666	0.660	-6	-0.9%	1
7.0	$X^{\text{fuel}}(CO_2) = 10\%$	0.952	0.936	-16	-1.7%	4
		0.833	0.829	-4	-0.5%	3
		0.740	0.740	0	0.0%	3
		0.666	0.660	-6	-0.9%	2
7.0	$X^{\text{fuel}}(CO_2) = 50\%$	0.952	0.785	-167	-17.6%	1
		0.833	0.727	-106	-12.7%	4
		0.740	0.663	-77	-10.4%	2
		0.666	0.611	-55	-8.3%	2
7.0	$X^{\text{fuel}}(H_2) = 20\%$	0.941	0.968	27	2.9%	4
		0.823	0.845	22	2.6%	3
		0.731	0.754	23	3.1%	1
		0.658	0.670	12	1.9%	1
7.0	$X^{\text{fuel}}(C_3H_8) = 5\%$	0.951	0.996	45	4.7%	2
		0.832	0.855	23	2.7%	2
		0.739	0.757	18	2.5%	3
		0.665	0.670	5	0.8%	1

Table 9.3: *Equivalence ratio sensing results based on the OH* signal measured by the photomultiplier tube.*

Power [kW]	Secondary component	ϕ real	ϕ' detected	$(\phi' - \phi)$ $\times 10^3$	$(\phi' - \phi)/\phi$ $\times 100\%$	SD $\times 10^3$
4.0	(pure CH_4)	0.956	0.955	-1	-0.1%	1
		0.836	0.836	0	0.0%	1
		0.742	0.745	3	0.4%	1
		0.668	0.667	-1	-0.2%	1
7.0	(pure CH_4)	0.952	0.958	6	0.6%	1
		0.833	0.836	3	0.4%	0
		0.740	0.746	6	0.8%	0
		0.666	0.659	-7	-1.1%	0
7.0	$X^{\text{fuel}}(N_2) = 10\%$	0.952	0.960	8	0.9%	1
		0.833	0.834	1	0.1%	1
		0.740	0.745	5	0.7%	0
		0.666	0.657	-9	-1.4%	0
7.0	$X^{\text{fuel}}(N_2) = 20\%$	0.952	0.947	-5	-0.5%	1
		0.833	0.826	-7	-0.8%	0
		0.740	0.738	-2	-0.2%	1
		0.666	0.653	-13	-1.9%	0
7.0	$X^{\text{fuel}}(CO_2) = 10\%$	0.952	0.935	-17	-1.7%	1
		0.833	0.818	-15	-1.8%	0
		0.740	0.732	-8	-1.1%	0
		0.666	0.647	-19	-2.9%	0
7.0	$X^{\text{fuel}}(CO_2) = 50\%$	0.952	0.853	-99	-10.4%	1
		0.833	0.753	-80	-9.6%	0
		0.740	0.677	-63	-8.5%	0
		0.666	0.606	-60	-9.0%	0
7.0	$X^{\text{fuel}}(H_2) = 20\%$	0.941	0.926	-15	-1.6%	0
		0.823	0.817	-6	-0.7%	1
		0.731	0.731	0	0.0%	0
		0.658	0.644	-14	-2.1%	0
7.0	$X^{\text{fuel}}(C_3H_8) = 5\%$	0.951	0.983	32	3.3%	1
		0.832	0.851	19	2.2%	1
		0.739	0.759	20	2.8%	1
		0.665	0.672	7	1.1%	1

time. The signal level can also easily be amplified with a photomultiplier tube.

- The fact that the OH^* intensity lies in the UV range makes it free from the impact of indoor lighting, even though the sunlight may still needs to be considered. The OH^* intensity is also insensitive to thermal radiation from the hot solid surfaces with light emission covering the visible and IR bands.

- The simplicity of this measurement with only one signal intensity without various correction procedures makes it promising to be realized with low cost alternative sensors.

Nevertheless, several potential risks need to be pointed out before applying this equivalence ratio sensing strategy to real flame monitoring systems:

- The OH^* signal is not a reliable indicator with high CO_2 concentrations in the fuel blend, as for example in the case of raw biogas.

- The validity of this indicator has not been not examined at higher burner loads due to the limitation of the laboratory test bench.

- The OH^* signal may take a long time to stabilize after a cold start or changes of flow operating conditions. This phenomenon is further investigated in Section 9.4.

9.4 Impact of burner temperature on OH^* signal

Due to the large thermal inertia of the metallic components of the boiler, it takes a certain time after ignition for the burner to heat up and reach a steady temperature. This is also the case, though to a less extent, for sudden changes of the flow operating conditions, especially when the power is modified.

Under ideal and stabilized conditions, according to the findings in Section 5.4, the burner temperature is not expected to modify the chemiluminescence intensity. For $u_0/S_L > 1$, the chemiluminescence intensity depends on the inlet gas temperature T_0, but the flame-burner heat exchange should be weak and the burner does not heats up. Consequently the inlet gas does not undergo the preheating process and T_0 is expected to remain close to the atmospheric temperature. For $u_0/S_L < 1$, the chemiluminescence intensity is found to be independent of inlet gas temperature T_0.

However, the observations made on the multi-perforated burner are at variance

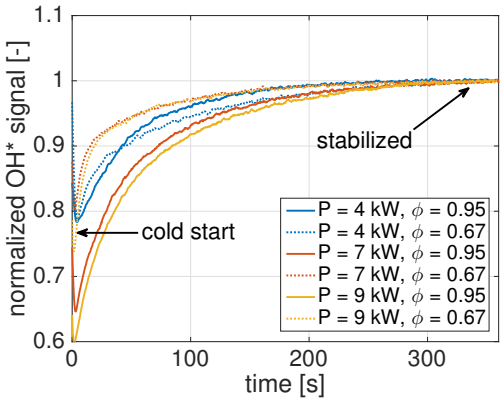

Figure 9.4: *Evolution of the OH* signal measured with a photomultiplier tube over* 6 min *after a cold start of the multi-preforated burner. Intensity values are normalized by the steady state value.*

with this conclusion. In Fig. 9.4, the burner is ignited from a cold condition at different powers varying between $P = 3$, 7 and 9 kW and different equivalence ratios $\phi = 0.67$ and 0.95. The OH* signal from the photomultiplier tube is recorded over a period of 6 minutes and the signal intensities are normalized by the steady state value reached at the end. It can be noticed that the signal intensity during the first instants is only 60%-80% of the final value $I_{\max}$, and this signal progressively approaches the stabilized value with time.

An interpretation of these features is attempted. The contradiction with the ideal case possibly results from the fact some of the flames are stabilized in the non-adiabatic regime and other ones are in the adiabatic regime. The burner is only heated up by those flames which are stabilized in the non-adiabatic regime ($u_0/S_L < 1$), while the other flames in the non-adiabatic regime ($u_0/S_L > 1$) benefit from the hotter reactant stream preheated by the hot burner components to achieve higher chemiluminescence intensities. Under these hypotheses, the OH* intensity increases with the burner temperature. The initially cold quartz tube surrounding the burner may also contribute to this mechanism during the warm up of the whole system. In addition, the conclusions obtained Section 5.4 under steady conditions may not be applicable to the transitional regime

A rough estimation of the time necessary to achieve 90%, 95% and 98% of $I_{\max}$ is given in Tab. 9.4. The resulting bias errors on the equivalence ratio are also reported in this table. They are estimated from the slope of the curves plotted in Fig. 9.2. This causes a difficulty to detect the correct equivalence ratio during the warm up of the burner and during transition to another operating conditions.

Table 9.4: *Time necessary for the OH* signal intensity to achieve 90%, 95% and 98% of the steady state value $I_{\max}$ after a cold start. An estimate of the resulting bias errors on the predicted equivalence ratio is given in the last row.*

Power	ϕ	90% $I_{\max}$	95% $I_{\max}$	98% $I_{\max}$
4.0 kW	0.95	45 s	80 s	140 s
4.0 kW	0.67	45 s	110 s	200 s
7.0 kW	0.95	70 s	125 s	200 s
7.0 kW	0.67	15 s	60 s	130 s
9.0 kW	0.95	85 s	150 s	220 s
9.0 kW	0.67	15 s	60 s	130 s
Bias error $(\phi' - \phi)$		~ -0.05	~ -0.03	~ -0.01

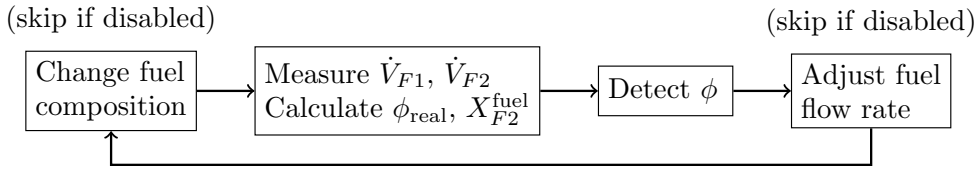

Figure 9.5: *Chart of the equivalence ratio control loop.*

9.5 Equivalence ratio control loop

A demonstrative equivalence ratio control system is now developed. The equivalence ratio is detected with the help of the OH* intensity recorded by the photomultiplier tube. The system uses three Bronkhorst mass flow meters controlled with a LabVIEW program. They allow to change separately the air, methane and another secondary component mass flow rates. They are for convenience designated in the following by AIR, F1 and F2 respectively.

Figure 9.5 shows a simplified chart of the control loop. More details are found in the block diagram in Fig. C.2, together with the corresponding LabVIEW front panel in Fig. C.1 in Appendix C. Each iteration of the loop is a four-step sequence:

- The first step is used to set the fuel composition according to the required secondary component volumetric molar fraction X_{F2}^{fuel} in the fuel blend. A button in the front panel gives a boolean signal which decides whether this step is executed or not. The global volumetric flow rate is kept constant in this process. It mimics the situation of gas composition variations in a real gas boiler, ignoring nevertheless changes of flow rates due to a different gas density considering Bernoulli's equation. The set values for

the flow meters F1 and F2 are calculated from the current value:

$$\dot{V}'_{F1} = (\dot{V}_{F1} + \dot{V}_{F2})(1 - X_{F2}^{\text{fuel}})$$
$$\dot{V}'_{F2} = (\dot{V}_{F2} + \dot{V}_{F2})X_{F2}^{\text{fuel}}$$

After sending the set values to the flow rate controllers, the program is forced to wait 2 seconds to let the flow controllers to reach the desired flow rates by changing the opening of their integrated valves.

- In the second step, the flow rates of methane $\dot{V}_{\text{F1}}$ and secondary component $\dot{V}_{\text{F2}}$ are read from the flow meters. The secondary component molar fraction $X_{\text{F2}}^{\text{fuel}}$ is calculated to check the desired value.

- In the third step, the equivalence ratio is deduced from the OH* signal according to the procedure shown in Fig. 9.3. The air flow rate needed for this calculation is read from the air flow meter. The real equivalence ratio ϕ_{real} is determined at this step based on the indications of the mass flow meters.

- The fourth step, executed when approved by clicking a button in the front panel of the LabVIEW program, serves to regulate the global fuel flow rate and the fuel composition is kept constant. The fuel flow rate is adjusted with the ratio of the detected equivalence ratio to the set value as:

$$\dot{V}'_{F1} = \dot{V}_{F1}\frac{\phi_{\text{set}}}{\phi_{\text{detected}}}$$
$$\dot{V}'_{F2} = \dot{V}_{F2}\frac{\phi_{\text{set}}}{\phi_{\text{detected}}}$$

A waiting time of 1 second is forced after sending the set points to the flow meters.

9.6 Validation of the control loop

The control loop validation is first tested with pure methane by changing the set value of equivalence ratio at two different powers $P = 4$ and 7 kW. Results are shown in Fig. 9.6. The initial operating point of the burner is set to an equivalence ratio $\phi = 0.80$. Automatic fuel flow rate regulation is started at the beginning and corresponds to the green dotted line with arbitrary scale. The set point of the equivalence ratio is then switched back and forth between $\phi = 0.80$ and $\phi = 0.75$. The real equivalence ratio (yellow line), calculated from the flow rates, is shown to follow the set value (blue line), with a small difference of $|\Delta\phi| \sim 0.01$.

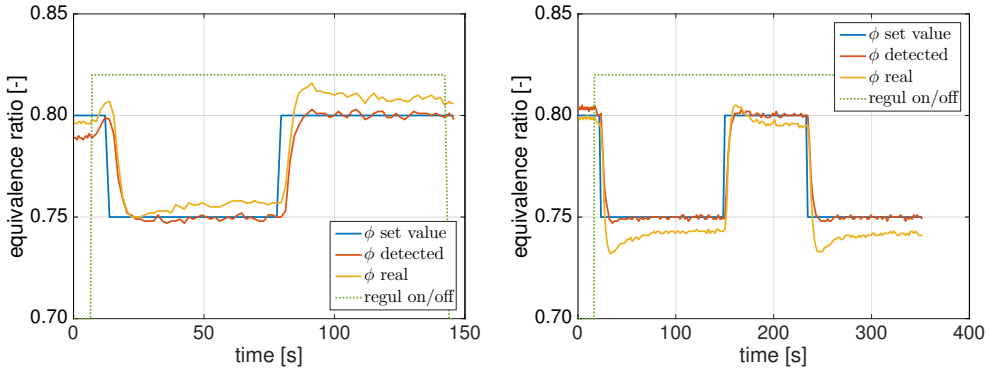

(a) P=4 kW (b) P=7 kW

Figure 9.6: *Tests of the control loop with methane/air mixtures at two different operating powers by changing the equivalence ratio set value. Automatic fuel flow rate regulation (green dotted line with arbitrary scale) is permanently enabled.*

A series of tests are then made with the following scenarios of binary fuel blends. Some of them are chosen in accordance with reference gases used for gas boiler certification:

- 86% vol. CH_4 and 14% vol. N_2 (reference gas G25).
- 90% vol. CH_4 and 10% vol. CO_2.
- 95% vol. CH_4 and 5% vol. C_3H_8 (typical of real natural gases).
- 87% vol. CH_4 and 13% vol. C_3H_8 (reference gas G21).
- 77% vol. CH_4 and 23% vol. H_2 (reference gas G222).

The secondary components are first added to and then removed from the fuel to test the ability of the control loop to regulate the fuel flow rate in both ways.

In Fig. 9.7, modifications of the fuel composition and automatic regulation are intentionally separated. The automatic regulation (green dotted line) is disabled at the beginning. When the secondary components (purple dashed lines, right axis) are added, the real equivalence ratio is automatically affected, while the detected value (red line) shows a lag and takes up to 30 seconds to stabilize at the correct value. The main contribution to this time lag is related to the lapse of time required by the burner to reach a stable temperature as discussed in Section 9.4. The regulation is then manually turned on. The real equivalence ratio is shown to be quickly brought back to the set value, despite a slight over-shoot during a few seconds. The difference with respect to the set value remains generally below $|\Delta\phi| = 0.01$ as shown by the results in Fig. 9.7.a

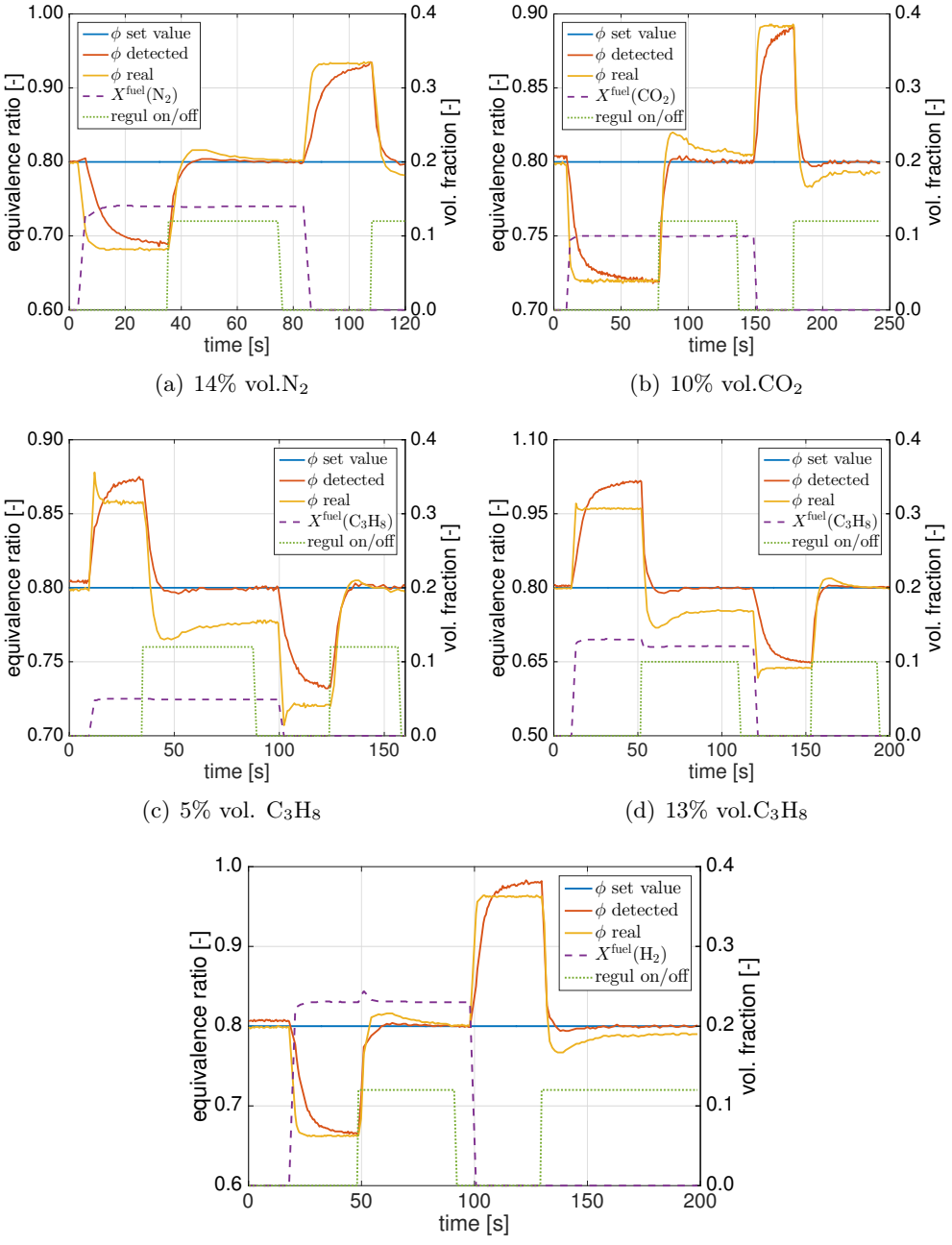

(a) 14% vol.N_2

(b) 10% vol.CO_2

(c) 5% vol. C_3H_8

(d) 13% vol.C_3H_8

(e) 23% vol. H_2

Figure 9.7: *Tests of the control system with binary fuel blends. Values for the equivalence ratio (solid lines) are presented on the left axis and the secondary component molar fraction (purple dashed line) on the right one. The signal for automatic fuel flow rate regulation (green dotted line with arbitrary scale) is sent manually after the detected equivalence ratio value yields stable values.*

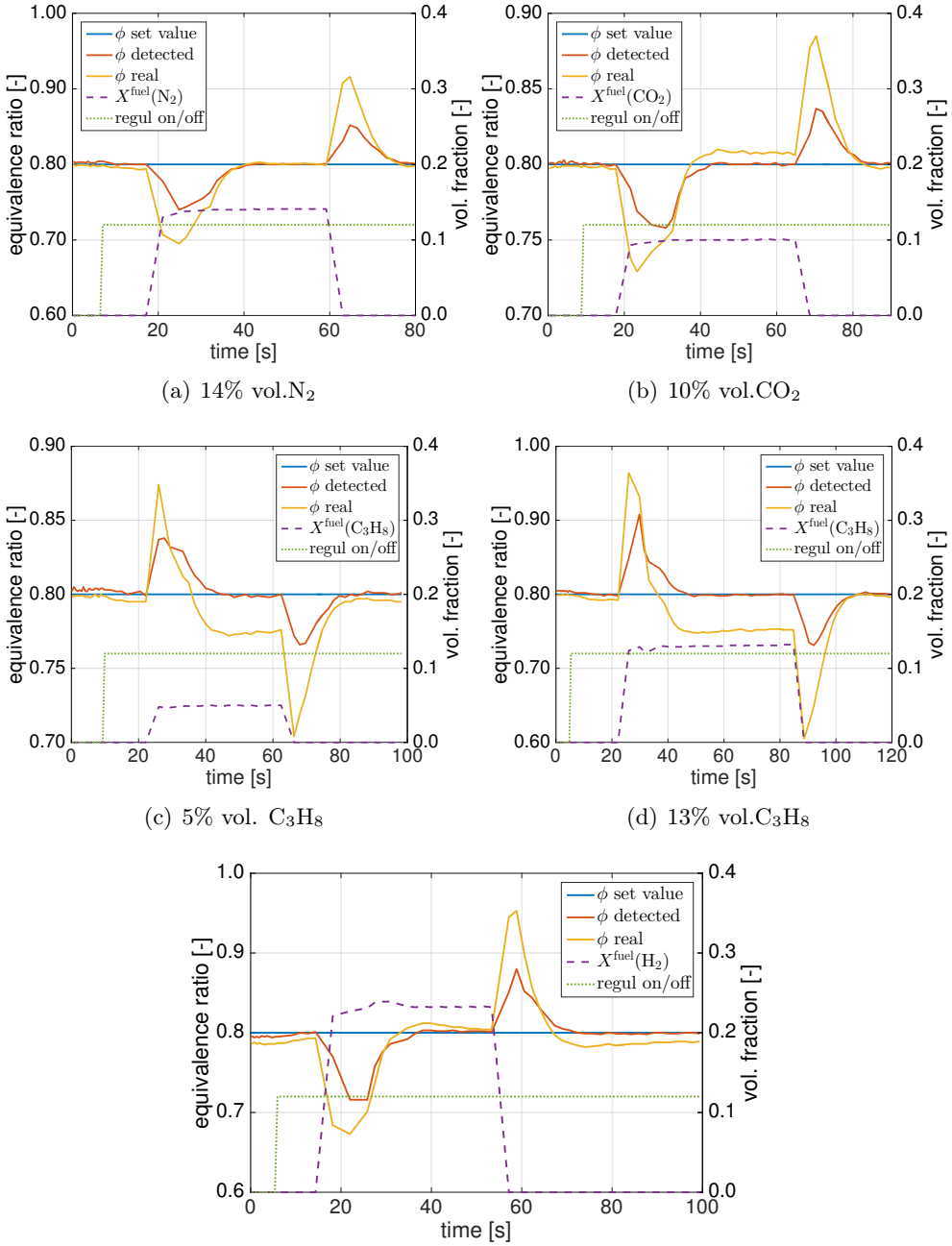

(a) 14% vol.N_2

(b) 10% vol.CO_2

(c) 5% vol. C_3H_8

(d) 13% vol.C_3H_8

(e) 23% vol. H_2

Figure 9.8: *Tests of the control system with binary fuel blends. Values for the equivalence ratio (solid lines) are presented on the left axis and the secondary component molar fraction (purple dashed line) on the right one. The signal for automatic fuel flow rate regulation (green dotted line with arbitrary scale) is permanently enabled.*

with 14% vol. N_2, Fig. 9.7.b with 10% vol. CO_2 and Fig. 9.7.e with 23% vol. H_2. Only C_3H_8 enrichment causes relatively bigger deviations of $|\Delta\phi| \sim 0.03$ for $X^{\text{fuel}}(C_3H_8) = 0.05$ in Fig. 9.7.c and $|\Delta\phi| \sim 0.05$ for $X^{\text{fuel}}(C_3H_8) = 0.13$ in Fig. 9.7.d. When the secondary components are removed from the fuel in the second part of these tests, the automatic regulation also successfully brings the equivalence ratio back to the set value.

Figure 9.8 show similar experiments but with the automatic regulation permanently enabled. The control system is again found to react correctly to changes of the fuel composition for all cases tested and allow to regulate the equivalence ratio.

The control loop developed in this work differs from that of Docquier et al. (2002) in some aspects. In their work the equivalence ratio sensing is realized with a lookup table consisting of two ratios OH^*/CH^* and CO_2^*/CH^*, while in the present thesis the OH^* intensity from photomultiplier tube scaled at different air flow rates is adopted as the equivalence ratio indicator. It allows the control system to be extended to a wider set of fuel scenarios. The validation procedure is similar to Docquier et al. (2002) but with some extensions. Tests with modifications of the equivalence ratio set value and dilution by N_2 were already carried out by Docquier et al. (2002). The validation is extended here to different flame powers and to a wider set of secondary components including CO_2, H_2 and C_3H_8. On the other hand, no special attempt was made in the present work to optimize the PID controller of the different flow devices, which is not the main purpose. Also, the impact of the contamination of light-collecting equipments was not tested. One reminds that the OH^* signal intensity scaled at different air flow rates which is used to determine the equivalence ratio in this study is vulnerable to signal intensity attenuation due to aging of the light collecting system or other sources of contamination obscuring the optical path.

Conclusion

Three techniques have been envisaged to detect the equivalence ratio and the OH^* signal measured by a photomultiplier tube equipped with a narrow band filter has finally been retained. It results from a compromise and gives good predictions of the equivalence ratio for a wide set of fuel blends. This signal is at the same time relatively easy to measure, making it promising for an industrial application.

An automatic equivalence ratio control loop has then been developed using the OH^* intensity as an input. Tests made with fuel blends have shown that the

system is able to regulate the equivalence ratio when secondary fuel components (N_2, CO_2, H_2, C_3H_8) are injected in the combustible mixture, with an error on the equivalence ratio in most cases lower than $|\Delta\phi| = 0.01$. Only C_3H_8, and also a priori C_2H_6 which was not tested, enriched fuel mixtures cause relatively larger differences, for the detected equivalence ratio with $|\Delta\phi| \sim 0.03$ for $X^{\text{fuel}}(C_3H_8) = 0.05$ and $|\Delta\phi| \sim 0.05$ for $X^{\text{fuel}}(C_3H_8) = 0.13$. These slight differences still remain tolerable.

Despite the success of this demonstrative control loop, additional issues still need to be addressed when applying the technique to real gas boilers:

- The tests made for the validation of the control loop were carried out at well stabilized states. However, as demonstrated in Section 9.4, the OH^* signal of the multi-perforated burner is strongly impacted by the burner temperature under transitional states. Consequently it takes several minutes for the OH^* signal to reach a stable value following a cold start or a drastic change of the flow operating conditions. During this period the predicted equivalence ratio is incorrect. This may not be a problem for the variations the natural gas composition, for which the characteristic time would be much longer. However, the burner power is likely to be subject to frequent and drastic changes according to the demand for heating and hot water. The lag of OH^* signal can make it unable to respond sufficiently fast to these changes.

- The tests were carried out within the lower part (4-7 kW) of the power modulation range covered by the burner (3-30 kW), due to the limitations of the test bench. At higher power, the flames over the multi-perforated surface may be less uniform and partial flame detachment may occur. These factors may lead to further uncertainties to the detected OH^* signal and disturb the equivalence ratio sensing. The validation procedure needs therefore to be extended to the whole power range of the burner.

- The selected equivalence ratio indicator exploiting the OH^* intensity is vulnerable to various sources of signal attenuation, caused for example by condensate deposits.

- The geometrical restrictions in a real gas boiler may lead to difficulties for the optical access to the chemiluminescence signal. In addition, light reflection from metallic components such as the heat exchanger may also alter the characterization of the chemiluminescence signal.

- The combination of a photomultiplier tube and a bandpass interference optical filter remains economically unrealistic to be integrated to a domestic gas boiler. Low-cost alternative sensor solutions need to be identified.

Conclusion

The future trend of greater variations of natural gas composition in the European gas network calls for an automatic combustion state regulation system. Potential technical solutions for this purpose have been reviewed in the Introduction and the theme of research is then narrowed down to two low cost techniques of flame chemiluminescence and ionization current.

In Part I, the flame chemiluminescence has been studied experimentally with three burner configurations and numerically with a 1-D flame models.

- The effects of secondary natural gas components on the chemiluminescence emission intensities of OH^*, CH^* and CO_2^* radicals have been documented. The most remarkable change is the significant increase of CH^* emission with C_2H_6 and C_3H_8 addition in the fuel mixture. Consequently, the widely used equivalence ratio indicator CH^*/OH^* is no longer reliable when heavier hydrocarbons are present in the natural gas. Instead, the OH^* intensity alone is proposed as an alternative indicator.

- The numerical approach correctly reproduces in most cases the changes of the OH^* and CH^* chemiluminescence signals caused by the injection of N_2, CO_2 and H_2 in the combustible mixture. However, larger differences with respect to the experimental results are noticed for C_2H_6 and C_3H_8 addition, probably due to the weakness of chemical kinetic mechanisms considered for their chemistry and their chemiluminescence. The order of magnitude is nevertheless correct. In addition, the simulations reveal that changes of chemiluminescence intensity with the equivalence ratio and with the secondary components N_2, CO_2 and H_2 can be partly attributed to the modification of the flame temperature.

- The flame-burner heat exchange, taking place when the gas injection velocity u_0 drops below the adiabatic laminar burning velocity S_L, is found to modify the chemiluminescence intensity. At fixed equivalence ratios, experimental results provide clear evidences of a nonlinear relationship between the chemiluminescence intensity signal and the mixture flow rate in

the regime $u_0/S_L < 1$. On the other hand, in the regime $u_0/S_L > 1$, the chemiluminescence intensity is proportional to the reactant stream flow rate, except for for the OH^* and CO_2^* signals measured on the cylindrical multi-perforated burner with equivalence ratios close to the stoichiometry. Another consequence of the flame-burner heat exchange is that the hot burner preheats the inlet stream of reactants. Experiments on the porous plug burner show that a higher inlet gas temperature enhances the chemiluminescence intensity for freely-propagating adiabatic flames ($u_0/S_L > 1$), while it has no effects on the burner-stabilized flames by heat losses ($u_0/S_L < 1$). However, this conclusion should not be directly extended to the cylindrical multi-perforated burner, as the flames may be stabilized simultaneously in both regimes over the complex surface injection area of this burner.

- The experimental observations made on the impact of the flame-burner heat exchange, including the evolution of the specific chemiluminescence intensity with the inlet gas velocity u_0 and the inlet gas temperature T_0, are then successfully reproduced by the numerical simulations conducted with a burner-stabilized non-adiabatic flame model. In addition, all these effects can be interpreted by considering the correlation between the specific chemiluminescence intensity I_s and the burnt gas temperature T_b of non-adiabatic flames.

- Experiments have also been performed to understand the disturbing factors altering the chemiluminescence signal characterization, including the impact of a region filled with burnt gases between the flame and the detector, the impact of the downstream confinement of the combustion reaction with a heat exchanger, and the light absorption of ground state OH radicals. The chemiluminescence signal has been found to depend on the sensor position and observation angle.

In Part II, the flame ionization current has been investigated with the conical flame burner.

- The flame ionization current is found to remain almost constant when the probe is in contact with the flame front. Otherwise, it decreases with the distance between the probe and the flame front. When the ionization probe is in contact with the flame front, the current intensity decreases with the inlet gas velocity.

- At fixed power and equivalence ratio, N_2 and CO_2 dilution cause the current intensity to decrease while H_2, C_2H_6 and C_3H_8 enrichment cause an increase of the ionization current. These secondary natural gas components lead to errors in the detection of the equivalence ratio, which nevertheless remain limited.

- The product of the chemiluminescence intensity ratio CH^*/OH^* and the ionization current is proposed as a new indicator for the flame equivalence ratio. The major advantage of this indicator is a considerably reduced error for the detection of the equivalence ratio in natural gases with H_2 enrichment compared to the strategies with the two quantities used alone.

- The drop of electrical potential between the flame base and the burner rim serving as the cathode accounts for more than 90% of the voltage applied between the ionization probe and the burner. The dead space between flame base and the burner rim is the major bottleneck of ionization current. The evolution of the current intensity with the flame conditions is attributed to the modification of the size of dead space between the flame base and the burner rim.

In Part III, a demonstrative equivalence regulation system has been conceived with LabVIEW and is tested on the cylindrical multi-perforated burner operated with three mass fllow controllers.

- Three equivalence ratio indicators are examined and the OH^* intensity measured by a photomultiplier tube mounted with a bandpass optical filter is finally selected. This indicator is scaled at different air flow rates. The preliminary tests show that the equivalence ratio is predicted with a very small bias error for pure methane, mild N_2-, CO_2-diluted methane mixtures and H_2-enriched methane mixtures. The errors slightly increase with C_3H_8 addition, but still remain tolerable at the operational equivalence ratio of gas boilers lower or close to $\phi \sim 0.8$.

- The OH^* signal features however a large time lag with respect to its steady state value reaching up to several minutes following a cold start or a drastic change of flow operating conditions. This issue has been discussed and the time lag is attributed to the burner temperature which takes time to reach thermal equilibrium.

- An automatic control loop is constructed accordingly. It is shown to respond correctly to changes of the equivalence set value and the injection of secondary components including N_2, CO_2, H_2 and C_3H_8. The real equivalence ratio is retrieved automatically by the detection/control system within $|\Delta\phi| = 0.01$ except for experiments conducted with C_3H_8 enriched fuel mixtures. For C_3H_8 enrichment the deviation rises to $|\Delta\phi| \sim 0.03$ for $X^{\text{fuel}}(C_3H_8) = 0.05$ and $|\Delta\phi| \sim 0.05$ for $X^{\text{fuel}}(C_3H_8) = 0.13$, which however still remain tolerable.

Perspectives

For the equivalence ratio regulation based on the flame chemiluminescence, future work remains on the practical difficulties to be solved for the application of the identified equivalence ratio sensing strategy to real gas boilers.

- The control strategy needs to be validated in a real gas boiler over the entire power range of $3 - 30\,\mathrm{kW}$. For this purpose, an optical path needs to be designed taking into account the geometrical restrictions inside a real gas boiler.

- Despite its many interesting features for equivalence ratio sensing, the OH^* signal suffers from several weaknesses. For example, the relatively long time needed to achieve the stabilized signal may compromise its performances. Finally, using one single chemiluminescence emission makes it vulnerable to signal intensity attenuation due to optical system contamination for example. This issue needs to be evaluated and periodic recalibration might be necessary.

Concerning the technique of flame ionization current:

- The experiments performed on the conical flame in the laboratory with a simple geometry enabled the characterization of the main fuel and flow parameters altering the ionization signal and also allowed to initiate a fundamental understanding of the major factor deciding the current intensity. It then remains to verify whether the conclusions are applicable to the cylindrical multi-perforated burner employed in real gas boilers.

- In the parametric analysis, most of the experiments were carried out with the probe in contact with the flame front, in order to avoid the impact of the probe position. However, in real gas boilers, flames stabilized on the burner surface are generally short, hence in many cases the probe lies in the zone of burnt gases. A better and more detailed knowledge is necessary for this regime of operation.

- The flame standoff distance has be shown to be an important factor deciding the ionization current intensity. However, the approach followed in the present work is still relatively rough, ignoring many factors potentially responsible for the ionization current intensity. Small deviations for the ionization current from the standoff distance correlation were indeed noticed. It is then interesting to further investigate the electrical properties of the dead space between the flame base and the burner rim.

Appendix A

Self-similarity of peak shapes

The following figures show a zoomed view of the chemiluminescence spectra near 310 nm and 430 nm with the intensity normalized respectively by the OH* and CH* peak height. The main observation is that the shapes of the OH* and CH* emission peaks are generally self-similar in Figs.A.1 to A.5 when various flame parameters are varied. One exception may be seen for the CH* emission when the fuel of methane is enriched by C_3H_8. This self-similar behavior of the OH* and CH* distributions indicates that the two methods to record the emission intensity from the spectrometer measurements by taking the peak height or the peak area make no significant differences. The conclusions obtained in the present thesis remain therefore unchanged by the choice of the method used to deduce the OH* and CH* emissions from the spectral data records.

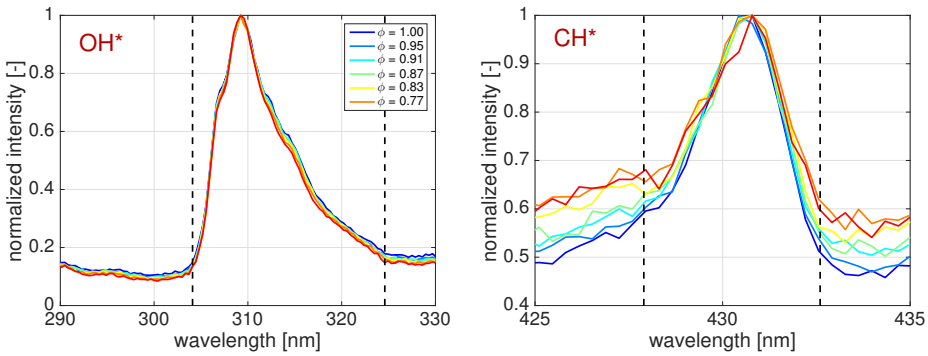

Figure A.1: *Shapes of OH* and CH* emission peaks from the conical flame burner with different equivalence ratios:* $\phi = 0.77 - 1.00$

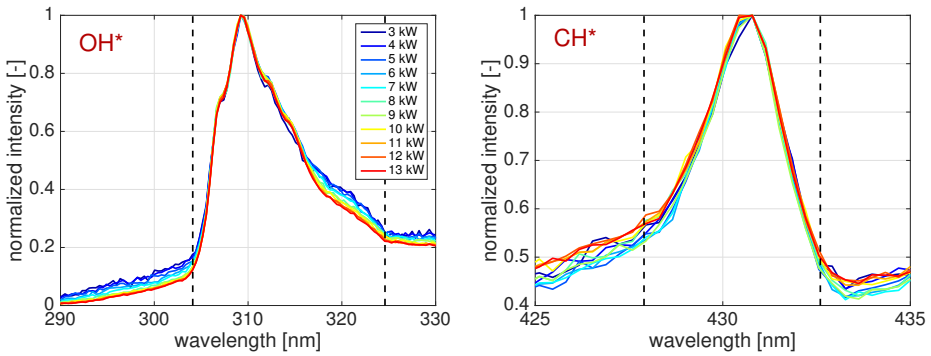

Figure A.2: *Shapes of OH* and CH* emission peaks from the cylindrical multi-perforated burner with different powers:* $P = 3 - 13\,\mathrm{kW}$.

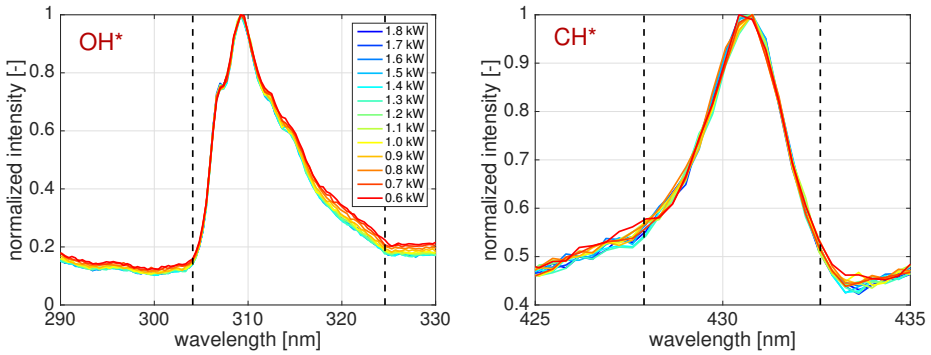

Figure A.3: *Shapes of OH* and CH* emission peaks from the porous plug burner with different powers:* $P = 0.6 - 1.8\,\mathrm{kW}$.

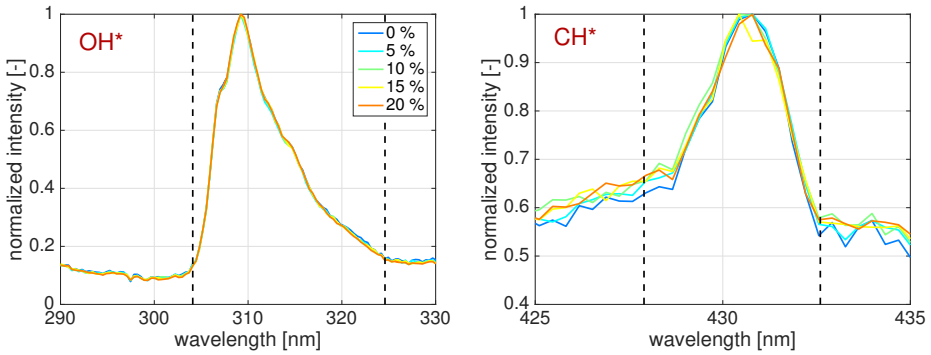

Figure A.4: *Shapes of OH* and CH* emission peaks from the conical flame burner with different* H_2 *fraction:* $X^{\mathrm{fuel}}(\mathrm{H_2}) = 0 - 20\%$.

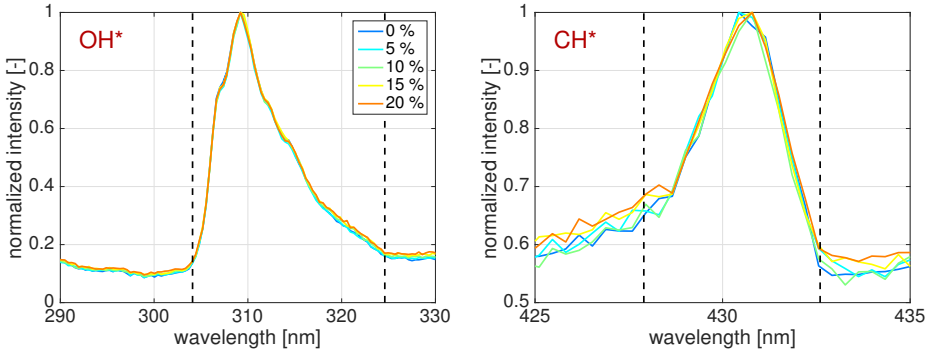

Figure A.5: *Shapes of OH* and CH* emission peaks from the conical flame burner with different CO_2 fraction:* $X^{\mathrm{fuel}}(\mathrm{CO_2}) = 0 - 20\%$.

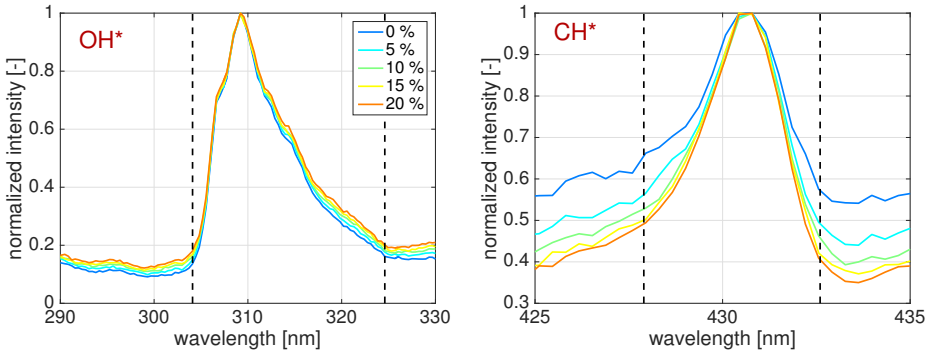

Figure A.6: *Shapes of OH* and CH* emission peaks from the conical flame burner with different* $\mathrm{C_3H_8}$ *fraction:* $X^{\mathrm{fuel}}(\mathrm{C_3H_8}) = 0 - 20\%$.

Appendix B

ICCD images of flame standoff distance

The original ICCD photos for the measurement of the flame standoff distance are provided below in Fig. B.1. Several parameters are varied including the equivalence ratio, the bulk gas velocity, and the fuel composition with the injection of CO_2, H_2 and C_3H_8. These images give rise to the results in Tab. 8.3 and Fig. 8.9.

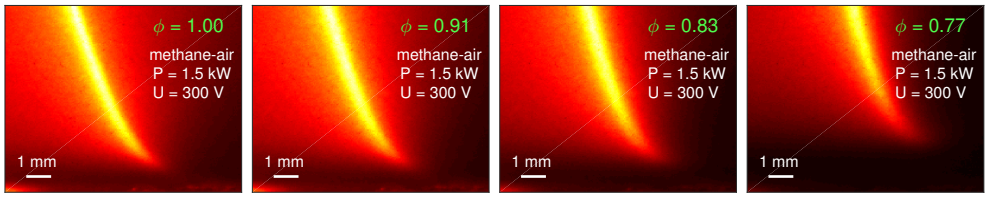

(a) Change of equivalence ratio

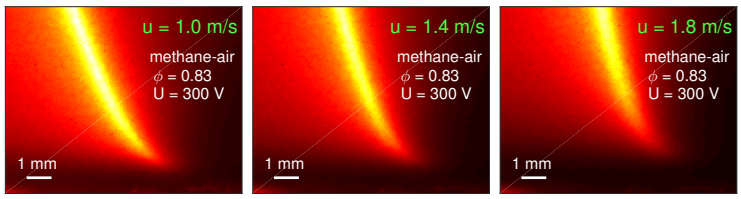

(b) Change of bulk gas velocity

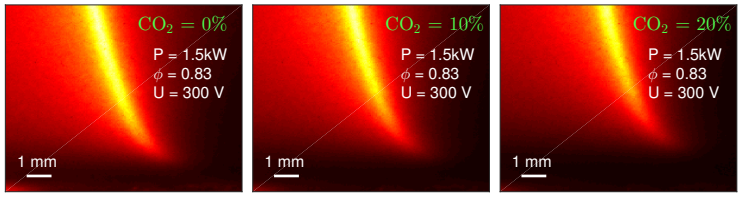

(c) Dilution with CO_2

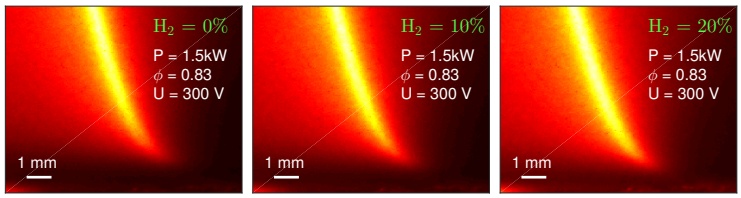

(d) Enrichment with H_2

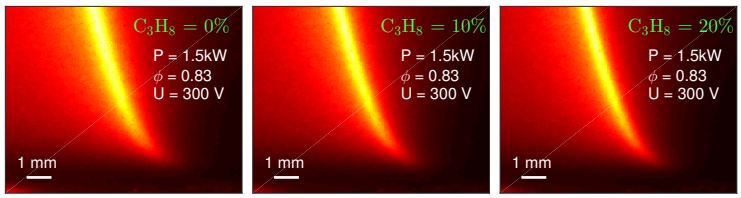

(e) Enrichment with C_3H_8

Figure B.1: *Original ICCD photos for the measurement of flame standoff distance. The flow operating conditions and the ionization probe voltage are indicated in the images.*

Appendix C

LabVIEW diagrams

The following figures illustrate the LabVIEW block diagrams of the equivalence ratio control loop and the important subroutines (subVIs).

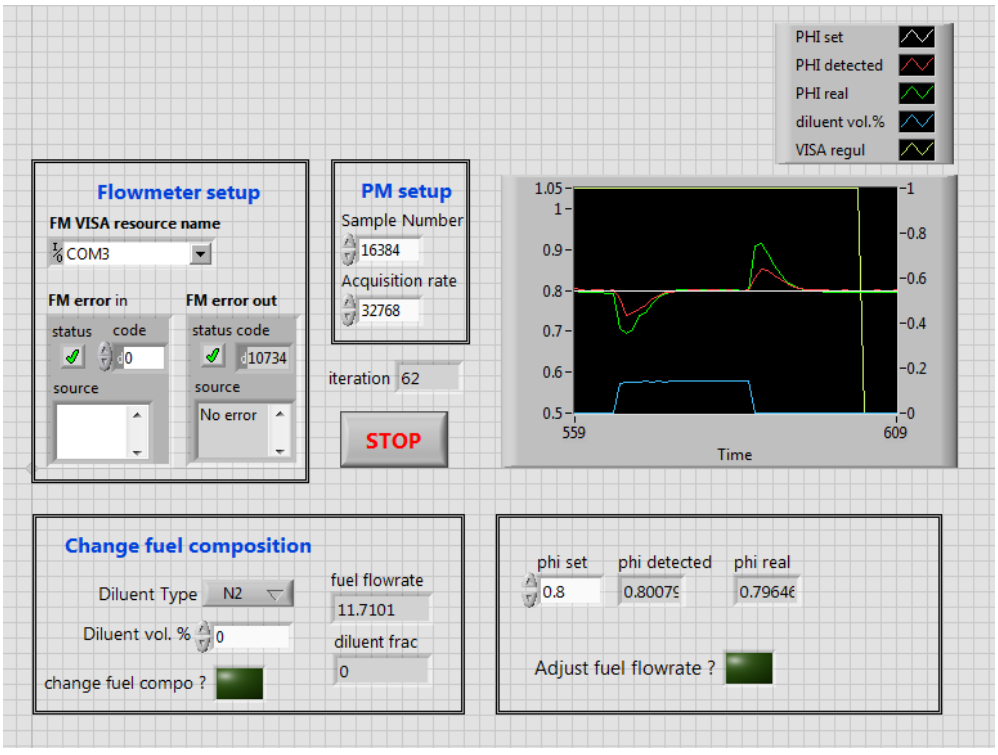

Figure C.1: *LabVIEW front panel for the demonstrative equivalence ratio control loop.*

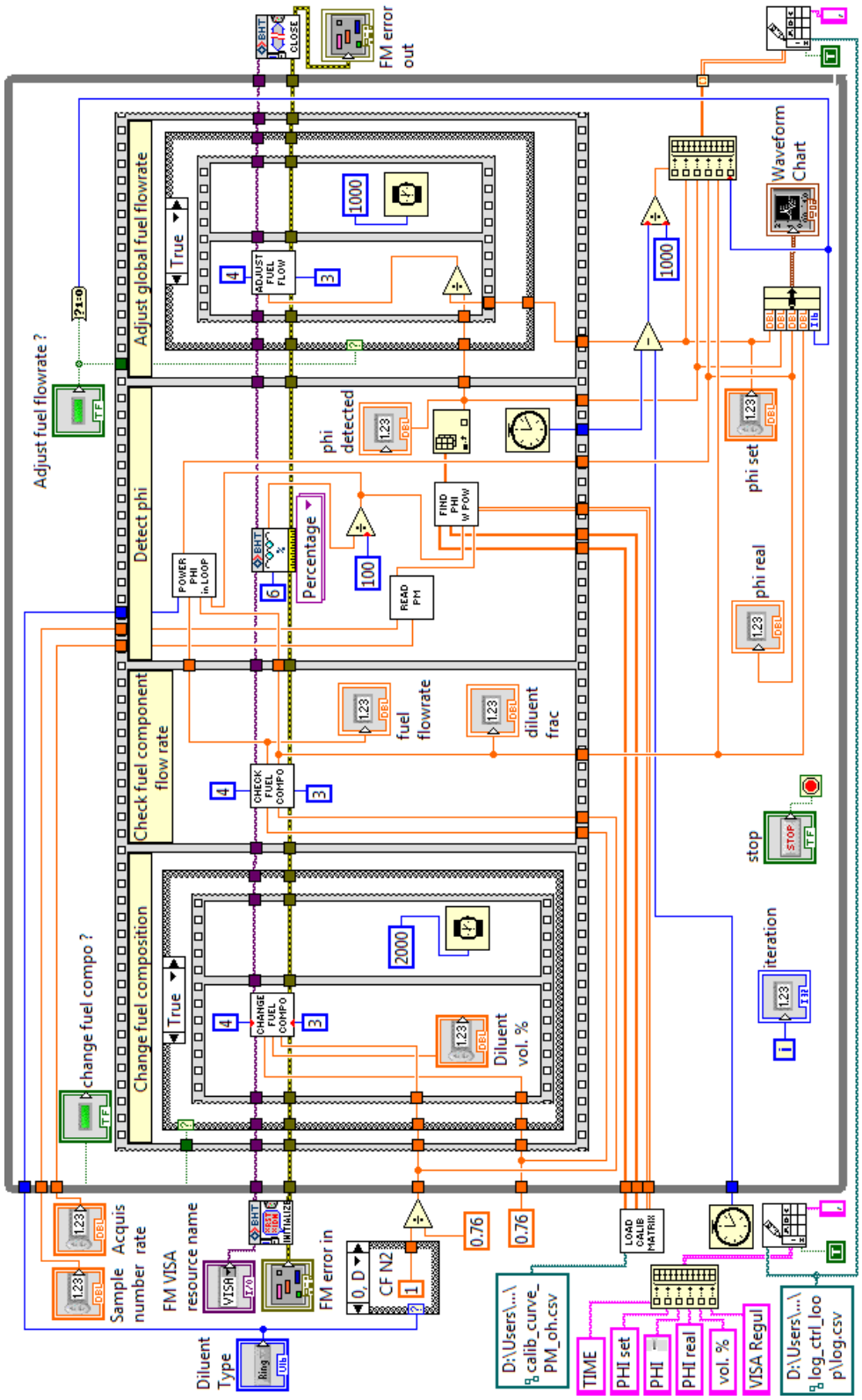

Figure C.2: *LabVIEW block diagram for the demonstrative equivalence ratio control loop.*

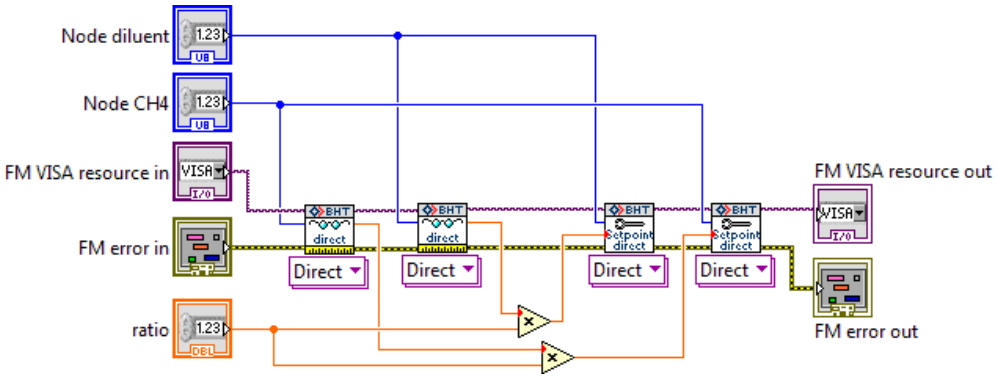

Figure C.3: *SubVI adjusting the global fuel flow rate according to the ratio of the detected equivalence ratio and the set value.*

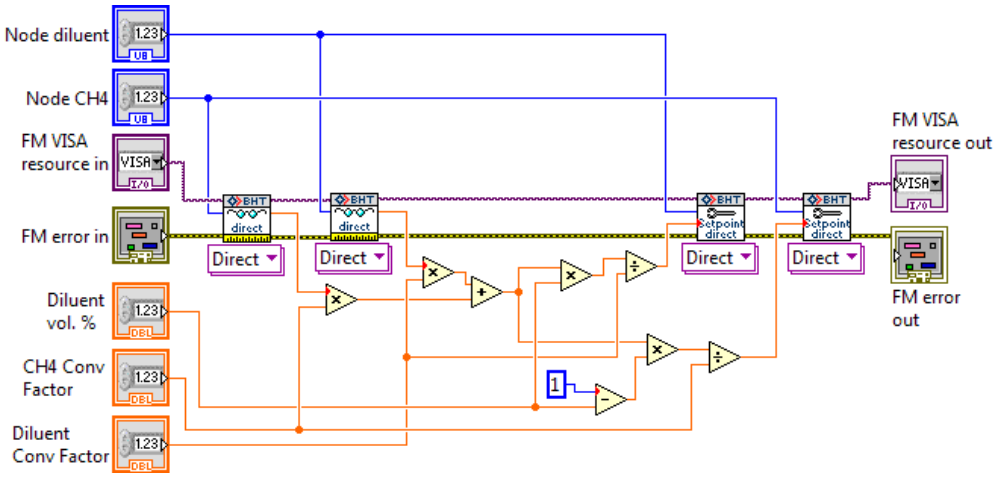

Figure C.4: *SubVI changing the fuel composition.*

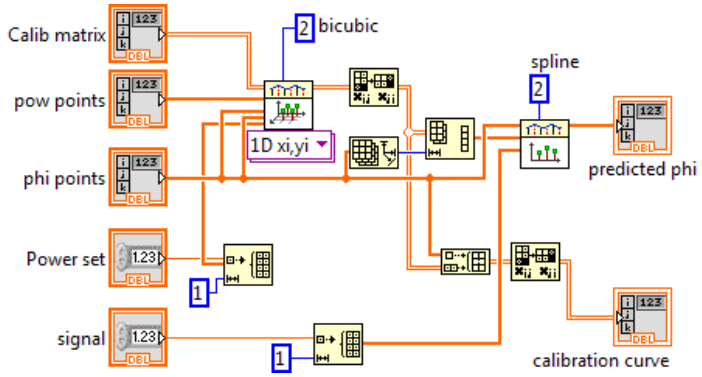

Figure C.5: *SubVI detecting the equivalence ratio from the measured OH* signal intensity, based on the stored calibration lookup table and the air flow rate.*

References

Adelt, M., M. Hoppe, M. Montero, and G. Peureux (2010). Report on gas composition range in Europe DB0.1. Technical report, INGAS. *(p. ix, 1, 2)*

Altendorfner, F., J. Kuhl, L. Zigan, and A. Leipertz (2011). Study of the influence of electric fields on flames using planar LIF and PIV techniques. *Proceedings of the Combustion Institute 33*(2), 3195 – 3201. *(p. 120)*

Alviso, D., J. Rolon, P. Scouflaire, and N. Darabiha (2015). Experimental and numerical studies of biodiesel combustion mechanisms using a laminar counterflow spray premixed flame. *Fuel 153*, 154 – 165. *(p. ix, 49, 54)*

Arias, L., S. Torres, D. Sbarbaro, and O. Farias (2008). Photodiode-based sensor for flame sensing and combustion-process monitoring. *Applied optics 47*(29), 5541–5549. *(p. 24)*

Ballester, J. and T. García-Armingol (2010). Diagnostic techniques for the monitoring and control of practical flames. *Progress in Energy and Combustion Science 36*(4), 375 – 411. *(p. 23)*

Ballester, J., A. Sanz, R. Hernández, and A. Smolarz (2005). Detection and analysis of emitted radiation for advanced monitoring and control of combustors. In *Congress on Optics and Optoelectronics*, pp. 59482H–1. International Society for Optics and Photonics. *(p. 21)*

Barra, A. J. and J. L. Ellzey (2004). Heat recirculation and heat transfer in porous burners. *Combustion and Flame 137*(1-2), 230 – 241. *(p. 30, 74)*

Botha, J. P. and D. B. Spalding (1954). The laminar flame speed of propane/air mixtures with heat extraction from the flame. *Proceedings of the Royal Society of London A: Mathematical, Physical and Engineering Sciences 225*(1160), 71–96. *(p. xiii, 72, 73)*

Brown, D. M., P. M. Sandvik, J. B. Fedison, J. Hibshman, and K. S. Matocha (2008). Determination of lean burn combustion temperature using ultraviolet emission. *IEEE Sensors Journal 8*(3), 255–260. *(p. 22)*

Calcote, H. (1961). Ion production and recombination in flames. *Symposium (International) on Combustion 8*(1), 184 – 199. Eighth Symposium (International) on Combustion. *(p. 104)*

Clark, T. (1958). Studies of OH, CO, CH and C2 radiation from laminar and turbulent propane-air and ethylene-air flames-NACA technical note

4266. Technical report, Technical report, National Advisory Committee for Aeronautics, Lewis Flight Propulsion Laboratory Cleveland, Ohio. *(p. 23)*

Crosley, D. R. and G. P. Smith (1980). Vibrational energy transfer in laser-excited a $^2\sigma^+$ OH as a flame thermometer. *Applied optics 19*(4), 517–520. *(p. 22)*

Cullen, R. E. (1950). *The Effect of Pressure on the Propagation Rate of Bunsen Flames in Propane-Air and Ethylene-Air Mixtures*. Willow Run Research Center, Engineering Research Institute, University of Michigan. *(p. 120)*

Daniel, W. (1957). Flame quenching at the walls of an internal combustion engine. *Symposium (International) on Combustion 6*(1), 886 – 894. Sixth Symposium (International) on Combustion. *(p. 120)*

Davidson, D., M. Roehrig, E. Petersen, M. D. Rosa, and R. Hanson (1996). Measurements of the OH A-X (0,0) 306 nm absorption bandhead at 60 atm and 1735 K. *Journal of Quantitative Spectroscopy and Radiative Transfer 55*(6), 755 – 762. *(p. 21)*

de Goey, L., J. van Oijen, V. Kornilov, and J. ten Thije Boonkkamp (2011). Propagation, dynamics and control of laminar premixed flames. *Proceedings of the Combustion Institute 33*(1), 863 – 886. *(p. 28, 71)*

Docquier, N. and S. Candel (2002). Combustion control and sensors: a review. *Progress in Energy and Combustion Science 28*(2), 107 – 150. *(p. 5)*

Docquier, N., F. Lacas, and S. Candel (2002). Closed-loop equivalence ratio control of premixed combustors using spectrally resolved chemiluminescence measurements. *Proceedings of the Combustion Institute 29*(1), 139 – 145. *(p. 24, 143)*

Durox, D., F. Baillot, G. Searby, and L. Boyer (1997). On the shape of flames under strong acoustic forcing: a mean flow controlled by an oscillating flow. *Journal of fluid mechanics 350*, 295–310. *(p. 29)*

Fialkov, A. B. (1997). Investigations on ions in flames. *Progress in Energy and Combustion Science 23*(5), 399 – 528. *(p. 103, 104, 105)*

Franke, A. (2002). *Characterization of an Electrical Sensor for Combustion Diagnostics*. Ph. D. thesis, Lund University. *(p. xiv, xv, 10, 11, 103, 105, 106, 107, 112, 113)*

García-Armingol, T. and J. Ballester (2014a). Flame chemiluminescence in premixed combustion of hydrogen-enriched fuels. *International Journal of Hydrogen Energy 39*(21), 11299–11307. *(p. 24)*

García-Armingol, T. and J. Ballester (2014b). Influence of fuel composition on chemiluminescence emission in premixed flames of CH4/CO2/H2/CO blends. *International Journal of Hydrogen Energy 39*(35), 20255 – 20265. *(p. 24)*

García-Armingol, T., J. Ballester, and A. Smolarz (2013). Chemiluminescence-based sensing of flame stoichiometry: Influence of the measurement method. *Measurement 46*(9), 3084 – 3097. *(p. 40)*

García-Armingol, T., Y. Hardalupas, A. Taylor, and J. Ballester (2014). Effect of local flame properties on chemiluminescence-based stoichiometry measurement. *Experimental Thermal and Fluid Science 53*, 93 – 103. *(p. 24)*

Geddis, P. J. (2009). *Evaluation of chemiluminescence as a measurement option for industrial flame monitoring and process control*. Ph. D. thesis, University of Toronto. *(p. 19)*

Giovangigli, V. (1999). Plane laminar flames with multicomponent transport and complex chemistry. *Mathematical Models and Methods in Applied Sciences 09*(03), 337–378. *(p. 47)*

Goodings, J., D. Bohme, and C.-W. Ng (1979a). Detailed ion chemistry in methane-oxygen flames. i. positive ions. *Combustion and Flame 36*, 27 – 43. *(p. xiv, 103, 104)*

Goodings, J., D. Bohme, and C.-W. Ng (1979b). Detailed ion chemistry in methane-oxygen flames. ii. negative ions. *Combustion and Flame 36*, 45 – 62. *(p. xiv, 103, 105, 113)*

Guethe, F., D. Guyot, G. Singla, N. Noiray, and B. Schuermans (2012). Chemiluminescence as diagnostic tool in the development of gas turbines. *Applied Physics B 107*(3), 619–636. *(p. 21)*

Guiberti, T. (2015, February). *Analysis of the topology of premixed swirl-stabilized confined flames*. Phd dissertation, Ecole Centrale Paris. *(p. 44)*

Guiberti, T. F., D. Durox, C. Mirat, and T. Schuller (2015, 07). Comparisons between 1-D simulations and experiments of OH*, CH*, and CO2* emissions in N2 and CO2 diluted laminar premixed flames. In *10th ASPACC*, Beijing. *(p. 24)*

Hardalupas, Y. and M. Orain (2004). Local measurements of the time-dependent heat release rate and equivalence ratio using chemiluminescent emission from a flame. *Combustion and Flame 139*(3), 188–207. *(p. 24)*

Hardalupas, Y., M. Orain, C. S. Panoutsos, A. Taylor, J. Olofsson, H. Seyfried, M. Richter, J. Hult, M. Aldén, F. Hermann, and J. Klingmann (2004). Chemiluminescence sensor for local equivalence ratio of reacting mixtures of fuel and air (FLAMESEEK). *Applied Thermal Engineering 24*(11-12), 1619 – 1632. Industrial Gas Turbine Technologies. *(p. 21)*

Higgins, B., M. McQuay, F. Lacas, and S. Candel (2001). An experimental study on the effect of pressure and strain rate on ch chemiluminescence of premixed fuel-lean methane/air flames. *Fuel 80*(11), 1583–1591. *(p. 22, 24, 77)*

Higgins, B., M. McQuay, F. Lacas, J.-C. Rolon, N. Darabiha, and S. Candel (2001). Systematic measurements of oh chemiluminescence for fuel-lean, high-pressure, premixed, laminar flames. *Fuel 80*(1), 67–74. *(p. 22, 24, 77)*

Hurle, I. R., R. B. Price, T. M. Sugden, and A. Thomas (1968). Sound emission from open turbulent premixed flames. *Proceedings of the Royal*

Society of London A: Mathematical, Physical and Engineering Sciences 303(1475), 409–427. *(p. 22, 77)*

Johnson, M., L. Kostiuk, and R. Cheng (1998). A ring stabilizer for lean premixed turbulent flames. *Combustion and flame 114*(3), 594–596. *(p. 29)*

Jones, H. R. N. (1989). *The application of combustion principles to domestic gas burner design*. Taylor & Francis. *(p. 3, 4)*

Joulin, G. and P. Clavin (1979). Linear stability analysis of nonadiabatic flames: Diffusional-thermal model. *Combustion and Flame 35*, 139 – 153. *(p. 53, 72)*

Karrer, M. (2009). *Diagnostic des plasmas de combustion par sonde d'ionisation: application à l'étude de l'interaction flamme-paroi instationnaire*. Ph. D. thesis, Chasseneuil-du-Poitou, Ecole nationale supérieure de mécanique et d'aéronautique. *(p. 108, 122)*

Karrer, M., M. Bellenoue, S. Labuda, J. Sotton, and M. Makarov (2010). Electrical probe diagnostics for the laminar flame quenching distance. *Experimental Thermal and Fluid Science 34*(2), 131 – 141. *(p. 106, 122)*

Kathrotia, T. (2011). *Reaction kinetics modeling of OH*, CH*, and C2* chemiluminescence*. Ph. D. thesis, Ruprecht-Karls-Universität Heidelberg. *(p. 19)*

Kedia, K. S. (2010). *Numerical simulations of perforated plate stabilized premixed flames with detailed chemistry*. Ph. D. thesis, Massachusetts Institute of Technology. *(p. 120)*

Kiefer, M., U. Maas, S. Park, X. Pian, G. Köllmann, G. O. Loohuis, D. Leerkes, H. Kalk, D. Markus, and T. Langer (2012). Combustion control based on flame ionization. In *25th World Gas Conference*. *(p. xv, 106, 109, 110, 111, 112, 114)*

Knewstubb, P. and T. Sugden (1958). Mass spectrometry of the ions present in hydrocarbon flames. *Symposium (International) on Combustion 7*(1), 247 – 253. *(p. 104)*

Kojima, J., Y. Ikeda, and T. Nakajima (2000). Spatially resolved measurement of OH*, CH*, and C2* chemiluminescence in the reaction zone of laminar methane/air premixed flames. *Proceedings of the Combustion Institute 28*(2), 1757 – 1764. *(p. 23, 62)*

Kojima, J., Y. Ikeda, and T. Nakajima (2005). Basic aspects of OH (A), CH (A), and C2 (d) chemiluminescence in the reaction zone of laminar methane-air premixed flames. *Combustion and Flame 140*(1), 34–45. *(p. 19, 53)*

Konnov, A. A. (2015). The temperature and pressure dependences of the laminar burning velocity: experiments and modeling. In *Proc. 7th European Combustion Meeting, Budapest, Hungary, March 30-April 2*. *(p. 76)*

Lacour, C. (2006). *Stabilité de flammes laminaires partiellement prémélangées-Application aux brûleurs domestiques*. Ph. D. thesis, INSA de Rouen. *(p. 120)*

Lauer, M. and T. Sattelmayer (2010). On the adequacy of chemilumines-

cence as a measure for heat release in turbulent flames with mixture gradients. *Journal of Engineering for Gas Turbines and Power 132*(6), 061502. *(p. 23)*

Lauer, M., M. Zellhuber, T. Sattelmayer, and C. J. Aul (2011). Determination of the heat release distribution in turbulent flames by a model based correction of OH* chemiluminescence. *Journal of Engineering for Gas Turbines and Power 133*(12), 121501. *(p. 23)*

Lauer, M. R. W. (2011, 3). *Determination of the Heat Release Distribution in Turbulent Flames by Chemiluminescence Imaging*. Ph. D. thesis, Technische Universitët München. *(p. xi, 10, 18, 22)*

Law, C. and C. Sung (2000). Structure, aerodynamics, and geometry of premixed flamelets. *Progress in Energy and Combustion Science 26*(4-6), 459 – 505. *(p. 74, 77)*

Le Corre, O. and K. Loubar (2010). Natural gas: physical properties and combustion features. In *Natural Gas*. InTech. *(p. xi, 7)*

Lee, J. and D. Santavicca (2003). Experimental diagnostics for the study of combustion instabilities in lean premixed combustors. *Journal of propulsion and power 19*(5), 735–750. *(p. 22)*

Lee, S., S.-M. Kum, and C.-E. Lee (2011a). An experimental study of a cylindrical multi-hole premixed burner for the development of a condensing gas boiler. *Energy 36*(7), 4150 – 4157. *(p. 71)*

Lee, S., S.-M. Kum, and C.-E. Lee (2011b). Performances of a heat exchanger and pilot boiler for the development of a condensing gas boiler. *Energy 36*(7), 3945 – 3951. *(p. 4)*

Lewis, B. and G. von Elbe (1987). {CHAPTER} v - combustion waves in laminar flow. In B. Lewis and G. v. Elbe (Eds.), *Combustion, Flames and Explosions of Gases (Third Edition)* (Third Edition ed.)., pp. 215 – 417. San Diego: Academic Press. *(p. xv, 120)*

Lewis, B. and G. Von Elbe (1987). *Combustion, flames and explosions of gases*. Elsevier. *(p. 76)*

Lötters, J. C., T. S. Lammerink, M. Pap, R. G. Sanders, M. J. de Boer, A. Mouris, and R. J. Wiegerink (2013). Integrated micro wobbe index meter towards on-chip energy content measurement. In *26th International Conference on Micro Electro Mechanical Systems (MEMS)*, pp. 965–968. IEEE. *(p. 7)*

Luque, J. and D. R. Crosley (1996a). Electronic transition moment and rotational transition probabilities in CH. I. $A^2\Delta - X^2\Pi$ system. *The Journal of chemical physics 104*(6), 2146–2155. *(p. 18)*

Luque, J. and D. R. Crosley (1996b). Electronic transition moment and rotational transition probabilities in CH. II. $B^2\Sigma - X^2\Pi$ system. *The Journal of chemical physics 104*(11), 3907–3913. *(p. 18)*

Luque, J. and D. R. Crosley (1998). Transition probabilities in the $A^2\Sigma^+ - X^2\Pi$ electronic system of OH. *The Journal of chemical physics 109*(2), 439–448. *(p. xi, 18)*

Najm, H. N., P. H. Paul, C. J. Mueller, and P. S. Wyckoff (1998). On the adequacy of certain experimental observables as measurements of flame burning rate. *Combustion and flame 113*(3), 312–332. *(p. xi, 9, 10, 23)*

Näslund, M. (2014, 04). Combustion control in domestic gas appliances - fuel gases containing hydrogen. Technical report, Danish Gas Technology Centre. *(p. 11, 109)*

Nitschke-Kowsky, P. (2012). Impact of hydrogen admixture to natural gas on installed gas appliances. In *25th World Gas Conference*. *(p. 110)*

Nori, V. and J. Seitzman (2007). Chemiluminescence measurements and modeling in syngas, methane and jet-a fueled combustors. In *45th AIAA Aerospace Sciences Meeting and Exhibit, Reno, NV, January*, pp. 8–11. *(p. 21, 22)*

Nori, V. N. (2008). *Modeling and analysis of chemiluminescence sensing for syngas, methane and Jet-A combustion*. Ph. D. thesis, Georgia Institute of Technology. *(p. 20)*

Orain, M. and Y. Hardalupas (2010). Effect of fuel type on equivalence ratio measurements using chemiluminescence in premixed flames. *Comptes Rendus Mecanique 338*(5), 241–254. *(p. 24)*

Panoutsos, C., Y. Hardalupas, and A. Taylor (2009). Numerical evaluation of equivalence ratio measurement using OH* and CH* chemiluminescence in premixed and non-premixed methane-air flames. *Combustion and Flame 156*(2), 273 – 291. *(p. 24, 77)*

Pickenäcker, K., K. Wawrzinek, and D. Trimis (2000). Optimization of burners by air-ratio-controlled combustion based on wobbe number measurement. In *European conference on small burner and heating technology*, pp. 231–240. *(p. 6, 7)*

Popp, P. and M. Baum (1997). Analysis of wall heat fluxes, reaction mechanisms, and unburnt hydrocarbons during the head-on quenching of a laminar methane flame. *Combustion and Flame 108*(3), 327 – 348. *(p. 120)*

Qin, Z., V. V. Lissianski, H. Yang, W. C. Gardiner, S. G. Davis, and H. Wang (2000). Combustion chemistry of propane: A case study of detailed reaction mechanism optimization. *Proceedings of the Combustion Institute 28*(2), 1663 – 1669. *(p. 49)*

Rahmouni, C., O. L. Corre, and M. Tazerout (2003). Online determination of natural gas properties. *Comptes Rendus Mécanique 331*(8), 545 – 550. *(p. 6)*

Rodrigues, J. M. (2005). *Analyse de la répartition du potentiel et des charges dans une flamme polarisée. Corrélation avec la distance d'extinction*. Ph. D. thesis, Université de Rouen. *(p. 11, 106, 107, 108, 118, 122)*

Rodrigues, J. M., A. Agneray, X. Jaffrézic, M. Bellenoue, S. Labuda, C. Leys, A. P. Chernukho, A. N. Migoun, A. Cenian, A. M. Savel'ev, N. S. Titova, and A. M. Starik (2007). Evolution of charged species in propane/air flames: mass-spectrometric analysis and modelling. *Plasma Sources Science and Technology 16*(1), 161. *(p. 105)*

Samaniego, J.-M., F. Egolfopoulos, and C. Bowman (1995). CO2* chemiluminescence in premixed flames. *Combustion Science and Technology 109*(1-6), 183–203. *(p. 22, 23, 41, 54, 59)*

Sandrowitz, A. K., J. M. Cooke, and N. G. Glumac (1998, May). Flame emission spectroscopy for equivalence ratio monitoring. *Appl. Spectrosc. 52*(5), 658–662. *(p. 36)*

Schley, P., M. Jaeschke, K. Altfeld, and A. Ruhrgas (2003). New technologies for gas quality determination. In *Proceedings of the 22nd Word Gas Conference, Tokyo, Japan.* *(p. 6)*

Slater, C., T. Maeder, and P. Ryser (2010). Portable ltcc gas viscometer for determining wobbe number. *Procedia Engineering 5*, 307–310. *(p. 7)*

Smith, G. P., D. M. Golden, M. Frenklach, B. Eiteener, M. Goldenberg, C. T. Bowman, R. K. Hanson, W. C. Gardiner, V. V. Lissianski, and Z. W. Qin (2000). GRI-Mech 3.0: http://www.me.berkeley.edu/gri_mech/. *(p. 49)*

Smith, G. P., J. Luque, C. Park, J. B. Jeffries, and D. R. Crosley (2002). Low pressure flame determinations of rate constants for OH(A) and CH(A) chemiluminescence. *Combustion and Flame 131*(1-2), 59 – 69. *(p. ix, 49, 54)*

Smooke, M. D. (1982). Solution of burner-stabilized premixed laminar flames by boundary value methods. *Journal of Computational Physics 48*(1), 72 – 105. *(p. 51)*

Trindade, T., A. Ferreira, and E. Fernandes (2014). Characterization of combustion chemiluminescence: An image processing approach. *Procedia Technology 17*(Supplement C), 194 – 201. Conference on Electronics, Telecommunications and Computers - CETC 2013. *(p. 41)*

Tschulena, G. and A. Lahrmann (2006). *Sensors Applications, Sensors in Household Appliances*, Volume 5. John Wiley & Sons. *(p. ix, 5, 6)*

Van Maaren, A., D. Thung, and L. R. H. De Goey (1994). Measurement of flame temperature and adiabatic burning velocity of methane/air mixtures. *Combustion Science and Technology 96*(4-6), 327–344. *(p. 73)*

Warnatz, J. (1978). Calculation of the structure of laminar flat flames iii: Structure of burner-stabilized hydrogen-oxygen and hydrogen-fluorine flames. *Berichte der Bunsengesellschaft für physikalische Chemie 82*(8), 834–841. *(p. 53)*

Williams, T., N. Bryant, M. Brown, L. Eastell, A. Jones, A. Kane, A. Paxton, G. Davies, A. Morris, D. J. Cox, J. Wyatt, M. da Costa, S. Fidanboy, N. Austin, and S. Daut (2012, 07). Gas quality harmonization cost benefit analysis. Technical report, GL Noble Denton and Pöyry Management Consulting. *(p. 1)*

Zimmer, L., S. Tachibana, T. Yamamoto, Y. Kurosawa, and K. Suzuki (2003). Evaluation of chemiluminescence as sensor for lean premixed combustion. In *4th Symposium on Smart Control of Turbulence.* *(p. 21)*

Titre : Application de la chimiluminescence de flamme et du courant d'ionisation à la surveillance de l'état de combustion pour une chaudière à gaz domestique

Mots clés : Chaudière domestique, surveillance de flamme, chimiluminescence, courant d'ionisation, richesse

Résumé : Les variations de la composition des gaz naturels nécessitent un system de réglage automatique de la richesse de flamme pour des chaudières domestiques à gaz. Dans ce travail, deux solutions potentielles sont étudiées, à savoir la chimiluminescence de flamme et le courant d'ionisation. Des indicateurs de richesse sont déduits des signaux de chimiluminescence obtenus expérimentalement. L'impact de l'échange de chaleur entre la flamme et le brûleur sur des signaux de chimiluminescence est ensuite étudié. Une analyse est également faite des principaux facteurs pouvant perturber la caractérisation du signal de chimiluminescence. Le courant d'ionisation est ensuite étudié sur une flamme conique pour comprendre l'évolution de son intensité avec la position de sonde et avec les conditions de flamme. Il est montré ensuite que ces évolutions sont corrélées avec le changement de la distance entre la flamme et le brûleur. Enfin, une boucle de contrôle est développée pour démontrer la faisabilité d'un réglage automatique de richesse en exploitant le signal de chimiluminescence.

Title : Use of flame chemiluminescence and ionization current for the combustion status monitoring of a domestic gas boiler

Keywords : Domestic boiler, flame monitoring, chemiluminescence, ionization current, equivalence ratio

Abstract : The variations of natural gas composition call for an automatic equivalence ratio regulation system for domestic gas boilers. Two potential techniques for this purpose are investigated, i.e. the flame chemiluminescence and ionization current. Equivalence ratio indicators are inferred from the chemiluminescence signal based on the experiments. The investigation proceeds by examining effects of the flame-burner heat exchange on the chemiluminescence signal. The interference of several disturbing factors for the chemiluminescence signal characterization is also analyzed. The flame ionization current is investigated on a conical flame to understand the evolution of its intensity with the probe position and flame conditions. These changes are then attributed to modifications of the distance between the flame base and the burner rim. Finally a control loop is developed to demonstrate the feasibility of equivalence ratio self-regulation with the chemiluminescence signal.

Université Paris-Saclay
Espace Technologique / Immeuble Discovery
Route de l'Orme aux Merisiers RD 128 / 91190 Saint-Aubin, France